OPTICAL STUDIES OF CUBIC III-NITRIDE STRUCTURES

ROSS EDWARD LEWIS POWELL, Msci.

Thesis submitted to the University of Nottingham for the degree of Doctor of Philosophy

May 2014

Abstract

The properties of cubic nitrides grown by molecular beam epitaxy (MBE) on GaAs (001) have been studied using optical and electrical techniques. The aim of these studies was the improvement of the growth techniques in order to improve the quality of grown nitrides intended for bulk substrate and optoelectronic device applications. We have also characterised hexagonal nanocolumn structures incorporating indium.

Firstly, bulk films of cubic $Al_xGa_{1-x}N$ with aluminium fractions (x) spanning the entire composition range were tested using time-integrated and time-resolved photoluminescence (PL) plus reflectivity measurements. Strong PL emission was recorded from the samples, with improved intensity for higher aluminium concentrations. Temperature dependent and time-resolved PL showed the increasing role of carrier localisation at larger AlN fractions. The reflectivity results showed a near-steady increase in the bandgap energy with increasing AlN content. Alternative interpretations that did and did not involve a transition from direct-gap to indirect-gap behaviour in cubic $Al_xGa_{1-}xN$ were considered.

We next looked at cubic $Al_xGa_{1-}xN/GaN/Al_xGa_{1-}xN$ single quantum well (QW) structures with varying AlN content in the barrier regions. The PL studies indicated that carrier escape from the QWs and non-radiative recombination at layer interfaces were limiting factors for strong well emission. Higher AlN concentration in the barriers appeared to exacerbate these problems.

The doping of cubic GaN with silicon (n-type) and magnesium (p-type) was also studied. For Mg-doped GaN, a strong blue band emission was noted in the PL spectrum, which became more intense at higher doping levels. The Mg-doped GaN layers had low conductivity and their mobility could not be measured due to strong compensation effects. The cubic film had similar time-resolved PL properties for the blue band emission compared to hexagonal Mg:GaN. These results suggested that the blue band was the result of recombination between a shallow Mg acceptor and deep donor, believed to be a complex including a nitrogen vacancy and an Mg atom. This complex was also associated with the compensation effect seen in the electrical measurements.

With the Si-doped cubic GaN, we observed PL spectra that were consistent with other sources. Thicker layers of GaN:Si did not have measurable mobility. This was likely caused by the rough surface structure that was imaged using a scanning electron microscope. The thin layer had a very smooth surface in comparison. The mobility of sub-micron thickness layers with a carrier concentrations of $n = 2.0\times10^{18}cm^{-3}$ and $n = 9.0\times10^{17}cm^{-3}$ were $\mu = 3.9cm^2/Vs$ and $\mu = 9.5cm^2/Vs$ respectively. The mobility values and structural issues indicated that growth improvements were needed to reduce scattering defects.

In addition to cubic structures, we have considered nanocolumn growth of InGaN and InN. $In_xGa_{1-x}N$ nanocolumns were grown on Si (111) by MBE with a nominal indium concentration of $x = 0.5$. PL emission was obtained from samples grown at higher temperature, but overall intensity was low. A second set of samples, where nanocolumn growth was followed by growth of a continuous coalesced film exhibited much stronger PL emission, which was attributed to the elimination of a phase separated core-shell structure in the nanocolumns.

Next, a coalesced $In_xGa_{1-x}N$ structure with vertically varying indium fraction was characterised. PL readings showed evidence of successful concentration grading. Finally, the PL spectra of coalesced InN layers were recorded, for which a specialised infrared PL system needed to be used. The results highlighted how increased growth temperature and indium flux can improve PL properties. For the binary alloy however, coalescence growth can decrease PL intensity compared to the nanocolumns stage.

List of Publications

1. S. V. Novikov, C. R. Staddon, R. E. L. Powell, A. V. Akimov, F. Luckert, P. R. Edwards, R. W. Martin, A. J. Kent, C. T. Foxon, Wurtzite $Al_xGa_{1-x}N$ bulk crystals grown by molecular beam epitaxy, *Journal of Crystal Growth* **322**, 23 (2011)

2. R. E. L. Powell, S. V. Novikov, F. Luckert, P. R. Edwards, A. V. Akimov, C. T. Foxon, R. W. Martin, A. J. Kent, Carrier localization and related photoluminescence in cubic AlGaN epilayers, *Journal of Applied Physics* **110**, 063517 (2011)

3. S. V. Novikov, C. R. Staddon, R. E. L. Powell, A. V. Akimov, A. J. Kent, C. T. Foxon, Plasma-assisted electroepitaxy as a novel method for the growth of GaN layers, *Physica Status Solidi (c)* **9**, 538 (2012)

4. S. V. Novikov, R. E. L. Powell, A. J. Kent, C. T. Foxon, Plasma-assisted molecular beam epitaxy process combined with a liquid phase electroepitaxy, a novel method for the growth of GaN layers, *Journal of Crystal Growth* **378**, 17 (2013)

5. L. E. Goff, R. E. L. Powell, A. J. Kent, C. T. Foxon, S. V. Novikov, R. Webster, D. Cherns, Molecular beam epitaxy of InN nanorods on Si- and C-faces of SiC substrates, *Journal of Crystal Growth* **386**, 135 (2014)

6. R. E. L. Powell, S. V. Novikov, C. T. Foxon, A. V. Akimov, A. J. Kent, Photoluminescence of magnesium and silicon doped cubic GaN, *Physica Status Solidi (c)* **11**, 385 (2014)

Acknowledgement

I would primarily like to thank my supervisor, Tony Kent for offering me this opportunity and providing me with support throughout the research and write up stages. I would also like to thank Sergei Novikov for extremely useful discussions and of course growing the samples. I am also grateful for the experimental assistance provided by Andrey Akimov.

I have received valuable assistance from a large number of technical and administrative staff from the School of Physics and Astronomy. In particular these include Jas and Dave Taylor who helped with my clean room processes and catastrophes as well as Bob and Ian from electronics support who made electronic components for me to use.

I would also like to acknowledge the funding provided by the Engineering and Physical Sciences Research Council (ESPRC), which allowed this research to take place. Finally, my thanks go to my family for the support as well as friends and GameSoc for helping me to unwind. Special mention goes to Dan Moss for providing tools helpful for writing this thesis and Matthew Jones for helping with computer issues.

Contents

List of Figures

List of Tables

Chapter 1: Introduction

1.1 Aims and Objectives

The aim of this work is to characterise cubic nitride films and structures in order to assess the quality of the growth and identify issues that need to be addressed to improve future growth. An additional objective is to improve understanding of the recombination mechanisms that take place within them and quantify figures of merit that would be useful to anyone designing cubic nitride based devices.

1.2 Motivation

The III-nitride semiconductors gallium nitride (GaN), aluminium nitride (AlN) and indium nitride (InN) are widely studied due to their wide range of potential applications in electronic and optoelectronic devices. The energy bandgaps of these materials span a wide region of the electromagnetic spectrum from the ultraviolet of AlN to the infrared of InN. By using tertiary III-nitride compounds with different proportions of group III elements, the bandgap can be tuned to values within this range. In this way, the optical and electronic transport properties can be varied.

Particularly promising applications are high efficiency blue and ultraviolet light emitting diodes (LEDs) and laser diodes (LDs) that can function at room temperature. Such devices fabricated from nitrides have numerous advantages over GaAs equivalents. AlGaN/GaN diodes have a large band discontinuity at the well walls leading to stronger recombination overlap and greater output power density. GaN based devices are also capable of functioning at higher temperatures. Experiments on GaN p-n diodes indicated that the breakdown field of GaN was 3.27MV/cm [1], demonstrating the suitability of the material for use in high power applications.

Considerable progress has been made in improving short wavelength nitride based LEDs. Recent InGaN-GaN blue LEDs have demonstrated external quantum efficiencies of ~64% [2] compared to efficiencies of ~7% achieved twenty years ago [3]. Additional advantages are gained by growing devices on native GaN substrates rather than typical substrate materials

such as sapphire or SiC. These include reduced dislocation density in device structures and improved performance at high injection currents [4]. AlGaN laser diodes that emit at UV wavelengths as low as 336nm with output power of ~3mW have also been fabricated [5].

1.3 The Importance of Cubic Nitrides

Gallium nitride normally crystallises in the hexagonal (wurtzite) structure. Wurtzite nitrides grown on the c-axis are subject to internal spontaneous and piezoelectric polarization fields. The piezoelectric effect occurs since ionic charges in the wurtzite lattice lack sufficient symmetry to possess a centre of inversion. When subject to a strain, such as one brought about by a lattice mismatch to an adjacent layer, the displacement of charges from their equilibrium position breaks the charge distribution symmetry.

This effect results in a net polarization and electric field in the crystal [6]. Spontaneous polarization, oriented along the $(000\bar{1})$ direction, arises as a result of the pyroelectric nature of the material [7], where opposite charges are shifted relative to each other as a result of temperature changes. These polarization fields can lead to reduced emission efficiency in LEDs and laser diodes by forcing electrons and holes to opposite ends of quantum wells and decreasing recombination overlap [8].

Crystals oriented in the (001) direction with a regular cubic lattice are not subject to piezoelectric effects as the presence of a centre of inversion means that the charge distribution is symmetric even under strain. Hexagonal GaN can be grown in non-polar directions that do not possess the internal fields by using particular substrates. These include the a-plane $(11\bar{2}0)$ orientation [9] (as shown in Figure 1.1) and the m-plane $(1\bar{1}00)$ orientation [10]. Alternatively, the material can be grown in the cubic (zinc blende) phase in the non-polar (001) direction.

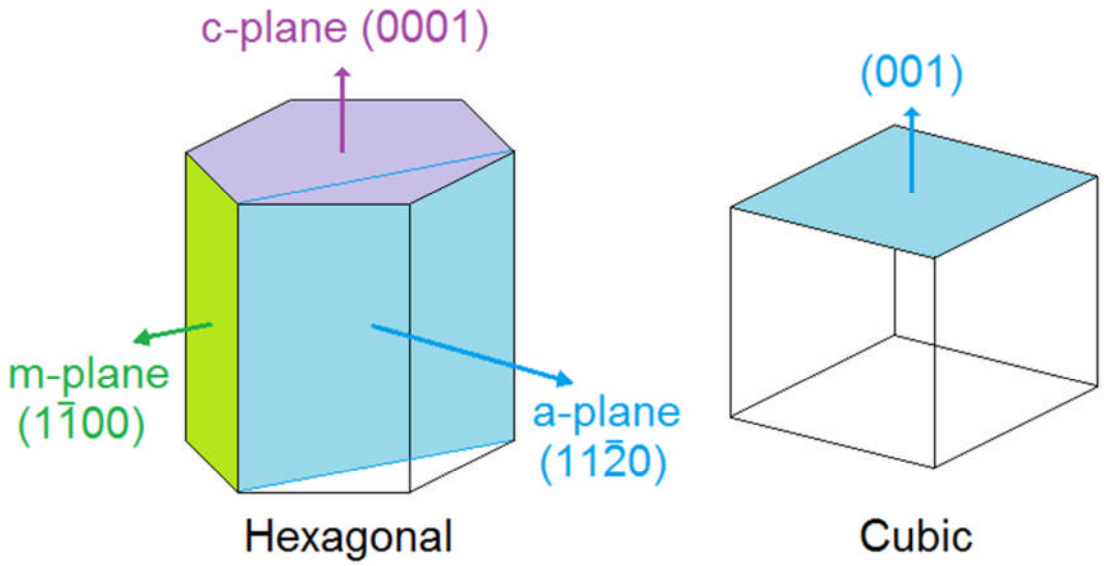

Figure 1.1: An illustration of different growth directions for hexagonal and cubic crystal structures.

The cubic nitrides possess additional advantages beyond the elimination of the internal polarization fields. These include the ability to cleave the material in perpendicular directions plus a shared structure with other cubic materials including GaAs, unlocking applications for bulk cubic nitrides as substrates.

Previous work carried out at Nottingham has concentrated on the development of techniques for the growth of bulk cubic GaN layers lacking the hexagonal inclusions brought about by the thermodynamic instability of the cubic phase [11]. It was determined that gallium-rich growth conditions allowed the best quality bulk cubic GaN to be achieved, with minimal hexagonal inclusions.

After the progress made in the area of bulk growth, this thesis aims to further progression towards cubic nitride device applications by going beyond bulk cubic GaN. Layered structures are fundamental to devices and achieving reliable alloy and doping variations between layers is a vital development stage. The thesis will therefore characterise recently grown tertiary cubic alloys, quantum well heterostructures and cubic GaN subject to both n-type and p-type doping.

1.4 Structure of the Thesis

The structure of this thesis is arranged as follows. The second chapter will outline research that has been done in the field of cubic nitrides, particularly optical studies of grown material. The relevant background physics needed to fully understand the results of the thesis will also be explained. In chapter three, the experimental techniques used to obtain the results of the following chapters are outlined.

The fourth chapter presents the results of optical studies of bulk layers and quantum well structures containing the tertiary cubic alloy AlGaN with different fractions of Al. The effects of aluminium alloy fraction on the emission properties of the bulk layers and wells were investigated. In the fifth chapter, optical and electrical studies of cubic GaN layers doped with magnesium or silicon are discussed. The sample parameters which lead to optimal electronic transport results were identified. In chapter six, we discuss the characterisation of InGaN and InN hexagonal nanocolumn structures, which offer some similar advantages to cubic growth in terms of the reduction in polarization fields. For the final chapter, the main conclusions of the work are stated and avenues for future research are presented.

Chapter 2: Background and Cubic Nitride Research Summary

The majority of nitrides research concerns hexagonal material. Despite this, a significant body of work has been carried out concerning the cubic phase. In this chapter, research concerning the growth plus the optical and electrical properties of primarily cubic nitrides will be reviewed to provide context for the work presented in this thesis.

The differences between hexagonal and cubic nitrides in terms of end product performance have been stated. The fundamental properties of the materials, such as optical and electrical characteristics are influenced by the arrangement of atoms within the crystal structure. This leads to different properties between hexagonal and cubic nitrides, and these will be summarised in this chapter. In addition, the underlying physics of some semiconductor structures and measurement techniques will be explained in order to aid reader understanding.

2.1 Crystal Structure

The two different crystal structures in which group III nitrides occur are shown in Figure 2.1, using GaN as an example. The wurtzite phase is thermodynamically stable under ambient conditions. The zinc-blende phase is metastable and occurs as a result of specially controlled growth on a cubic structured substrate, such as GaAs.

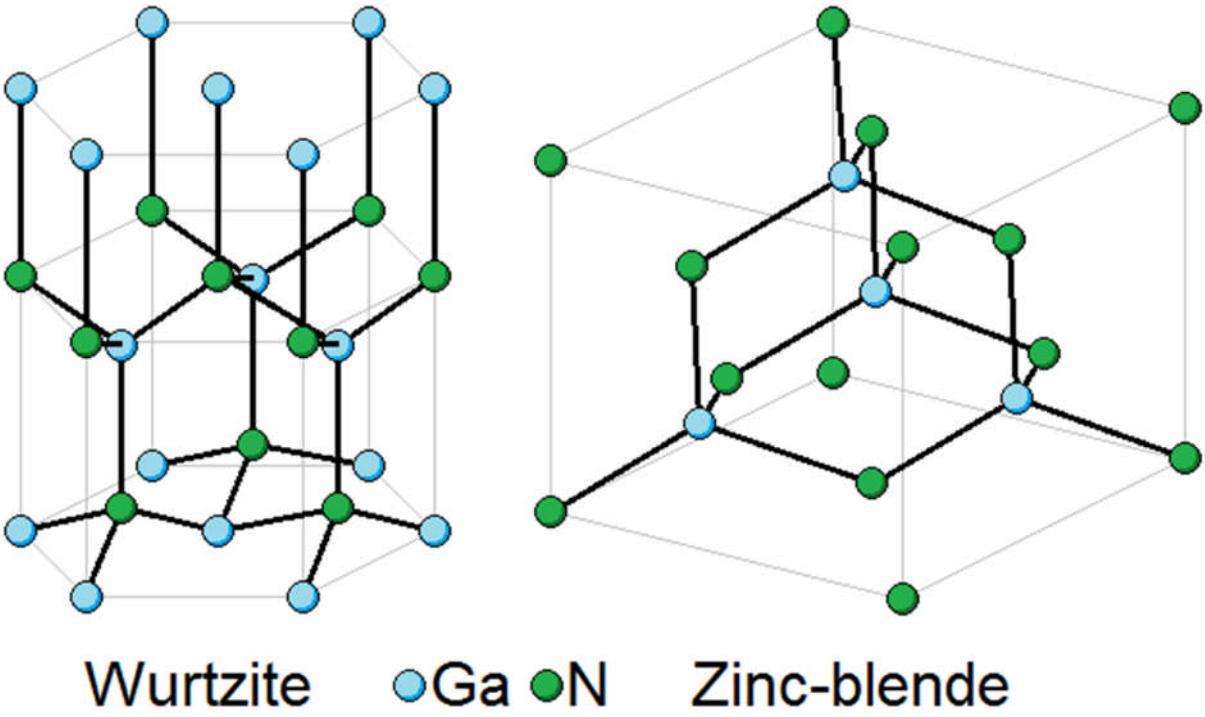

Figure 2.1: Atomic arrangement in the wurtzite (hexagonal) and zinc-blende (cubic) GaN lattice structures.

In the hexagonal unit cell of the wurtzite structure, there are two lattice constants, the vertical, or polar c constant and the horizontal a constant. The zinc-blende unit cell features the gallium atoms positioned in a face-centred cubic arrangement with the nitrogen atoms residing in another face-centred cubic lattice offset from the other by a quarter of a body diagonal. This structure has a single lattice constant a, which is symmetrical in three dimensions. In both structures, each atom is bonded only to four others of the opposite atomic type. The significant differences between these structures lead to distinct properties for hexagonal and cubic variants of the same nitride.

A table of values for the basic properties of the main nitrides in both the hexagonal and cubic forms are shown in Table 2.1. These values were taken from the literature, with experimental results being used when possible, but these were not available in every case. The values vary between sources due to different growth regimes and substrates being employed in each case. In some cases, data is not yet unavailable.

Property	WZ GaN	ZB GaN	WZ AlN	ZB AlN	WZ InN	ZB InN
Bandgap energy, E_G (eV)	3.4 [12]	3.2 [13]	6.00 [14]	5.1 [13]	0.8 [15]	0.596 [16]
Lattice constant, a (Å)	3.189 [17]	4.50 [18]	3.111 [17]	4.38 [18]	3.538 [17]	4.98 [18]
Lattice constant, c (Å)	5.185 [17]	N/A	4.980 [17]	N/A	5.704 [17]	N/A
Electron effective mass, m_e (m_0)	0.22 [19]	0.15 [20]	0.35 [21]	0.25 [18]	0.14 [15]	0.07 [18]
Effective heavy hole mass (m_0) [22]	$m^{\parallel}_{hh}$=1.27 $m^{\perp}_{hh}$=1.02	m_{hh}=0.80	$m^{\parallel}_{hh}$=2.04 $m^{\perp}_{hh}$=2.08	m_{hh}=1.20	$m^{\parallel}_{hh}$=1.56 $m^{\perp}_{hh}$=1.25	m_{hh}=0.84
Effective light hole mass (m_0) [22]	$m^{\parallel}_{lh}$=1.27 $m^{\perp}_{lh}$=0.11	m_{lh}=0.18	$m^{\parallel}_{lh}$=2.04 $m^{\perp}_{lh}$=0.20	m_{lh}=0.33	$m^{\parallel}_{lh}$=1.56 $m^{\perp}_{lh}$=0.09	m_{lh}=0.16
Electron affinity, χ (eV)	3.4 [23]	-	1.9 [24]	2.0 [25]	5.8 [26]	-

Table 2.1: This table gives values of various properties for hexagonal (WZ) and cubic (ZB) nitrides at room temperature.

The valence band at the Γ point in wurtzite nitrides is non-parabolic compared to the cubic nitrides. Since the effective mass is given by the second derivative of the band energy with respect to wavevector k, there are effective hole masses for wurtzite nitrides for two directions in k-space away from the Γ point. For the cubic phase, only one effective hole mass is necessary.

2.2 Summary of Cubic Nitride Growth

This section aims to summarise the growth techniques used to produce cubic nitrides and the properties of the resulting films, so they can be compared to the structures grown for this work.

2.2.1 Growth of Cubic GaN

Previously at Nottingham, cubic GaN films were grown on GaAs (001) substrates by molecular beam epitaxy (MBE). The bulk layers were intended for substrate applications, so a freestanding layer 30-100μm thick was desired. The ability to obtain 2-3 inch diameter wafers from MBE of cubic GaN was identified as an advantage compared to non-polar

hexagonal GaN substrates that must be sliced from the c-axis grown wafers, leaving a section whose width is limited by the growth thickness. [11]

Optimal structural properties were obtained for wafers grown under Ga-rich conditions but not so rich that Ga surface droplets formed. TEM and RHEED measurements indicated that there were no hexagonal inclusions within the first 10μm of layers [27]. Layers with thicknesses between 20μm and 50μm were found to consist of an average of 10% hexagonal material by nuclear magnetic resonance (NMR) spectrometry [28]. About a week of growth was required to obtain the necessary thickness for substrate use at the growth rate of 0.25μm/hour. Maintaining growth conditions for this duration presented a challenge. It was also noted that the hexagonal inclusions were not found within the first 10μm but started to occur as the layers grew thicker.

Elsewhere, cubic GaN layers have previously been grown by Kimura et al. [29] using plasma assisted MBE (pa-MBE) on GaAs (100) substrates with an ordered alloy of GaN and AlN put down before epitaxial growth. As et al. [30] used radio frequency plasma assisted MBE to grow cubic GaN layers up to 1.5μm thick on GaAs (001) with hexagonal content of ~0.1%.

Qin et al. [31] used a thin layer of c-GaN as a buffer and grew wafers under different V/III ratio conditions using MBE on GaAs (001). The proportion of hexagonal to cubic component in the film was determined using X-ray diffraction (XRD) by comparing the relative intensities of diffraction peaks from cubic and hexagonal crystal planes. Moving away from near-stoichiometric Ga-rich growth towards Ga-richer growth caused the hexagonal fraction to increase. On the flipside, using N-rich conditions mostly prevented c-GaN from growing at all. For growth under near-stoichiometric conditions, a hexagonal fraction of ~0.4% was achieved.

Other substrates and growth techniques have also been used to produce cubic GaN. 3C-SiC is another common substrate that possesses cubic crystal structure. The lattice mismatch between 3C-SiC and c-GaN, is 3.7% compared to 20% with GaAs.

MBE grown c-GaN films on SiC have been produced by Daudin et al. [32]. The wurtzite fraction was found to be higher further away from the substrate interface for GaN wafers 1.5μm thick. The smoothness of the SiC surface was found to be important for achieving high

cubic purity as (111) facets on the surface provide nucleation sites for hexagonal material. A slower growth rate at 0.2μm/hour also improved cubic growth.

Wei el al. [33] used Metalorganic chemical vapour deposition (MOCVD) to grow c-GaN on a 3C-SiC layer on top of a Si (100) substrate. The 1μm thick layer had 9% hexagonal component. High temperature growth (950°C) led to effective cubic growth due to strong interaction between the grown layer and underlying substrate. It also enhanced surface atom mobility and re-evaporation, reducing stacking faults.

Despite the smaller lattice mismatch between c-GaN and 3C-SiC, the mismatch still leads to strain and dislocations in the grown wafer. Recent developments [34] have seen c-GaN grown by pa-MBE on 3C-SiC nanostructure posts, resulting in high structural quality GaN produced on the top of the posts due to the reduction in growth area.

Tsuchiya et al. [35] grew cubic GaN films grown by halide vapour phase epitaxy (HVPE) on GaAs (001) with a buffer of a cubic GaN grown by metal organic MBE (MOMBE). They determined that the percentage of hexagonal inclusions increased with the thickness of the film and were reduced at a higher growth temperature. They were able to achieve a 5μm thick film with 10% hexagonal fraction. It was noted that hexagonal inclusions grow on the (111) planes of cubic GaN due to stacking faults in these planes.

MOCVD has also been used to grow cubic GaN on GaAs. Free standing films consisting of a 3μm cubic epitaxial layer on top of a 69μm polycrystalline template film were obtained by Vilchis et al. [36]. The template structure was a result of nitridation at the GaN-GaAs interface. The growth rate was 1.5μm/hour, which is significantly faster than the MBE rate achieved at Nottingham. Yasui et al. [37] used hot-wire CVD to grow c-Gan on GaAs (100), where a hot W-wire was used to decompose NH_3 to provide nitrogen for nitridation of the substrate surface.

Metalorganic vapour phase epitaxy (MOVPE) was used by Funato et al. [38] to grow 0.35μm thick c-GaN on GaAs (001) substrates. They achieved a 10% hexagonal fraction for high temperature growth conducted at the faster of two growth rates at 1.05μm/hour. The dependence of cubic fraction on growth temperature was explained by adatom migration. At low temperature, migration is inactive. At higher temperatures, when migration is active, the

faster lateral growth of the cubic phase allows it to expand whilst the hexagonal grains in the buffer layer have their expansion suppressed. Wu et al. [39] were able to obtain 10% hexagonal inclusions in a thicker cubic GaN layer of 1μm, using the same method, growth temperature and substrate.

We have discussed an array of cubic GaN layers grown by different methods. Many of the layers were thin compared to the bulk layers being developed at Nottingham, so the higher hexagonal fractions of these wafers compared to bulk MBE growth on GaAs (001) are particularly notable. MBE has achieved higher purity cubic GaN, but this requires a slow growth rate. It is evident that the thicker the layer becomes, the more likely hexagonal inclusions are to develop. Despite the greater mismatch between GaN and GaAs, GaAs substrates can be etched off chemically, allowing freestanding cubic GaN to be obtained more easily.

2.2.2 Growth of Cubic AlGaN

Less work has been published on the growth of bulk cubic AlGaN, particularly for high AlN fractions in the alloy. A range of growth techniques and substrates have again been employed in this area although a larger proportion of the growth was done by MBE.

Nakadaira et al. [40] grew 500nm thick cubic $Al_xGa_{1-x}N$ on GaAs (001) using MOVPE up to an AlN fraction of x = 0.51. A cubic GaN buffer layer was put down before the AlGaN to prevent the substrate surface roughening and inducing growth of the hexagonal phase. Emission intensity of the layers decreased rapidly as the AlN component increased due to the increased concentration of impurities such as carbon and oxygen. MOVPE was also employed by Xu et al. [41] on a GaAs (100) substrate. Ammonia provided nitrogen for the growth. Increasing the ammonia flux resulted in the emergence of a hexagonal component that was not present at the lower fluxes.

Martinez-Guerrero et al. [42] grew cubic AlGaN by pa-MBE on SiC (001) layers on top of an Si substrate and utilised in-situ growth control to verify Al incorporation and purity of the cubic phase.

MBE growth on 3C-SiC was used by Okumura et al. [43] to obtain cubic AlGaN films up to 2.1μm thick. XRD measurements showed that the AlGaN layers had separate peaks for c-GaN and c-AlGaN components. The c-AlN layer did not however have its own distinct diffraction peak. Koizumi et al. [44] improved upon this by putting down a cubic AlN buffer layer. Since the lattice mismatch between AlN and SiC was only 0.9%, the buffer led to reduced roughening of the substrate surface and thus reduced formation of (111) facets from which the hexagonal phase grows. Metal rich growth conditions were found to be favourable. They were able to fit the variation of lattice constant against AlN composition to the expected relationship, Vegard's law for the whole AlN fraction range.

There is a larger quantity of published work where cubic AlGaN layers form part of cubic nitride heterostructures such as the quantum well (QW). QWs are of interest because of their utility in optoelectronic devices. They offer several advantages over bulk material for optical emission [45]. The bandgap discontinuity between layers leads to effective confinement for electrons and holes, leading to stronger overlap of their wavefunctions and hence a higher probability of recombination and efficient radiative recombination. The result of this is improved emission brightness.

The emission energy of QWs depends on the confinement energy, allowing the device wavelength to be set by adjusting the well width. The small well widths involved prevent the well material from being affected by stacking faults or dislocations caused by any lattice mismatch.

We have seen that several groups have grown bulk AlGaN layers. Growth of higher AlN content $Al_xGa_{1-x}N$ alloys has been more difficult to achieve. The importance of buffer layers between the substrate and growth layers for good quality growth has been demonstrated. AlGaN has been more widely used as part of QW structures, and these will be discussed in greater detail later in the chapter.

2.2.3 Doping of Cubic GaN

Doping of cubic GaN is an important process for achieving electronic device applications. Two of the more widely used dopants for GaN are magnesium for p-type doping and silicon for n-type doping. These are the dopants that have been employed during this work. The

optical and electrical properties of Mg and Si-doped cubic GaN are discussed later, but we will first consider other dopants that have been incorporated into cubic GaN.

Cubic GaN doped with manganese has previously been grown at Nottingham by MBE on GaAs substrates [46]. This material has potential electronic and spintronics applications. Whilst undoped wafers were found to be n-type, the Mn doped films had p-type conductivity. Ga-rich growth conditions led to improved surface roughness but reduced Mn incorporation.

Results from multiple batches indicated that Mn doping was very reproducible and it was proved that p-type conductivity originated from Mn in the GaN layer rather than Mn diffusion into the substrate. The hole concentration was significantly lower than the Mn dopant concentration, suggesting that compensating donors were forming in the films. Post-growth annealing led to an increase in hole concentration.

As et al. [47] studied carbon as an alternative p-type dopant to magnesium, due to the strong compensation effects encountered when Mg is used. Carbon was incorporated into the layers using electron beam evaporation of a graphite rod. Regions of the wafer subject to Ga-rich growth were p-type whilst those subject to N-rich conditions were n-type. This was attributed to C atoms incorporating at the N site when Ga was in excess.

2.3 Optical Characterisation

A wide range of techniques have been employed by various groups for the characterisation of the optical properties of nitrides. Photoluminescence (PL) has been used primarily during the research conducted for this thesis. In addition, reflectivity measurements were also used. Here, the proportion of light absorbed at different wavelengths was recorded. These allowed accurate measurement of the bandgap energies of cubic $Al_xGa_{1-x}N$ films. Researchers outside of Nottingham have used other optical methods that are briefly summarised below.

Cathodoluminescence (CL) involves the sample being subject to a beam of electrons which scatter through the crystal and provide energy for the excitation of electron-hole pairs. These pairs relax to the bottom of the bands before recombining and emitting photons, which can subsequently be detected. The advantage of CL over optical excitation is that the latter is

limited by the available photon energies of the excitation source, plus the electron beam can be focused to a very small spot size, allowing excitation of sub-micron features [45].

Ellipsometry [45] is a version of reflectivity where the incident light is linearly polarized and arrives at an oblique angle. The reflected light has elliptical polarization. The reflectivity of the reflected light in two perpendicular polarization directions, s and p, is different. The ratio of these values can be equated to a complex number containing two parameters including a phase component. These can be related to optical values using a model of the reflecting structure. After modelling, the dielectric function of the material can be obtained, which relates to the refractive indices and the absorption coefficient. The measurement of a ratio allows for highly reproducible results but the modelling process required for data interpretation can be complex.

In Raman scattering [45], incident laser light scatters inelastically off optical phonons inside the crystal, leading to the light frequency being shifted downwards. By measuring the frequency shift of scattered light, the frequencies of LO and TO phonons in the sample can be determined. The difficulty of this technique is that the intensity of scattered light is low, and the frequency shift is small, making the measured signal difficult to differentiate from scattered laser light.

2.3.1 Photoluminescence Technique

Photoluminescence was the main characterisation technique used throughout this study. The mechanisms behind PL are explained by Pavesi [48] and Singh [49], and illustrated in Figure 2.2. When a laser is shone on the material, electrons are excited from the valence band to the conduction band, generating holes in the valence band. These photoexcited carriers thermalize by emitting phonons and relaxing to the band edges before recombining band to band or via donor/acceptor impurity levels.

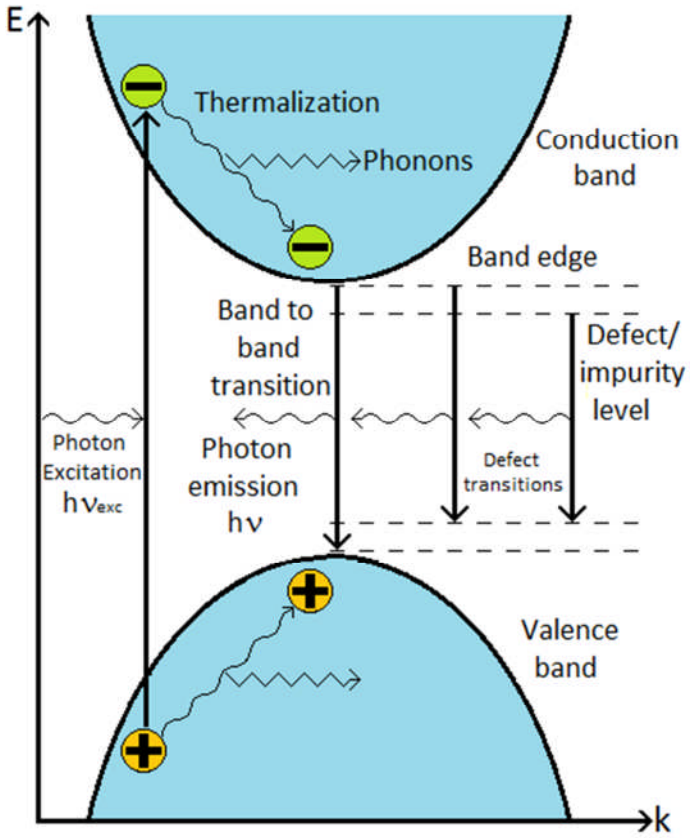

Figure 2.2: Band diagram illustrating PL. Photoexcited carriers rethermalise to the band edge by emitting phonons. Recombination mainly takes place between defect levels, leading to the emission of a range of photon energies.

The PL technique measures the number of photons emitted by radiative transitions as a function of photon energy. Each of the different types of recombination contribute to the PL spectrum for a given sample. Most transitions are between the band tails, additional energy levels outside the edge of the bands brought about due to presence of impurities, strains and defects [50]. As a result, the broadened main peak in the PL spectrum corresponds to the average near band edge transition and does not give a direct measurement of the bandgap energy.

In addition, electrons and holes can bind together to form an exciton with an exciton binding energy, E_x. The two carriers are held together by mutual Coulomb attraction. These excitons can become trapped on impurities before recombination; this is known as a bound exciton whilst unbound excitons are called free excitons. When the bound electron and hole recombine they emit a photon whose energy, hν is lowered from the bandgap due to the exciton binding energy; ie. $h\nu = E_G - E_x$. Additional peaks at higher energies than the main

band tail emission peak can be seen on the PL spectrum as a result of transitions involving free or bound excitons.

2.3.2 Photoluminescence Emission from Quantum Wells

PL emission from a quantum well (QW) is affected by the band structure according to rules that will now be explained. We will consider a simple QW structure consisting of a layer of small bandgap material sandwiched between two layers of higher bandgap material, as shown in Figure 2.3. The QW is irradiated from the z direction by light of angular frequency ω, which is absorbed. This excites electrons between the valence band and the conduction band from an initial state $|i\rangle$ with energy E_i and a final state $|f\rangle$ with energy E_f. The absorption rate is given by Fermi's golden rule [45]:

$$W_{i\to f} = \frac{2\pi}{\hbar}|M|^2 g(\hbar\omega) \tag{1}$$

where, M – matrix element representing the perturbation of electrons by the light wave
g(ħω) – density of states in the band at the photon energy ħω.

The matrix element M can be written in terms of the light wave perturbation H':

$$M = \langle f|H'|i\rangle = \int \psi_f^*(\boldsymbol{r})H'(\boldsymbol{r})\psi_i(\boldsymbol{r})d^3\boldsymbol{r} \tag{2}$$

where, **r** – position vector of the electron.

The perturbation consists of an electron energy shift caused by the electric field of the photon, ε_p acting on the electron dipole moment, p_e:

$$H' = -p_e.\varepsilon_p. \tag{3}$$

The electron dipole moment is expressed as:

$$p_e = -e\boldsymbol{r}. \tag{4}$$

The incoming light is defined as a plane wave with the form:

$$\varepsilon_p = \boldsymbol{\varepsilon}_0 e^{i\boldsymbol{k}.\boldsymbol{r}} \tag{5}$$

where, $\boldsymbol{\varepsilon}_0$ – electric field amplitude.

Equations (4) and (5) can be inserted into expression (3) such that the perturbation becomes:

$$H'(\boldsymbol{r}) = e\boldsymbol{\varepsilon}_0.\boldsymbol{r}e^{i\boldsymbol{k}.\boldsymbol{r}}. \tag{6}$$

Since the wave vector of the photon is small compared to the wave vector of the electron, the exponential factor describing the light wave can be set equal to one. The absorption rate is hence:

$$W_{i\to f} = \frac{2\pi}{\hbar}|\langle f|-e\boldsymbol{r}.\boldsymbol{\varepsilon}|i\rangle|^2 g(\hbar\omega). \tag{7}$$

The selection rules for QW transitions can be derived by considering the matrix element. The design of the QW means that the z direction is not equivalent to the x and y directions, so we will consider light that is polarized in the xy plane. The initial state of the transition is the nth hole state whilst the final state is the n'th electron state. According to Bloch's theorem, the state wavefunctions should be described as modulated plane waves with envelope functions u(r) whose periodicity is equivalent to that of the crystal lattice:

$$|i\rangle = \frac{1}{\sqrt{A}}u_v(\boldsymbol{r})\varphi_{hn}(z)e^{i\boldsymbol{k}_{xy}.\boldsymbol{r}_{xy}} \tag{8}$$

$$|f\rangle = \frac{1}{\sqrt{A}}u_c(\boldsymbol{r})\varphi_{en'}(z)e^{i\boldsymbol{k}'_{xy}.\boldsymbol{r}_{xy}} \tag{9}$$

where, A – normalisation area in the x-y plane

φ(z) – z direction bound states of the QW

$e^{i\boldsymbol{k}_{xy}.\boldsymbol{r}_{xy}}$- xy plane free motion plane wave.

Conservation of momentum between the states dictates that $\mathbf{k}_{xy} = \mathbf{k'}_{xy}$ as the momentum of the photon is much smaller than the electron momentum. These equations can be inserted into the expression for the x direction matrix element. The result can be separated into two components:

$$M = \langle f|x|i\rangle = M_{cv}M_{nn'}. \tag{10}$$

The first component is the valence-conduction band dipole moment:

$$M_{cv} = \langle u_c|x|u_v\rangle = \int u_c^*(\boldsymbol{r})xu_v(\boldsymbol{r})d^3\boldsymbol{r}. \tag{11}$$

The second consists of the overlap of electron and hole wavefunctions:

$$M_{nn'} = \langle en'|hn\rangle = \int_{-\infty}^{+\infty} \varphi_{en'}^*(z)\varphi_{hn}(z)dz. \tag{12}$$

The atomic orbital and band structure properties of most III-V materials are highly conducive to electric dipole transitions from the valence band to the conduction band, leading to a large M_{cv} component. The matrix element is therefore proportional to the electron-hole overlap. For an infinite QW of width d, the wavefunction of the nth bound state is given by:

$$\varphi_n(z) = \sqrt{2/d}\sin\left(k_n z + \frac{n\pi}{2}\right). \tag{13}$$

The overlap function resulting from this would be:

$$M_{nn'} = \frac{2}{d}\int_{-d/2}^{+d/2} \sin\left(k_n z + \frac{n\pi}{2}\right)\sin\left(k_{n'} z + \frac{n'\pi}{2}\right)dz. \tag{14}$$

This overlap function evaluates to zero for transitions between states that fail to meet the condition n' = n + 2m (m = 0, 1, 2…), in which case a finite value is observed. This result means that the transition rate is only non-zero for transitions between valence and conduction

states of the same number and those separated by a multiple of two. The selection rule for transitions in an infinite QW is hence:

$$\Delta n = n' - n = 2m \ (m = 0, 1, 2 \ldots). \tag{15}$$

This result has been visualised on Figure 2.3, where allowed transitions in the QW are shown. Although this selection rule was derived for an infinite well, in finite wells the $\Delta n \neq 0$ transitions are mostly weaker and therefore don't cause a large deviation [45].

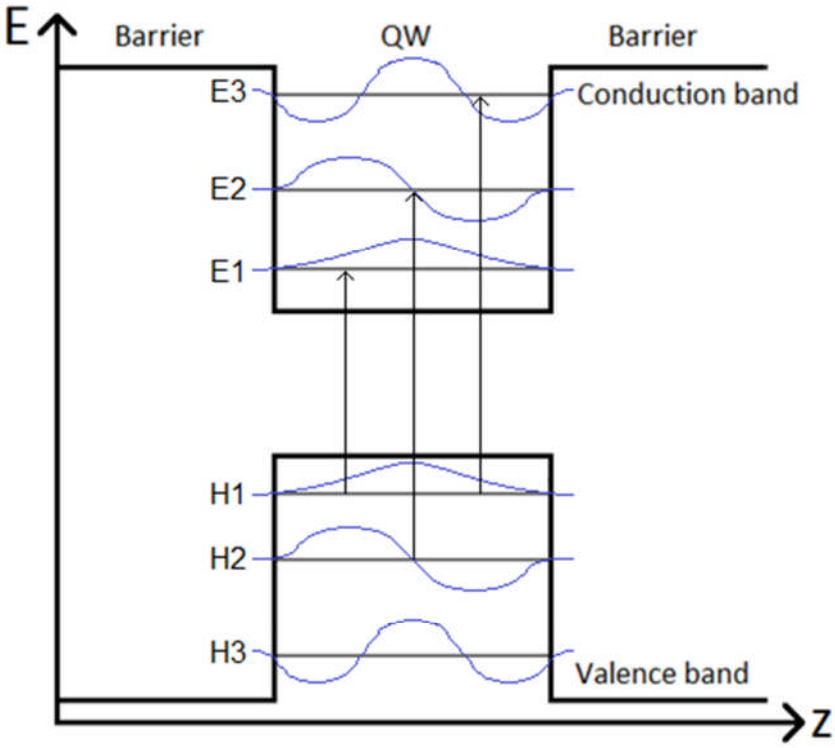

Figure 2.3: Energy band diagram for a QW, showing some allowed transitions between bound states.

The selection rule means that the lowest energy levels for injected carriers to recombine between are at the energy of the n = 1 confined states rather than the band edges. Compared to emission from bulk material, the energy of the PL emission peak is adjusted higher by the confined state energies in the valence and conduction bands (excluding exciton binding energy):

$$E_{PL} = E_G + E_{hh1} + E_{e1} \tag{16}$$

where, E_{hh1} – energy of the first bound heavy hole state

E_{e1} – energy of the first bound electron state.

There is another consideration that affects QW emission, particularly in the presence of the internal fields known to exist in hexagonal nitrides. An electric field applied to a QW in the z direction leads to the quantum confined Stark effect (QCSE). Electrons and holes in excitons are pushed in opposite directions by the field but remain bound as an exciton due to the confining barriers. The interaction of these bound excitons with the electric field causes their energy to be shifted lower. Figure 2.4 demonstrates how the application of an external electric field affects an ideal QW.

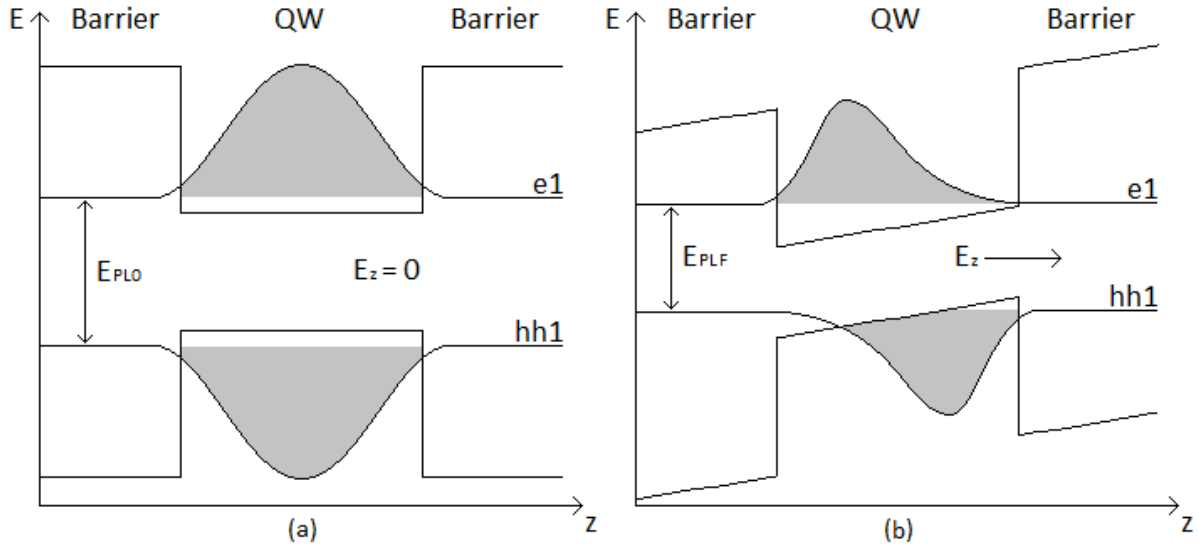

Figure 2.4: Illustration of the quantum confined Stark effect showing the band structure and lowest energy state probability densities of an ideal QW with (a) no applied field and (b) an electric field applied in the z direction.

The potential difference over the well leads to a change in potential across that causes tilting of the bands and decreases the energy of the bound states. This leads to a decrease of the emission energy and redshifting of the emission wavelength. The electron and hole probability densities are shifted in opposite directions, causing the electron-hole overlap to be reduced along with the emission intensity.

The above situation considers an ideal QW subject to an external electric field. In the case of hexagonal nitride wells, the strain due to interface lattice mismatch results in spontaneous and

piezoelectric polarisation charge build up around the interfaces [51], resulting in the QCSE without any applied field. Evidence of the QCSE in PL spectra can therefore be used to determine whether hexagonal material exists within cubic QW structures.

2.4 Summary of Optical Studies on Cubic Nitrides

Now that the mechanics of the optical characterisation methods have been explained, the results of optical studies on cubic nitrides from the literature can now be summarised.

2.4.1 Optical Studies of Cubic GaN

We will first consider a typical PL spectrum for cubic GaN and discuss the origin of the major features based on what is stated in the literature. The spectrum shown in Figure 2.5 was taken from a pure cubic GaN wafer grown and studied for the present work. The energy positions of the peaks have been highlighted. The locations of these peaks vary slightly between sources owing to differences in growth techniques and substrates, leading to different strains, defects and impurities, but they are still readily identifiable.

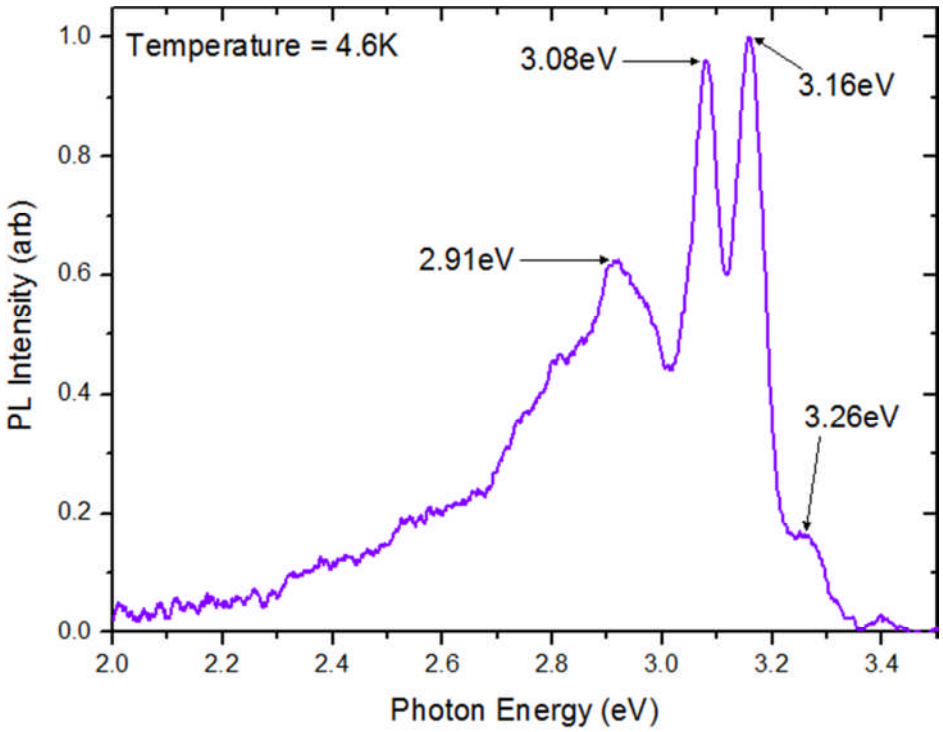

Figure 2.5: PL spectrum of a 466nm thick cubic GaN film grown by pa-MBE. The energies of prominent emission peaks have been highlighted.

The two highest energy peaks are generally well understood. The highest energy peak is found at 3.26eV and forms part of the high energy shoulder of a larger peak in this case. It has been identified as the result of excitonic recombinations. These recombinations may involve a shallow donor bound exciton [52]. The peak may also be the result of overlapping contributions from both free and bound exciton recombination [53].

The peak at 3.16eV is usually the dominant feature of the spectrum. This has been attributed to the recombination of shallow donor acceptor pairs (often denoted DAP or D^0-A^0). These consist of electrons and holes from impurities that sit in the energy band tails away from the band edge. Feneberg et al. [53] have assigned binding energies to the acceptor of E_A = 130meV and the donor of E_D = 30meV, and noted that the donor binding energy was similar to that of silicon and oxygen in hexagonal GaN, where they occur often as impurities.

Philippe et al. [54] identified the same two peaks in the low temperature PL spectrum of their cubic GaN sample. They observed that as the temperature was increased, the intensity of the peaks diminished whilst a new peak emerged on the higher energy side of the D-A peak. This new peak was attributed to conduction band to acceptor recombinations as the donors became ionised at higher temperature. Hence we can expect the shape of the PL spectrum to change with temperature.

The lower energy peaks are not as well characterised, and identification is complicated by transitions involving deeper impurities and phonon replicas of the main peaks that can be mistaken for each other. The 3.08eV peak has been associated with a DAP transition with a deeper donor [52] or alternatively between a free or donor electron and an As impurity acceptor [55].

Xu et al. [56] identified two peaks at energies of 2.82eV and 2.96eV forming part of a broad low energy feature. The similar temperature dependent behaviour of these peaks to the 3.16eV DAP peak led them to identify the two lower energy peaks as DAP transitions as well, involving the same shallow donor, but deeper acceptors with binding energies of 447meV and 342meV. The origin of the levels was uncertain, but it was possibly due to intrinsic defects or growth contamination, such as oxygen incorporation. There are similarly sited features in our spectrum.

2.4.2 Optical Studies of Cubic AlGaN

A number of optical studies have been performed on cubic AlGaN layers with AlN concentrations spanning the entire range. A particularly controversial issue surrounding cubic AlGaN is the question of whether the alloy becomes indirect leading up to pure AlN and at what AlN concentration this takes place. A transition is widely predicted in theoretical models, but many optical studies do not observe evidence of a transition. We have looked for evidence of this in our own cubic $Al_xGa_{1-x}N$ wafer study.

Kanoun et al. [57] used a density-functional theory (DFT) approach to calculate the energies of the direct Γ-Γ band gap and the indirect Γ-X band gap across the composition range. They found that the Γ-Γ energy overtook the Γ-X energy at $x \sim 0.62$, marking a transition to indirect gap. Ellipsometry performed on cubic AlN by Röppischer [58] revealed an absorption tail below the direct bandgap in the imaginary part of the dielectric function, suggesting indirect absorption at 5.3eV. Other theoretical studies have also calculated the bandgap as remaining direct across the whole AlN content range, such as Amin et al. [59].

Landmann et al. [60] used spectroscopic ellipsometry to study a series of cubic $Al_xGa_{1-x}N$ layers. Energy values taken from the resulting dielectric function were used in conjunction with a variety of numerical methods to evaluate the transition x value. A hybrid functional DFT method led to a crossover at $x = 0.71$. Purely numerical calculations were found to agree closely with their experimentally derived result, producing values of $x = 0.64$-0.69.

Nakadaira et al. [40] observed a near-linear increase in PL emission energy with increasing AlN content, and hence no indication of a transition for $Al_xGa_{1-x}N$. This could only be relied upon up to $x \sim 0.4$ however due to loss of intensity via impurity incorporation.

The reflectivity spectra obtained by Martinez-Guerrero et al. [42] feature a sharp disappearance of the interference fringes across the whole AlN composition range studied, indicating a direct absorption edge in each case. They did however acknowledge the possibility that the direct absorption edge was not the fundamental AlGaN bandgap. Okumura et al. [61] used CL and spectroscopic ellipsometry on samples covering the full range of aluminium fraction and found that the absorption edge was close to the CL emission

energy, which increased linearly with AlN composition, indicating a direct gap across the range.

To summarise, the lack of consensus on the question of a direct to indirect gap transition in cubic AlGaN is clear. Addressing this issue is the main motivation of the reflectivity measurements performed in this study.

2.4.3 Optical Studies of Cubic Nitride Quantum Wells

Only a limited amount of material is available concerning cubic nitride QW structures similar to those studied in this work. Badcock et al. [62] grew non-polar, a-plane ($11\bar{2}0$) hexagonal GaN/$Al_{0.18}Ga_{0.82}$ multiple quantum wells (MQWs) on sapphire using MOVPE and were able to confirm a lack of QCSE. The PL spectra however featured a peak due to recombination of carriers at sites introduced by Basal stacking faults resulting from non-polar growth.

Corfdir et al. [63] used HVPE to grow a-plane $Al_xGa_{1-x}N$/GaN QWs without any stacking faults. Their PL studies showed that the emission intensity and carrier lifetime was limited by the escape of carriers from the wells into the barriers where non-radiative recombination took place.

MBE-grown cubic MQWs made from GaN with $Al_xGa_{1-x}N$ barriers on GaAs (001) were studied using CL, PL and photoreflectance by Köhler et al. [64]. The well widths ranged from 2.5nm to 10nm whilst the barrier AlN fraction varied between x = 0.07 and x = 0.5. A distinct QW emission peak was recorded on the CL spectra, at energies between the $Al_xGa_{1-x}N$ barrier and GaN buffer peaks. The energy of QW emission was tuned by changing the AlN concentration and well width, whilst luminescence intensity was greatly enhanced by the integration of additional wells.

Schörmann et al. [65] presented the PL spectra of cubic single and multiple QW structures with 3nm GaN wells and 6nm $Al_{0.15}Ga_{0.85}N$ barriers grown on a 3C-SiC substrate by MBE. Intense room temperature near-UV emission was observed. The linewidth of the MQW emission was wider due to well width fluctuations across the sample. The linewidths were similar to those obtained from a-plane hexagonal QWs, highlighting the potential device applications of the cubic equivalent. A fit between the experimental and calculated values for

the transition energy against well width indicated that internal polarization and piezoelectric fields were not present.

We have seen how the PL emission energy of QWs is modified by changing the specifications of cubic nitride QWs, such as well width and barrier height. QW structures also allow the lack of internal fields in non-polar and cubic nitrides to be experimentally demonstrated. Carrier escape from QWs has been highlighted as a key contributor to non-radiative recombination.

2.4.4 Optical Studies of Doped Cubic GaN

Although doping is often employed to modify electrical properties, it has a significant effect on the optical behaviour of nitrides. Optical studies can therefore indicate the degree to which the dopant has been incorporated into the wafer. The following studies have investigated the optical properties of doped layers

PL of C-doped cubic GaN, undertaken by As et al. [47] identified the typical band edge peak plus an intense red band around 2.1eV. This was identified as the combined result of two recombinations. The first was between a deep donor complex involving C and the valence band and the second was between the deep complex and the shallow C acceptor.

As and Lischka [55] obtained PL spectra for both Si and Mg-doped cubic GaN, with a wide range of doping levels. For Mg-doped material, in addition to the D^0-A^0 and X emissions, peaks due to transitions involving a shallow Mg acceptor were detected. As the Mg doping level increased, a broad band at low energy around 2.8eV grew in relative intensity until it dominated the spectrum. The origin of this feature was uncertain but its presence indicated that Mg was potentially forming complexes. This blue band has also been observed by Martinez-Guerrero et al. [66].

For Si-doped cubic GaN, the D^0-A^0 and X peaks were once again noted. The donor-acceptor peak broadened and shifted to higher energy for higher Si fluxes and eventually merged with the exciton peak to form one broad feature. This effect was attributed to the development of a broadened band tail due to inhomogenous impurity distribution and shrinkage of the bandgap due to the emergence of an impurity band.

Si-doped cubic GaN was grown by Wang et al. [67] using MBE on SiC. The structural properties of the layers were studied by atomic force microscopy (AFM) and transmission electron microscopy (TEM). The more heavily doped layers had a greater density of stacking faults, attributed to the reduced stacking fault energy due to Si doping. It was noted that stress due to lattice mismatch was reduced due to the substitution of Ga atoms with Si atoms plus the presence of stacking faults.

In their PL spectra they observed a strong room temperature peak at 3.26eV that broadened at the higher doping level. The broadening of the peak was attributed to randomly distributed donor atoms that lead to fluctuations in concentration and thus the band profile, permitting a wider range of recombinations to contribute to the emission. A peak was also observed at the low energy of 1.8eV, possibly due to deep levels introduced by Si doping.

Li et al. [68] reported on PL measurements carried out on Si-doped cubic GaN grown by MBE on GaAs (001). The main near-band edge emission peak was seen to broaden and shift to lower energies as the concentration of incorporated Si increased. The shift in energy was explained by band gap narrowing, an effect observed elsewhere [69]. The broadening effect was greater compared to the hexagonal equivalent.

2.5 Electrical Characterisation

Amongst the main quantities used to assess doped semiconductors are the concentration, the density of carriers that contribute to conduction, and the carrier mobility, a measure of the drift velocity in response to a unit of electric field. These values can be obtained via Hall measurements, which are outlined in the next chapter. A number of electrical studies have been conducted on doped layers of cubic GaN, and these are summarised in Table 2.2.

Source	Dopant	Concentration (cm^{-3})	Mobility (cm^2/Vs)
As et al. [70]	N-rich growth*	~10^{13} (p-type)	350
As et al. [70]	Ga-rich growth*	~10^{14} (n-type)	100
As and Lischka [55]	Mg	3×10^{16} (p-type)	215
Martinez-Guerrero et al. [66]	Mg	~4×10^{18}	35
Lin et al. [71]	Mg	8×10^{16}-8×10^{18}	39
As and Lischka [55]	Si	3×10^{19} (n-type)	100
Martinez-Guerrero et al. [66]	Si	3×10^{18}-4×10^{19}	170-50
Novikov et al. [46]	Mn	~10^{18} (p-type)	300
As et al. [47]	C	6×10^{18} (p-type)	19

Table 2.2: This table shows measured carrier mobility values for various doped cubic GaN layers taken from the literature. *These samples were not doped but were p-type or n-type due to growth conditions.

Even without intentional doping, n or p-type conductivity can be found in cubic GaN films due to the presence of other impurities. This was demonstrated by As et al. [70], where N-rich growth conditions led to p-type material and Ga-rich growth resulted in n-type material. They were unable to identify the chemical nature of the donors and acceptors but stated that they were likely to be intrinsic defects.

As and Lischka [55] noted that increasing the amount of incorporated Mg in their doped cubic GaN layers did not increase the free hole concentration. Compositional analysis of the material showed that more Mg atoms had been incorporated due to higher Mg flux, whilst the intensity of the blue emission band in the PL spectrum also increased. This led the authors to conclude that the Mg related complexes that were contributing to the blue band were acting as compensating donors and thus preventing an increase in free hole concentration. These compensation effects may also explain the reduced mobility of the Mg-doped layers compared to other p-type dopants in Table 2.2.

A similar lack of correlation between Mg incorporation and hole density was observed by Martinez-Guerrero et al. [66], as well as difficulties in obtaining reliable Hall measurements. This was attributed to impurity atoms being trapped on structural defects.

For Si doping of cubic GaN in As and Lischka [55], the mobility peaked at an electron concentration of $3\times10^{19}cm^{-3}$ before decreasing, possibly due to scattering off threading edge dislocations at higher concentrations.

Kim et al. [72] studied heavily Si-doped cubic GaN and noted that at low temperatures, the carrier concentration increased whilst the mobility increased. This was attributed to conduction being dominant in an impurity band at low temperatures, whilst it was dominant in the conduction band at higher temperatures. The impurity band sits below the conduction band edge due to the high density of impurity sites leading to high overlap. Conductivity in the band was reduced at lower doping levels due to the increased dopant separation. They suggested that Si provides a donor level at ~62meV.

We have seen how doping cubic GaN layers alters their optical properties. In Mg-doped GaN, a low energy blue band develops as a result of increased Mg incorporation. In Si-doped GaN, the spectral peaks broadened at higher doping levels due to potential fluctuations. The electrical properties have also been presented. Achieving high hole concentrations in Mg-doped material has proved difficult due to self-compensation, which is likely related to the blue band emission peak. A range of carrier mobility values have been obtained for Mg and Si-doped cubic GaN.

2.6 Studies of InN and InGaN Grown in the Nanocolumn Structure

In addition to studies of cubic GaN and AlGaN, we have characterised nitride structures that incorporate indium. Instead of the cubic phase of InN and InGaN, hexagonal nanocolumns have been grown. Cubic InN is extremely difficult to grow, but the use of hexagonal nanocolumns offers benefits over continuous hexagonal layer growth and thus leads to a variety of device applications. The small bandgap of InN allows a very wide range of bandgap energies to be achieved by integrating indium into the III-nitride system.

As an alternative to continuous layered structures, nitrides can be grown as separate columns with diameters less than 1μm. Nanocolumn growth offers the primary advantage of being strain free [73]. In bulk films, the difference between the thermal expansion coefficient in the substrate and the grown layer leads to a build-up of residual strain. In nanocolumns, only the first few monolayers are affected by the mismatch, and the lattice parameter of the grown material is restored a short distance from the interface.

The result of this lessened strain is a reduction in polarization fields and suppression of non-radiative recombination defect sites [74]. The reduced influence of polarization fields shows

that nanocolumns have some advantages in common with the cubic phase growth. In addition the large surface area to volume ratio leads to high light collection and extraction efficiency plus improved quantum confinement leading to enhanced radiative recombination.

Calleja et al. [73] suggest that the key to nanocolumn growth of III-nitrides is the use of nitrogen-rich growth conditions which suppress the surface diffusion of metal atoms which drives sideways growth.

Transmission electron microscopy (TEM) studies of InGaN nanocolumns grown by rf-MBE on Si (111) and indium flux ratios between 0.13 and 0.3 have been carried out by Tabata et al. [75]. They revealed a lack of threading dislocations and stacking faults at the substrate/column interface. Stacking faults elsewhere in columns did not originate from this region, and their density decreased at higher growth temperatures.

Coalescence is a process where the growth conditions are changed so that the nanocolumns merge together into a continuous layer. The nanocolumns can be grown free of dislocations before coalesced layers are grown to obtain the planar geometry that is suited to device fabrication [76].

This concept was demonstrated by Kuskabe et al. [77] in their growth of GaN by rf-MBE on sapphire (0001). A thick (2.7μm) overgrown layer was deposited on top of nanocolumns. They noted that residual stress was confined to the area near the nanocolumn/substrate interface due to the slender profile of the columns. In addition, the columns released biaxial strain, preventing warping of the overgrown layer. The lack of residual strain in the overgrown layer was confirmed by XRD measurements that gave a c-axis lattice constant value close to that of free-standing bulk GaN.

Grandal et al. [78] grew InN layers on Si (111) substrates using pa-MBE. They found that nitrogen-rich growth conditions encouraged the columnar growth whilst increasingly indium-rich conditions led to stronger coalescence. The growth temperature was kept under 500°C to prevent dissociation of the InN and the emergence of indium droplets. The growth rate also had to be limited since it prevented coalescence at higher levels.

InN nanocolumns were grown by Stoica et al. [79] on Si (111) by rf-MBE. Higher indium fluxes led to the columns becoming increasingly wider at the top relative to the bottom, eventually resulting in coalescence. This was due to the growth dynamics where indium atoms diffuse up the lateral side of the columns. The higher growth temperature led to improved indium surface diffusion and so more rapid nucleation at existing features and thus a reduction in column density.

InN is often subject to strong edge effects, where very high electron densities accumulate on the surface [80]. This is caused by the break in translational symmetry at the surface [81], which leads to positively charged states appearing within the bandgap. These states induce an electric field and downward bending of the bands, resulting in the accumulation of electrons at the surface.

Due to high surface to volume ratio of nanocolumns, they are particularly susceptible to these edge effects. The surface accumulation causes filling of the near conduction band states. The PL emission thus has a broadened peak and shifts to higher energy whilst the peak energy is insensitive to temperature and excitation power variations.

The strain-reducing benefits of nanocolumn growth for InN and InGaN have been presented along with examples of this growth from the literature. Coalescence allows the strain free nanocolumns to be transitioned into continuous layers that can be used in devices. We have also seen how strong edge effects in InN could potentially affect any structures we grow.

2.7 Summary and Conclusions

In this chapter the basic properties of cubic nitrides were discussed. The body of research that has been conducted on the growth and characterisation of cubic nitrides relevant to this work was also summarised, including recent developments. Although a significant amount of work has been done, there are many gaps and some controversies for cubic nitrides beyond pure cubic GaN. This thesis will report on developments in the growth of cubic nitride alloys, quantum wells and doped layers with the hope of building upon existing research and moving towards device fabrication.

Chapter 3: Sample Preparation and Experimental Techniques

This chapter will discuss the techniques used in the study of the cubic nitrides, from sample fabrication to characterisation. The results obtained using these techniques are presented in the next chapters.

3.1 Sample Growth

All films studied were grown by Sergei Novikov at the University of Nottingham. The cubic films were grown using plasma assisted molecular beam epitaxy (pa-MBE) in a MOD-GENII system. The substrate used for cubic growth was GaAs (001), which shares the zinc-blende (cubic) structure with the grown layers.

An excess arsenic flux is used to encourage GaN to grow in the cubic structure, rather than hexagonal, as the arsenic acts as a surfactant. A model to explain this proposed by Cheng [82] suggests that the arsenic stimulates growth of the cubic GaAs structure to match the underlying substrate. As the bond energy of gallium to nitrogen is higher than that of gallium to arsenic, the mobile active nitrogen replaces the arsenic and bonds to the gallium in the cubic structure whilst the arsenic desorbs, leaving cubic GaN.

For the growth of cubic AlGaN, an excess of group III elements on the growth surface is additionally needed, and this was achieved by an excess gallium flux. Since aluminium preferentially bonds with active nitrogen over gallium, the excess gallium does not hinder the growth of AlGaN. The presence of a gallium ‘lake’ that is a couple of monolayers thick on the surface prevents oxidation of the growth surface and increases the mobility of aluminium. A cubic GaN buffer layer was put down before the alloy in order to initialise the cubic growth.

An HD25 RF activated plasma source produced active nitrogen for the growth. Conventional solid effusion cells were used to provide the lattice elements gallium and aluminium, as well as dopants such as magnesium and silicon.

The temperature of the growth was monitored using an optical pyrometer. The samples were monitored during growth using reflection high-energy electron diffraction (RHEED) and, post-growth using x-ray diffraction (XRD).

In addition to cubic films, nanocolumn arrays of hexagonal InGaN and InN were also grown. The same pa-MBE system was used, but the substrate in this case was Si (111). Nanocolumn growth was encouraged by strong nitrogen-rich conditions. The growth temperature was significantly lower than for GaN growth due to the low desorption temperature of indium.

3.2 Photoluminescence Measurements

The principles behind photoluminescence (PL) were explained in the previous chapter (Section 2.3.1). The process of preparing the sample for PL measurement and the experimental set-up and technique used for obtaining the measurement will now be explained.

3.2.1 Sample Preparation and Mounting

For many wafers, droplets of gallium that had formed on the surface during post-growth cooling were present. These had to be removed before performing characterisation measurements in order to ensure measurement results originated from the film and not surface droplets. This was performed by leaving the sample immersed in pure hydrochloric acid overnight and verified by imaging before and after with an optical microscope, as shown in Figure 3.1.

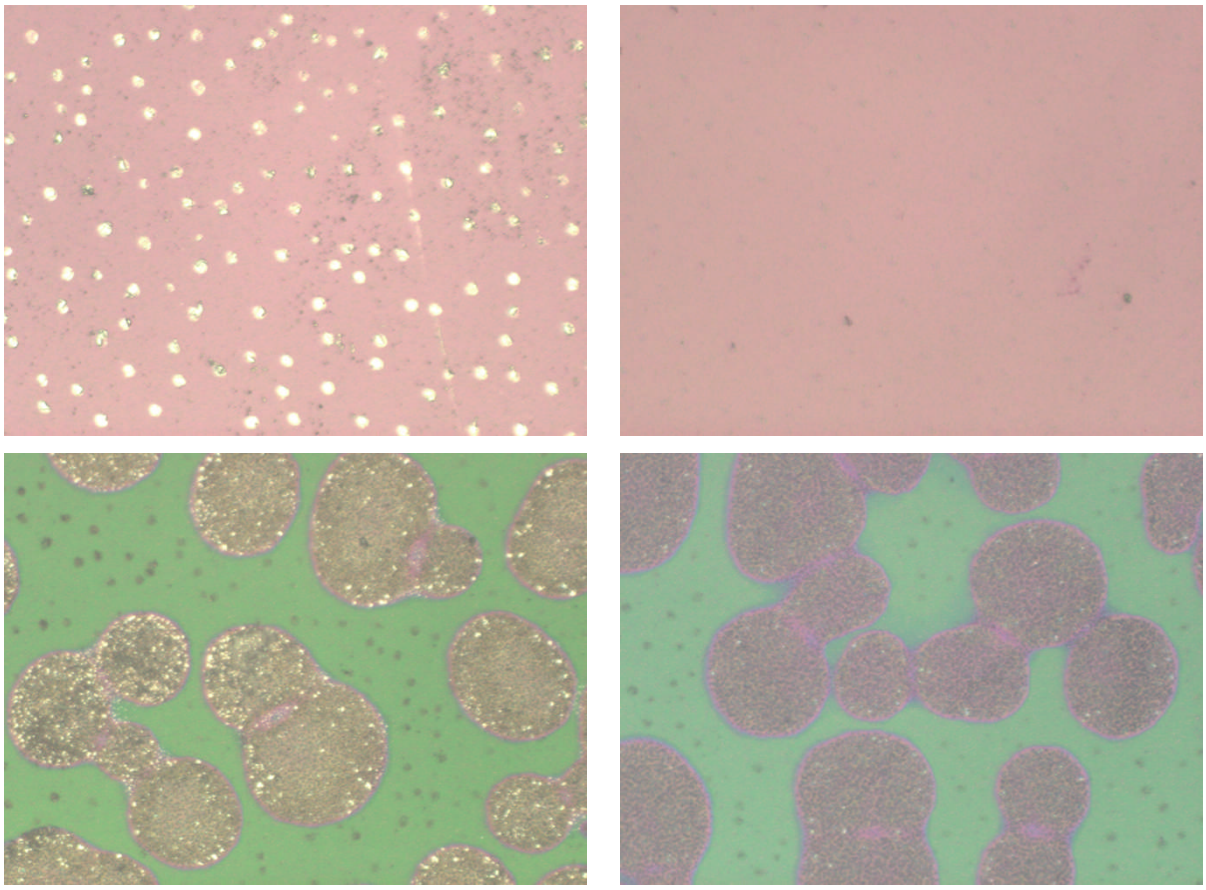

Figure 3.1: Optical microscope images of surfaces of AlGaN samples before (left) and after (right) etching. The white dots seen to disappear in each case are the gallium droplets.

For most measurements, the samples were affixed to a 2cm square copper plate designed to fit on the sample holder at the end of the cryostat arm. A small amount of GE varnish was used for adhesion, which dries fully after several hours.

3.2.2 Cryostat System

The PL measurements made use of an Oxford Instruments MicrostatHe2 liquid helium flow cryostat. The cryostat allowed cooling and stabilisation of the sample to temperatures as low as ~4K. There were quartz windows at the bottom of the cryostat that allowed optical access to the sample. A schematic diagram of the cryostat and related control system is shown in Figure 3.2.

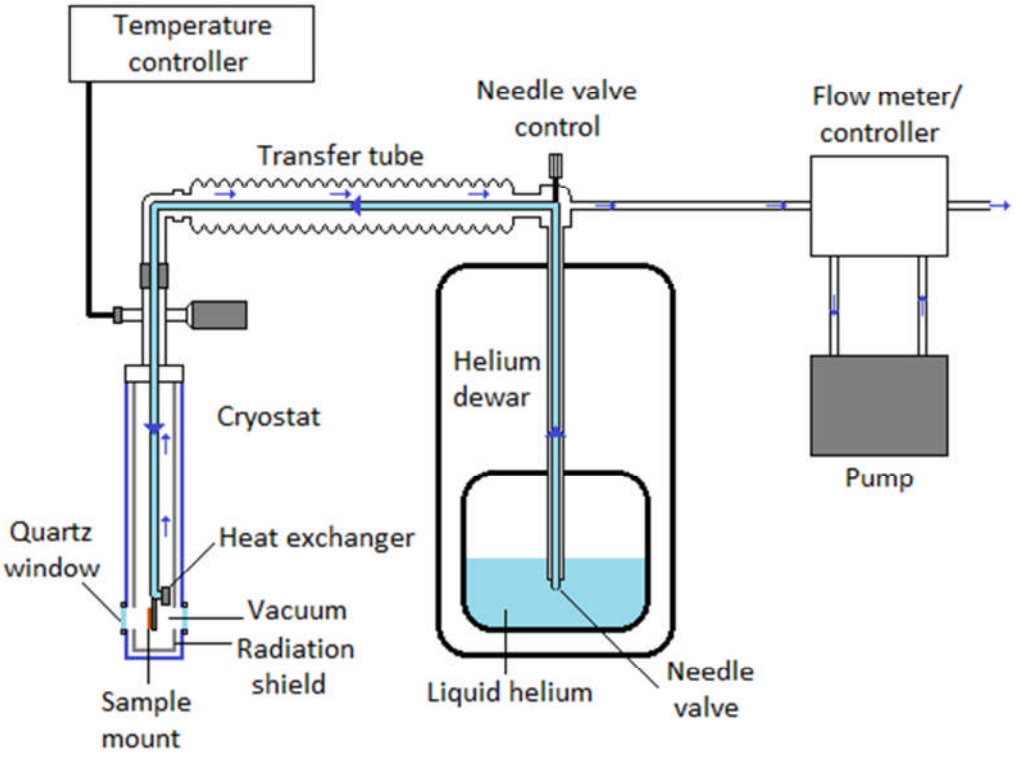

Figure 3.2: Schematic diagram of the cryostat system. Liquid helium flows from the dewar into the cryostat, where a temperature controlled heat exchanger maintains a stable temperature. Used helium gas is pumped out of the cryostat using the pump.

Prior to cooling, a turbo pump system was used to evacuate the cryostat to prevent moisture in the air freezing inside. The vacuum pressure achieved was typically under ~$5x10^{-5}$mBar. The cryostat was a continuous flow model that uses liquid helium transferred from an external storage vessel via an insulated tube. The helium flowed into the sample space through a heat exchanger, with the flow of helium around the sample cooling it. The used helium gas was removed from the cryostat using a vacuum pump, thus maintaining a continuous flow.

The heat exchanger had a thermometer and a heater attached to it, which were connected to a PID temperature controller. The heater could be set to raise the temperature of the sample above the minimum achievable. The flow rate of the helium could also be adjusted by opening or closing the needle valve on the transfer tube. This allowed the rate of helium use to be regulated.

3.2.3 Photoluminescence Technique

The experimental setup used for obtaining the PL spectra of samples is shown in Figure 3.3. The excitation source was a Ti-Sapphire pulsed laser, producing ~150fs duration pulses at a rate of 82MHz. The laser's wavelength could be tuned within the range 695-1050nm and had a typical output power of 0.5-1.0W.

The beam from this laser was directed into a frequency harmonic generator, which used non-linear crystals to generate harmonics of the beam with multiples of the input frequency. This could be configured to output second, third or fourth harmonics, allowing laser wavelengths of 210-350nm to be used for excitation of PL depending on experimental requirements. The output power from the harmonic generator varied as the wavelength was increased, from ~1.5mW at 210nm up to ~300mW at 350nm, but a sliding attenuator was used to control and maintain the beam power incident on the sample.

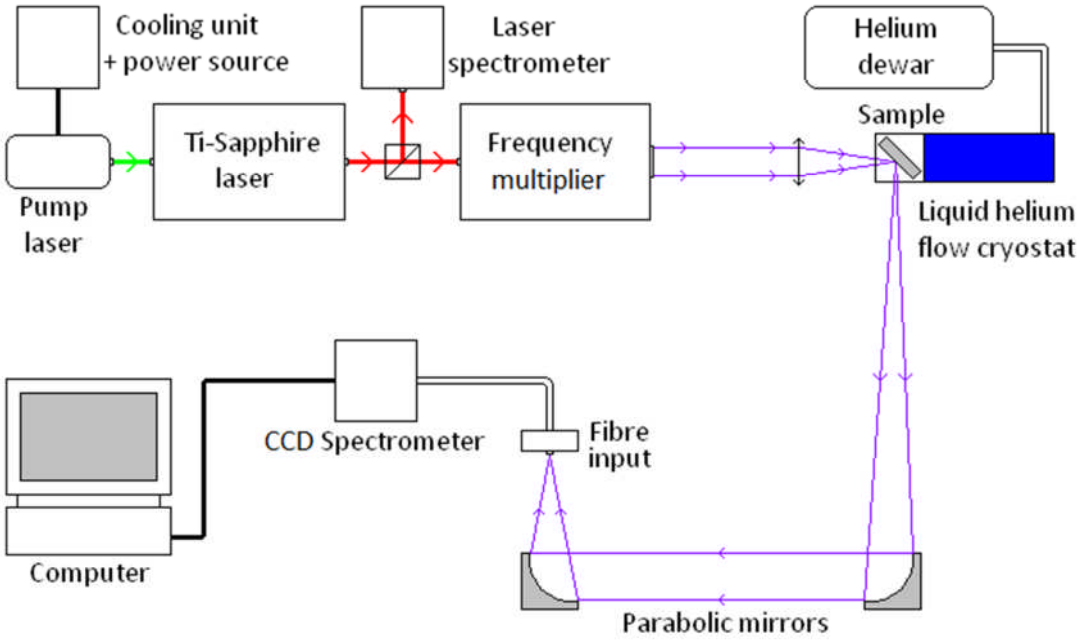

Figure 3.3: Experimental setup for measuring the PL of nitride samples. The frequency multiplier allows doubling, tripling or quadrupling of the laser frequency.

Upon exiting the multiplier, the beam was focused onto the surface of the sample held within the cryostat. The PL from the sample was collected and focused onto the optical fibre input using non-dispersive parabolic mirrors. Since no lenses were used for focusing, the effects of

aberrations were eliminated and all light wavelengths came into focus on the same point. A low pass edge filter with a cut-off wavelength between that of the laser and the expected emission region was placed in front of the fibre to remove laser emission from the measured spectrum.

Time-integrated PL (TIPL) spectra were recorded using an Ocean Optics UV enhanced spectrometer with a measurement range of 200-900nm. The operation of the spectrometer is demonstrated in Figure 3.4. The device contains no moving parts. Collected light enters via an optical fibre and is directed via a mirror onto a stationary diffraction grating. The grating diffracts different wavelengths by different angles. The dispersed light is directed onto a 3648 element linear CCD array with an individual pixel size of 8µm by 200µm. Each pixel collects a different wavelength of light and sends a digital response to the software. The spectral resolution was 1.5nm.

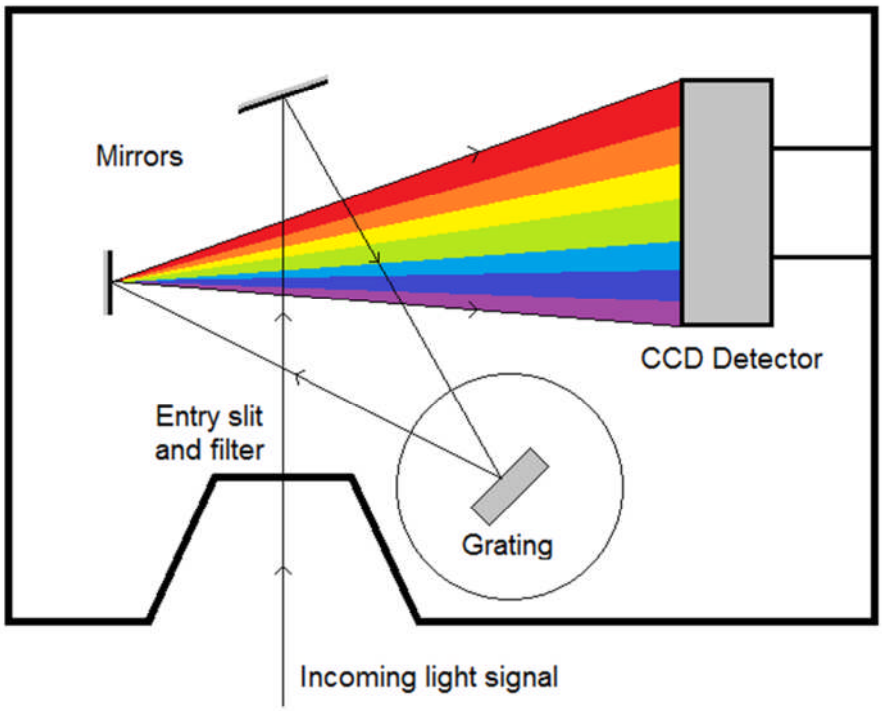

Figure 3.4: Schematic diagram showing the internal operation of the CCD spectrometer. Incoming light is diffracted by a grating before a mirror reflects each wavelength to a different part of the CCD array.

The spectrometer input to the computer was processed using manufacturer software, which subtracted the background signal from the spectrum. The software allowed the collection

time and number of averages to be changed. A well characterised GaN template sample with strong luminescence allowed the apparatus to be aligned by adjusting micrometer controls on the optics until the PL peak intensity was maximised.

3.2.4 Time-Resolved Photoluminescence

Time-resolved PL allows the temporal evolution of emission in response to a laser pulse to be directly measured. The methods of excitation and light collection are the same as for the time integrated case. The cryostat also allows the effects of temperature variation on the time evolution to also be observed. Conversion of the collected light to digital information is done in a different way. The experimental set up is shown in Figure 3.5.

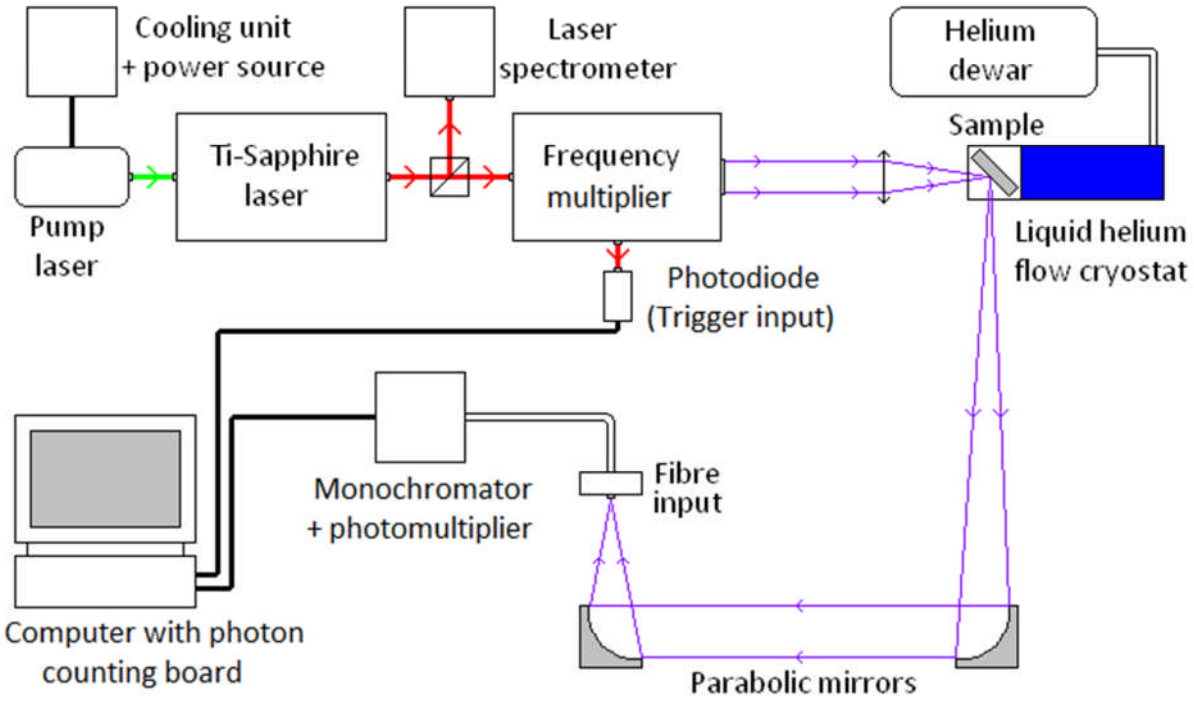

Figure 3.5: Experimental setup for time-resolved measurements. The apparatus is mostly the same as that used for time integrated readings. A monochromator and photomultiplier is used instead of a spectrometer. Photon counting at the PC is triggered by laser pulses.

Instead of a spectrometer that the collects the entire spectrum at once, a Bentham monochromator was used to isolate a single wavelength from the light entering the fibre. The internal operation of the monochromator is demonstrated in Figure 3.6. It has a mechanically

rotated grating that diffracts incident light, which is then directed onto an exit slit. The slit only allows a narrow part of the spectrum near a single wavelength to enter the detector. The selected wavelength is determined by the angle of the grating, set using an external stepper motor control. A resolution of 0.5nm could be achieved for a slit width of 2mm and a grating with 1800 lines/mm.

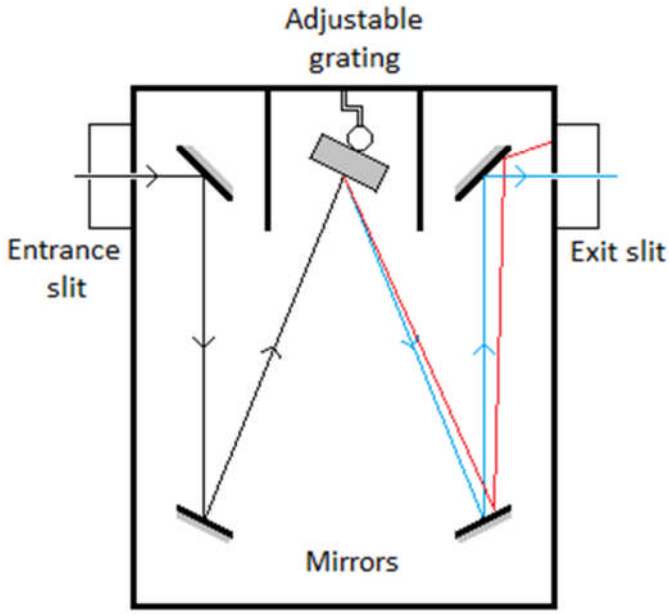

Figure 3.6: Schematic diagram showing internal light path through the monochromator used for time-resolved measurements. Only a single wavelength (blue beam path) is permitted to exit the device.

The near monochromatic light output enters a Becker and Hickl PMH-100-4 photomultiplier tube (PMT). Incoming photons impact a photocathode and cause electrons to be emitted from the cathode via the external photoelectric effect. These electrons are focussed on to a series of curved dynodes consisting of secondary emissive material on top of a metal substrate electrode. At each dynode, individual incident electrons cause multiple electrons to be emitted, which proceed to the next dynode and repeat the process. This causes the current to be amplified by orders of magnitude over the array of dynodes. An anode at the end of the tube collects the secondary electrons and outputs them to an external circuit.

The electrical detection signals are sent to the PC, which contains a Becker and Hickl SPC-630 time correlated single photon counting module. This board also receives signals from a photodiode correlating with the excitation laser pulses, and this acts a synchronisation signal (SYNC) for the photon counting process. The light intensity entering the PMT was limited

such that the chance of a photon being detected during one interval between SYNC pulses was only ~1%.

When a photon detection signal is received, the measurement board starts generating a voltage that ramps up linearly. When the next SYNC pulse arrives, the ramp is terminated, and the voltage is proportional to the time from photon pulse to SYNC pulse. By starting the time count on detection of a photon rather than after each SYNC pulse, the time-amplitude converter of the board has to work much less often than the laser repetition rate.

The time period between SYNC pulses is divided into 4096 memory addresses. The value at the memory address corresponding to the measured time is increased by an increment of one for each detected photon. Over many periods, a histogram of photon detection times is built up. This histogram corresponds to a time dependence of the PL intensity after the incidence of a laser pulse.

The single photon counting technique requires there to be only one photon per SYNC time period to work properly, so the light intensity entering the measurement fibre was kept beneath ~1M photons per second through the use of filters. The time-resolved decay curve builds continuously once the measurement has started as the results from successive pulses are summed. In order to achieve sufficient signal to noise ratio, a long measurement time (>60sec) was used for a typical measurement.

3.2.5 Infrared Photoluminescence for Measurement of Indium Nitride

The PL set-up described in Section 3.2.3 utilised a CCD spectrometer that was sensitive to wavelengths up to 900nm. Indium nitride possesses a very small bandgap of around ~0.8eV for the hexagonal structure. This corresponds to a wavelength of ~1550nm which sits beyond the sensitivity range of that spectrometer. PL measurements of InN hence required an alternative detector to be used.

We used a Hamamatsu G6122 infrared detector module with an InGaAs collection element. Although this detector was sensitive to the required wavelengths, it offered reduced functionality compared to the CCD spectrometer. With no in-built grating it lacked the ability

to differentiate between different wavelengths and simply converted incident light intensities into an electrical signal. The PL apparatus consequently had to be modified to include a method of wavelength selection and a means of converting electrical signals into spectral data. The modified setup is shown in Figure 3.7, which includes dispersive lens optics.

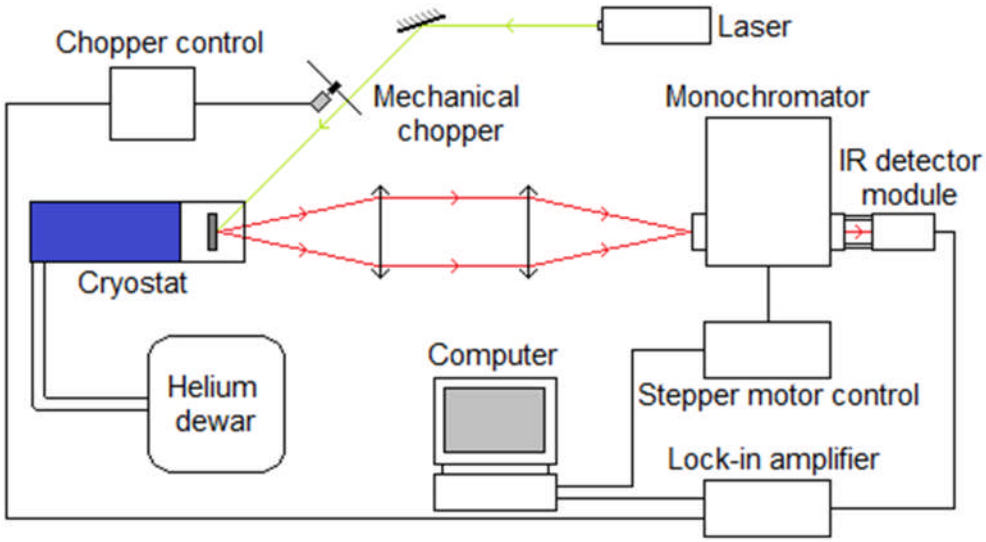

Figure 3.7: Experimental setup used for time integrated PL measurements of indium nitride samples.

The same Bentham monochromator used for the time-resolved PL measurements was used here to isolate a single emission wavelength. The external stepper motor that controlled the angle of the monochromator grating was connected to a computer running a Visual Basic program that automatically cycled through the wavelengths in a user defined range. In this way the PL emission at each separate wavelength could be collected. The control program allowed several averages to be taken over the space of several seconds for each wavelength increment, leading to high fidelity spectra to be collected at a cost of long measurement times.

The infrared detector outputted a very low voltage signal that was difficult to distinguish from background noise. The detector was thus connected to a lock-in amplifier. The lock-in amplified signals with the same frequency as a reference input, allowing separation of the signal from noise.

Due to experimental requirements and the higher emission wavelength, a different excitation source to the previous was also used, a green laser module emitting at λ=535nm. The laser beam passed through a mechanical chopper, a plastic wheel with alternating slits rotated by a motor. The intersection of the opaque parts of the wheel with the beam caused the beam to effectively start pulsing. The repetition rate was controlled by the rotation speed of the wheel's motor, which in turn was set by its control unit.

The control unit fed the modulation frequency of the laser to the lock-in amplifier as the reference input. The lock-in consequently only detected signals with same modulation frequency, which would consist of detector module outputs caused by PL emission only. Scattered and background light signals would not be recorded since they would not have the reference modulation.

The lock-in output signal was fed into the computer which plotted the signal voltage against the emission energy that had been set on the monochromator by the computer. Over time, the PL emission spectrum for the sample was built up by the computer for a programmed range of wavelengths.

3.3 Reflectivity Measurement

This measurement involves measuring the reflectance of a sample at wavelengths across a spectral range. For photon energies above the sample band gap, all incoming light is observed, leading to a cut-off in the reflectance spectrum. This measurement thus allows the band gap energy of a sample to be measured much more accurately than it can be from PL spectra.

The measurement procedure involves recording the emission spectrum of the light source and then the spectrum of this light after reflection from the sample surface. A fibre-coupled deuterium UV lamp was used as the light source for the experiment. This source had a small spot size and a broad spectrum with high light intensity in the UV range, a region in which the band gaps of the AlGaN samples could be found. The light being recorded was focussed onto the same fibre input and CCD spectrometer arrangement used for the time-integrated PL measurements.

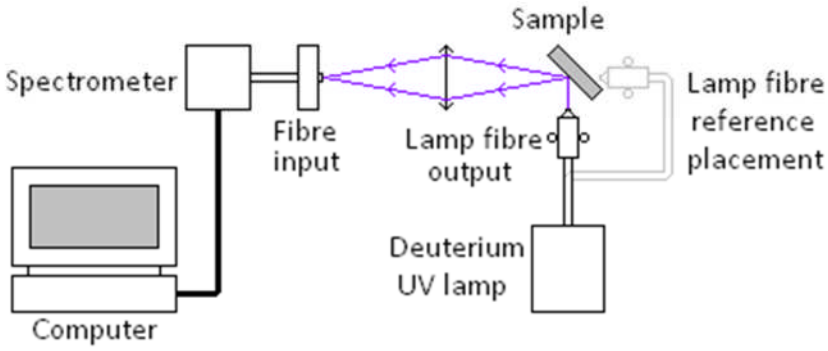

Figure 3.8: Experimental set up for reflectivity measurements. A spectrum was taken with the lamp fibre in the reference position, which had the same optical path length to the spectrometer as the measurement position.

The measurement was taken with the light shining on the sample at a 45 degree angle, as shown in Figure 3.8. Prior to this, a reference was taken without the sample and with the lamp fibre placed behind the sample's usual position, directly in line with the collection fibre input. The reference position was selected such that the optical path from lamp fibre to spectrometer was the same in both cases. This ensured that the effects of attenuation and alignment were minimised. The reflected light spectrum was divided by the saved reference spectrum to give the reflectance spectrum.

3.4 Surface Analysis: SIMS Measurement

Secondary Ion Mass Spectroscopy (SIMS) is a surface characterisation technique that allows the atomic composition of a layer to be determined. It was primarily used to determine the component fractions of ternary alloys and the concentration of dopants in doped materials. The results take the form of depth profiles showing the concentration of atom types per centimetre cubed against the depth through the layer. The measurements were performed externally by Loughborough Surface Analysis Ltd so only the general technique will be discussed here.

The SIMS measurement is performed in an evacuated vacuum chamber. An ion gun supplies a beam of high energy ions onto the sample. This ionises and sputters some ions off the surface. These secondary charged ions can be analysed using a mass spectrometer, which allows the proportion of different atomic types can be determined. The primary ion beam

consists of O_2^+ ions to detect positive ions such as magnesium and Cs^+ ions to detect negative ions such as silicon.

The dynamic SIMS technique used is destructive, resulting in a continuous etching away of the layer and pitting of the surrounding area. This distortion can lead to misrepresentative features on the composition curve, but the technique allows a depth profile to be obtained for the whole layer.

3.5 Transport Measurements on Doped Cubic GaN Layers

This measurement allowed the conductivity, carrier concentration and carrier mobility of electrically active layers to be determined. This experiment was carried out to test the electrical properties of doped cubic GaN samples. A sequence of readings was taken, including a Hall measurement according to the van der Pauw technique. The samples had to have contacts added in order to allow connections to the measuring apparatus. It was also necessary to remove the substrate, leaving very thin layers whose handling presented a significant challenge.

3.5.1 Sample Processing and Preparation

The samples consisted of small squares of material (5mm × 5mm) cut from the wafers. The aim of the study was to determine the electrical properties of cubic GaN layers. The presence of the GaAs substrate had the potential to compromise this measurement.

The difference in band gap between two semiconductor materials can lead to the formation of an inversion layer at the interface [83]. Excited carriers in the conduction band of the wider gap material move into the narrow gap material and leave a charge due to unscreened ions. Carriers in the narrow gap material are attracted by the charge but do not have enough energy to overcome the barrier and so become trapped near the interface.

The resulting high conductivity channel of carriers can interfere with an electrical measurement of the layer. For this reason the substrate had to be removed so the GaN layer could be measured on its own. The GaN layer was very thin (5-12μm) and so would be too fragile to handle or process on its own. The layer was hence stuck down to a ceramic mount

with protruding wires before substrate removal. The process, starting from as-grown sample is shown in Figure 3.9.

As with the samples for optical measurements, gallium droplets present on the sample surface were etched off first. In this case it was because droplets prevented good adhesion between the GaN surface and the ceramic mount.

The sample was also cleaned with the solvents ethyl lactate, acetone, methanol and isopropyl alcohol to remove dust and grease on the surface that could compromise the evaporated contacts. All samples brought into the clean room for processing were cleaned in this way.

The metal contacts were added next. These were designed to be low resistance Ohmic contacts to which wires could be adhered. They consisted of 50nm of indium capped with 100nm gold. They were applied in an Edwards E306A evaporator under vacuum conditions (1×10^{-6}mbar). A copper shadow mask with holes in the shape of triangles at the corner of a square was held over the sample to ensure that the contacts had this shape when applied.

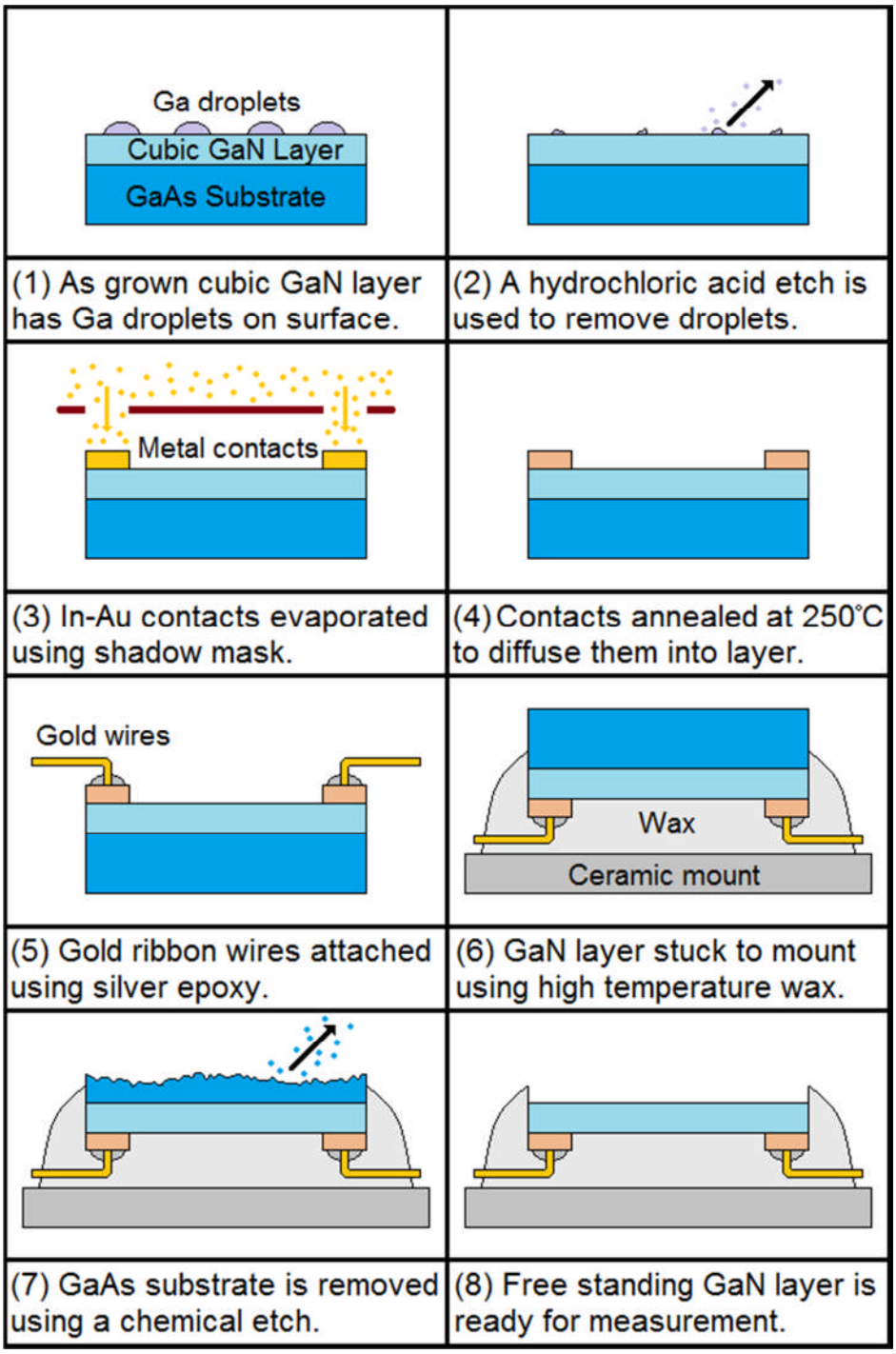

Figure 3.9: Illustration of processing stages for the preparation of doped cubic GaN layers for transport measurements.

After contact metallisation, the samples were annealed in order to diffuse the metal pads into the GaN layer and ensure good electrical contact. An unannealed metal-semiconductor interface may present a barrier to electron conduction due to the disparity between the metal's work function and the semiconductor's electron affinity [84].

The anneal was performed in an Anealsys AS-One rapid thermal annealer (RTA) under an atmosphere of 5% hydrogen and 95% argon. The sample temperature was ramped up to 250°C using an infrared halogen lamp, and held there for 30 seconds before cooling back to room temperature. The low contact resistance resulting from this method was verified on a test sample by putting down a row of four contacts and using a multimeter to ensure resistance increased linearly along the series of pads.

Gold tape wire with a width of 1mm was used for wiring since it was required to withstand the physical process of being glued down to the ceramic and subsequent handling. Epoxy Technology H20E-PFC 10Z conductive silver epoxy was used to attach the wires to the contact pads.

The sample was then attached, with the GaN layer face down, to a ceramic mount using high temperature wax. It was important to ensure that the wax surface in contact with the layer was flat in order to prevent cracking of the GaN during the substrate etch. The wax also had to encase the wire bonds completely to prevent the etching solution from removing the silver epoxy.

The entire mount with sample was left submerged in a solution consisting of one part phosphoric acid (H_3PO_4) to ten parts hydrogen peroxide (H_2O_2) for approximately 48 hours to etch away the GaAs substrate completely. An example of a sample after etching of the substrate is shown in Figure 3.10.

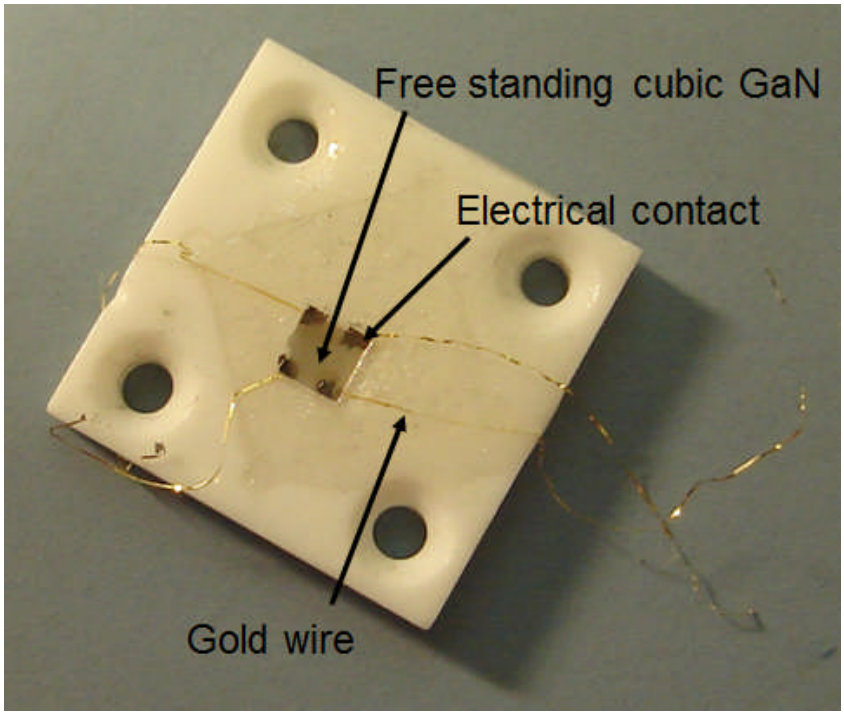

Figure 3.10: Photograph of processed Mg-doped cubic GaN layer separated from the substrate and attached to a ceramic mount using wax.

The electrical measurements were performed on some samples before and after substrate removal to ascertain what effect its presence had. The loose ends of the wires were attached to copper tracks on a header board to which the ceramic piece could be attached.

3.5.2 Transport Measurement

Once the contacts had been applied, they were tested by measuring the resistance between pairs of contacts with a multimeter. This also gave preliminary information about the conductivity of the layers.

The first stage of the transport measurement process involved measuring the sheet resistance. Voltage sourcing and current measurements were both performed by a Keithley 2400 sourcemeter operating in a four wire measurement mode. The terminals of the sourcemeter were connected to the sample contacts in one of two configurations, as shown in Figure 3.11.

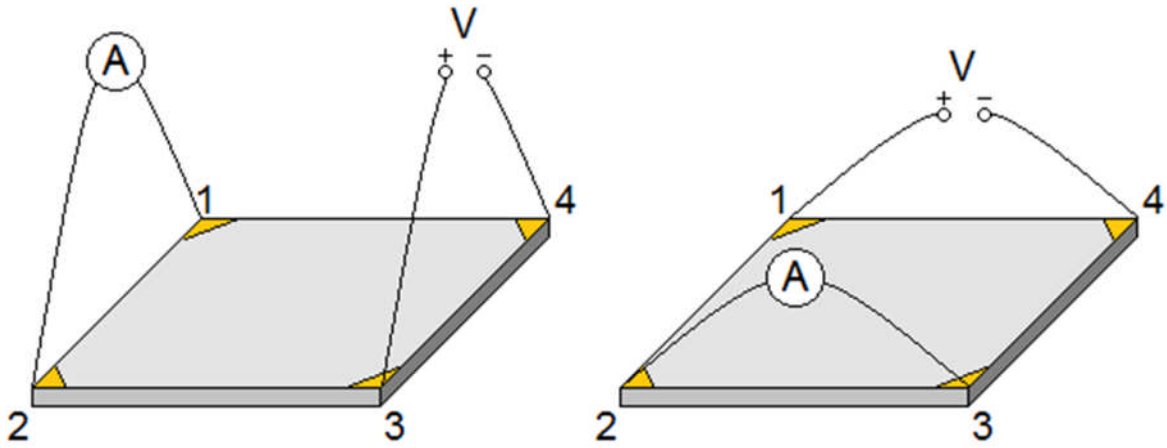

Figure 3.11: Diagram of contact arrangement for a van der Pauw sheet resistance measurement. In each case, a resistance was calculated from the applied voltage and measured current. These were combined via the van der Pauw equation to determine sheet resistance.

In each case, a resistance R_A or R_B was calculated from the applied voltage and measured current. These values are related to the sheet resistance R_S via the van der Pauw equation [85]:

$$e^{-\pi R_A/R_S} + e^{-\pi R_B/R_S} = 1\,. \tag{17}$$

The value of R_S was determined from this equation via an iterative solver in MATLAB. The bulk resistivity ρ was calculated from this result using:

$$\rho = R_S d \tag{18}$$

where, d – layer thickness.

The conductivity σ is hence given by:

$$\sigma = 1/\rho\,. \tag{19}$$

The next stage of the measurement involved determining the voltage that results from the Hall Effect. When charge carriers are flowing through a conducting bar which is subject to a constant magnetic field acting perpendicular to the direction of travel, they experience a Lorentz force that pushes them to one side of the bar. For electrons, this would lead to the

accumulation of negative charges on one side and the depletion of electrons on the other side, causing a positive charge to develop.

This charge separation results in a potential difference across the bar known as the Hall voltage, which can be measured using a voltmeter. The direction of the potential difference indicates whether the charge carriers are positive or negative, potentially identifying p or n type doping.

The terminals were wired to contacts on opposite corners, as illustrated in Figure 3.12. This measurement was performed using the sourcemeter to source a current across the first pair of terminals and measure a voltage across the other. The voltage reading was taken using a large number of averages to ensure that any Hall voltage was distinguishable from noise fluctuations.

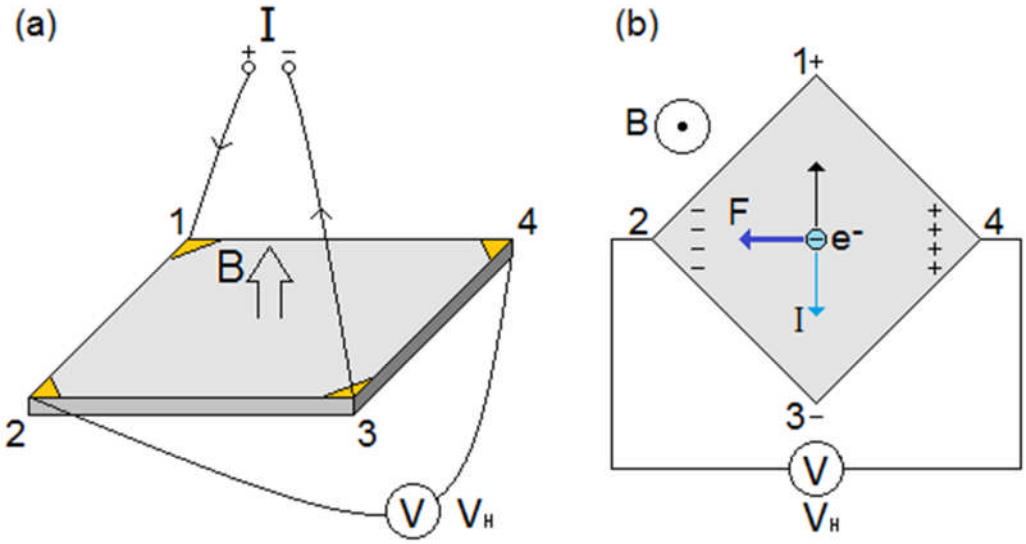

Figure 3.12: (a) Diagram of contact arrangement for Hall measurement. (b) Illustration of Hall Effect within the sample for negative charge carriers. Electrons flowing from contacts 3 to 1 experience a force pushing them towards terminal 2 due to the presence of the magnetic field, leading to the build-up of a potential difference across the sample.

The magnetic field was provided by a 0.3T horseshoe magnet. Samples were mounted on a copper header with shielded cables held by a clamp stand that allowed the sample to be slid in and out of the magnetic field. The voltage across the sample (V_{24}) was measured prior to the magnet being introduced in order to measure any inherent voltage due to inhomogeneities

within the sample. The sample then went into the magnet for a second voltage reading before the magnet was rotated to invert the field direction for the third voltage reading. The average difference in measured voltage between when the magnet was and was not present equated to the Hall voltage V_H.

The Hall voltage equates to the applied magnetic field B via the following expression that allows the density of carriers, n to be determined [86]:

$$V_H = \frac{IB}{nqd} \tag{20}$$

where, I – current (perpendicular to Hall voltage)

d – sample thickness.

Using the carrier density, the carrier mobility μ can be calculated:

$$\mu = \frac{\sigma}{nq} \tag{21}$$

where, σ – conductivity.

By measuring the sheet resistance and the Hall voltage of a sample, its carrier mobility can hence be found. The carrier mobility is an important quantity for characterising electrically active materials.

3.6 Sample Imaging Using the Scanning Electron Microscope

The scanning electron microscope (SEM) is an instrument that uses a beam of electrons to image sample surfaces. The SEM offers higher resolution than optical microscopes due to the smaller wavelength of electrons compared to sample features [87]. It was used to capture images of the surface of doped cubic GaN layers in an attempt to learn about the morphology and underlying structure.

In the SEM a beam of electrons is emitted from an electron gun and accelerated through an anode towards the sample. A series of magnetic field coils is used in the place of lenses for beam focusing. The interior of the SEM is under a high vacuum to prevent scattering of

electrons off of air molecules. The electron beam is focused into a narrow line that is scanned across the sample.

The electron beam knocks off secondary electrons. These are drawn to a collector wire mesh held at a few hundred volts. These captured electrons are accelerated into a scintillator that generates light which is converted into an electrical signal using a photomultiplier tube. The current of secondary electrons changes across the specimen due to the surface topography and this varying current is used to modulate the final image.

The system used was a JEOL 7000F thermal field emission SEM offering an optimal imaging resolution of 4nm, although this was not achieved or necessary for this work. The sample mount was capable of holding 5mm × 5mm sample pieces. Conductive clips were attached to the conducting surface of the sample to provide a ground connection. This prevented a build-up of negative charge on the surface due to the electron beam [88].

The sample mount was inserted into an exchange unit where the sample was brought to high vacuum before being moved to the imaging position. A short scan time narrow field view was used to optimise focus before high resolution images were captured and saved to the PC.

3.7 Conclusion

We have presented the experimental techniques and equipment used to obtain the results found within this thesis. Molecular beam epitaxy has been used to grow all nitride samples. Their optical properties have been assessed using photoluminescence and reflectivity measurements. Electrical properties have been studied using Hall measurements, for which sample processing was required. To complement optical and electrical measurements, scanning electron microscopy has been used to image sample surfaces.

Chapter 4: Characterisation of Cubic AlGaN Bulk Layers and Structures

This chapter will present the results of characterisation studies of structures containing the cubic ternary alloy AlGaN. Initially, bulk layers of cubic $Al_xGa_{1-x}N$ with different fractions, x of aluminium were studied. The next stage was the growth and characterisation of single AlGaN/GaN/AlGaN quantum well structures, an important step towards device applications.

4.1 Study of Bulk Cubic $Al_xGa_{1-x}N$ Layers

The aim of this work was to assess cubic $Al_xGa_{1-x}N$ grown in the MBE system at Nottingham and to study how recombination dynamics changed over the full range of aluminium fraction (x). A set of ten wafers of cubic were grown with different aluminium fractions, starting from pure GaN. PL spectra and time-resolved PL decays were recorded at temperatures between ~4K and room temperature.

Sample	Nominal AlN fraction (x)	Al effusion cell temperature (°C)	Measured AlN fraction (x)	Film thickness (μm)
SN-433	0	0	0	0.466
SN-437	0.1	945	0.08	0.460
SN-434	0.2	975	0.16	0.428
SN-442	0.3	996	0.23	0.465
SN-435	0.4	1007	0.29	0.411
SN-438	0.5	1020	0.42	0.463
SN-444	0.6	1028	0.49	0.424
SN-439	0.8	1043	0.66	0.444
SN-441	0.9	1049	0.78	0.391
SN-440	1.0	1054	0.95	0.361

Table 4.1: This table shows sample specifications for Cubic $Al_xGa_{1-x}N$ Wafers. The measured aluminium fraction was determined using SIMS measurements.

These films were grown using the technique discussed in the previous chapter (Section 3.1), at a growth temperature of 680°C and a rate of 0.25μm per hour. Different levels of aluminium incorporation were achieved by varying the temperature of the aluminium effusion cell. The specification for each of the samples, shown in Table 4.1, quantifies the desired AlN fraction in each case with the actual fraction measured using SIMS.

4.1.1 Effect of Gallium Droplet Etch

The cubic $Al_xGa_{1-x}N$ layers featured droplets of gallium on the surface as a result of the growth process, examples of which were shown in Section 3.2.1. To determine the effect that these droplets had on the PL results, spectra were taken on the x = 0.95 alloy before and after the acid etch that removed the droplets. The spectra are shown in Figure 4.1.

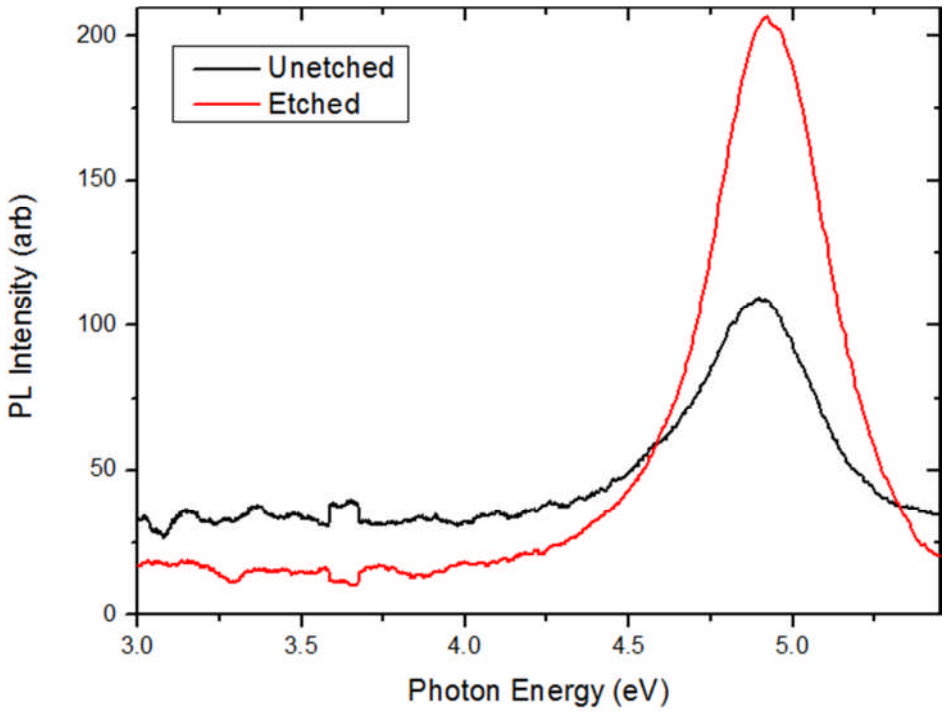

Figure 4.1: PL spectra taken for $Al_{0.95}Ga_{0.05}N$ wafer before and after the etching of gallium droplets from the surface.

The same main peak can be observed in both spectra, indicating that the feature was due to emission from the bulk $Al_{0.95}Ga_{0.05}N$ film and not from the surface droplets. The disparity in intensity is likely the result of stronger emission from the cleaner surface as well as changes in the alignment of the measuring system between measurements.

4.1.2 Photoluminescence Spectra

The PL spectra recorded at room temperature for the full set of $Al_xGa_{1-x}N$ wafers are shown in Figure 4.2. A single broadened peak is recorded for each sample, attributed to the near

band edge emission from the cubic material. There is no peak present due to hexagonal inclusions, indicating that the nucleation and growth have been well controlled.

Increasing incorporation of aluminium across the range is verified by the shift of peak energy upwards starting from pure GaN as the band gap energy is increased. The band gap energy for a ternary alloy system is expected to follow Vegard's law, where the linear transition between the bandgap energies of the two binary alloys is adjusted by a bowing parameter, b. The band gap energy at an aluminium fraction x is given by [89]:

$$E_G(x) = (1-x)E_G(GaN) + xE_G(AlN) - bx(1-x) \quad (22)$$

where, E_G(GaN) – GaN bandgap energy

E_G(AlN) – AlN bandgap energy.

The integrated intensity of PL emission was considerably higher in the high AlN fraction wafers. The enhancement of PL efficiency has been attributed to carrier localisation [90]. The non-uniform distribution of aluminium throughout the layer results in regions of varying alloy fractions. These nanoscale compositional inhomogeneities (NCIs) lead to spatial bandgap fluctuations. Carriers become trapped, or localised on these fluctuations and thus prevented from travelling to defects and sites where they can recombine non-radiatively.

NCIs have been deliberately incorporated into hexagonal AlGaN layers in order to improve emission efficiency, whilst dislocations and impurities were associated with causing non-radiative emission [91].

The density and variety of the NCIs is expected to be greatest at around 50% aluminium concentration, when the broadest distribution of elements is present. Studies on hexagonal AlGaN have identified the point of maximum localisation as being at slightly higher AlN fraction [92]. This was attributed to the decrease in exciton Böhr radius with increasing x [93]. The reduced radius effectively makes the exciton more sensitive to smaller alloy fluctuations.

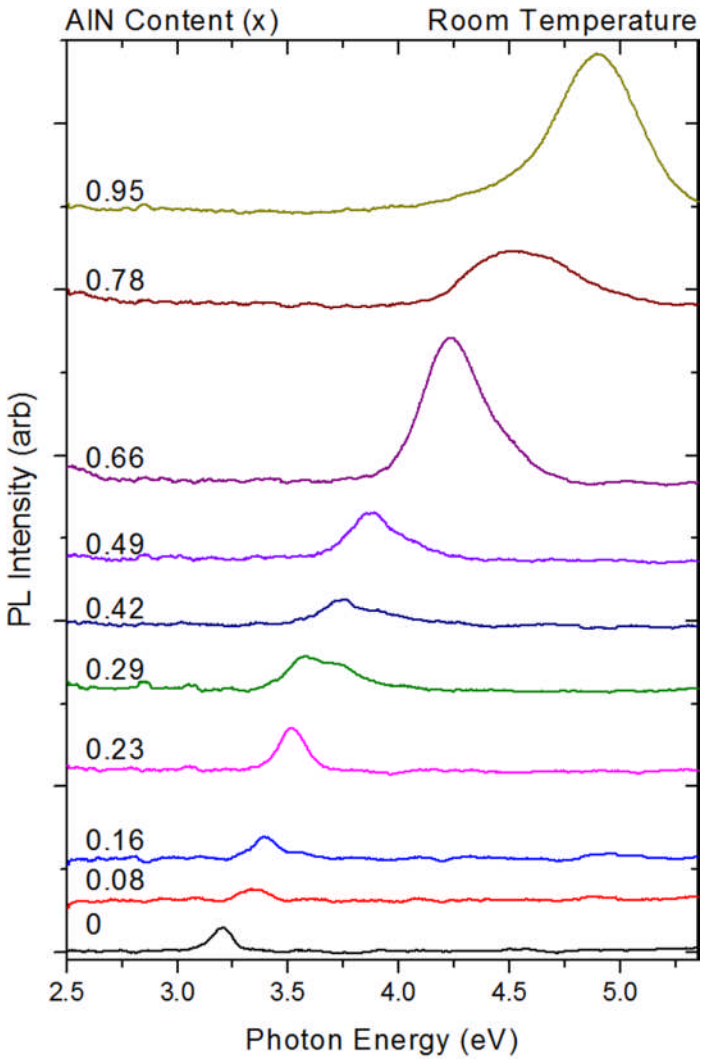

Figure 4.2: Time integrated PL spectra for cubic $Al_xGa_{1-x}N$ wafers with varying AlN fraction, taken at room temperature.

The PL spectra for the $Al_xGa_{1-x}N$ layers taken at low temperature (T=4K) are shown in Figure 4.3. The PL intensity at low temperatures is significantly improved due to the temperature quenching effect at higher temperatures. Carriers gain energy as the temperature increases and use this to escape localisation traps and travel to sites where non-radiative recombination can occur, reducing light emission.

Unlike the room temperature spectra, in the low temperature results, multiple spectral peaks are visible. In the case of pure GaN, the main peak at 3.15eV has been attributed to near band edge donor-acceptor (D^0-A^0) recombination between band tail impurities [94]. The origin of the line at 3.07eV is less clear, but may be due to a transition involving an arsenic acceptor impurity [55]. A small peak appears on the high energy edge of the main feature at 3.26eV.

This has been identified as the combined emission of free and bound excitonic recombinations [30].

The samples just under the midpoint of the alloy range (x = 0.29-0.49) exhibit extended shoulders and peaks on the higher energy side that are not as prominent on other samples. These features are likely due to excitonic features but may also indicate hexagonal inclusions. The most prominent tail occurs for x = 0.49, one of the thickest films in the set. Thicker layers are known to be more likely to include hexagonal features, but the variation in width of the sample set is fairly small whilst significant changes are seen in the PL spectra.

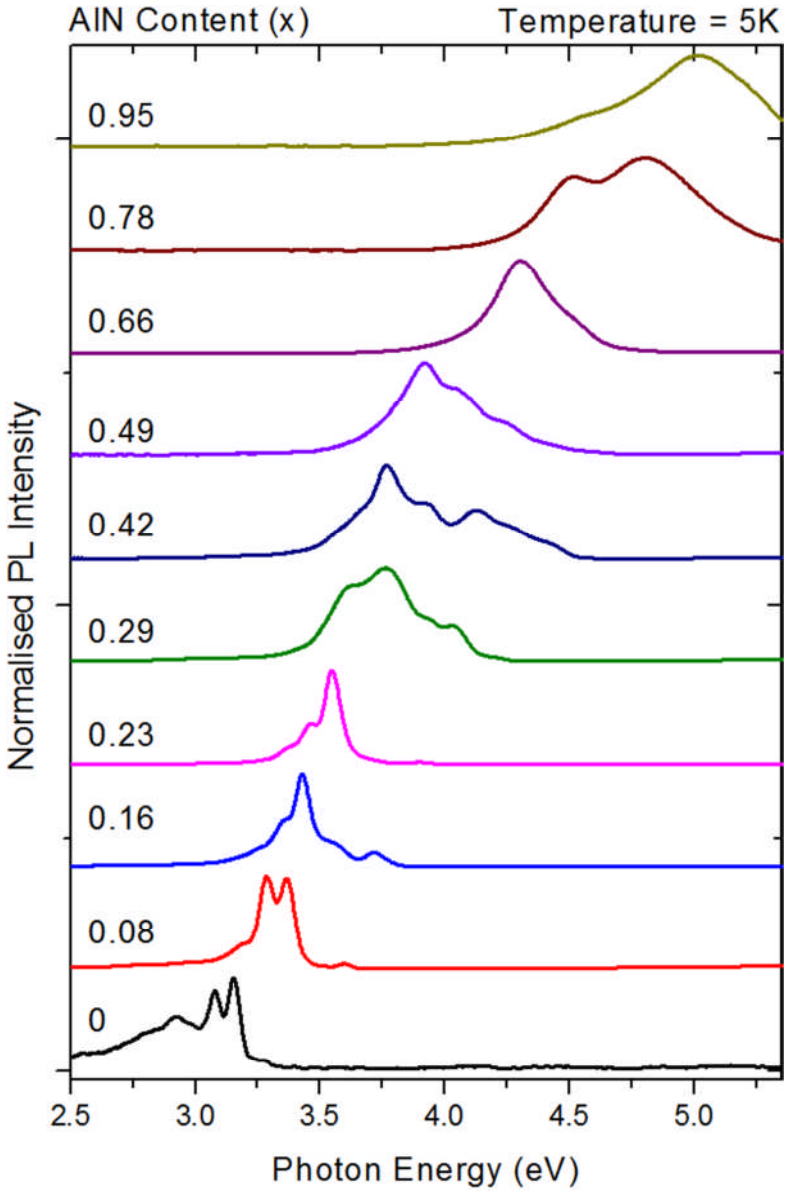

Figure 4.3: Low temperature PL spectra for cubic $Al_xGa_{1-x}N$ sample set. The spectral intensity has been normalised to add clarity to spectral features.

The integrated PL intensity is significantly higher at the larger AlN molar fraction, and does not peak just above the middle of the range. This result suggests that carrier localisation increases as more aluminium is added. This outcome is unexpected if localisation is solely attributed to alloy compositional inhomogeneities. Other defects or impurities that are related to aluminium incorporation are therefore likely to be acting as localisation sites and contributing to enhanced luminescence via localisation as well.

As the AlN fraction increases, the spectral features become broader, merging into a single peak in some cases. In the wafers with more aluminium, the increased amount of fluctuations and inhomogeneities and the presence of greater numbers of defects and impurities allow recombinations with a broader range of energies to occur. This broadening effect has also been observed in the $Al_xGa_{1-x}As$ system [48].

The spectra for the $Al_xGa_{1-x}N$ films were recorded at regular intervals across a range of temperatures in order to determine the effect of temperature on the luminescence. Examples of the temperature dependent spectra for alloys near the extremities of the AlN fraction range are shown in Figure 4.4.

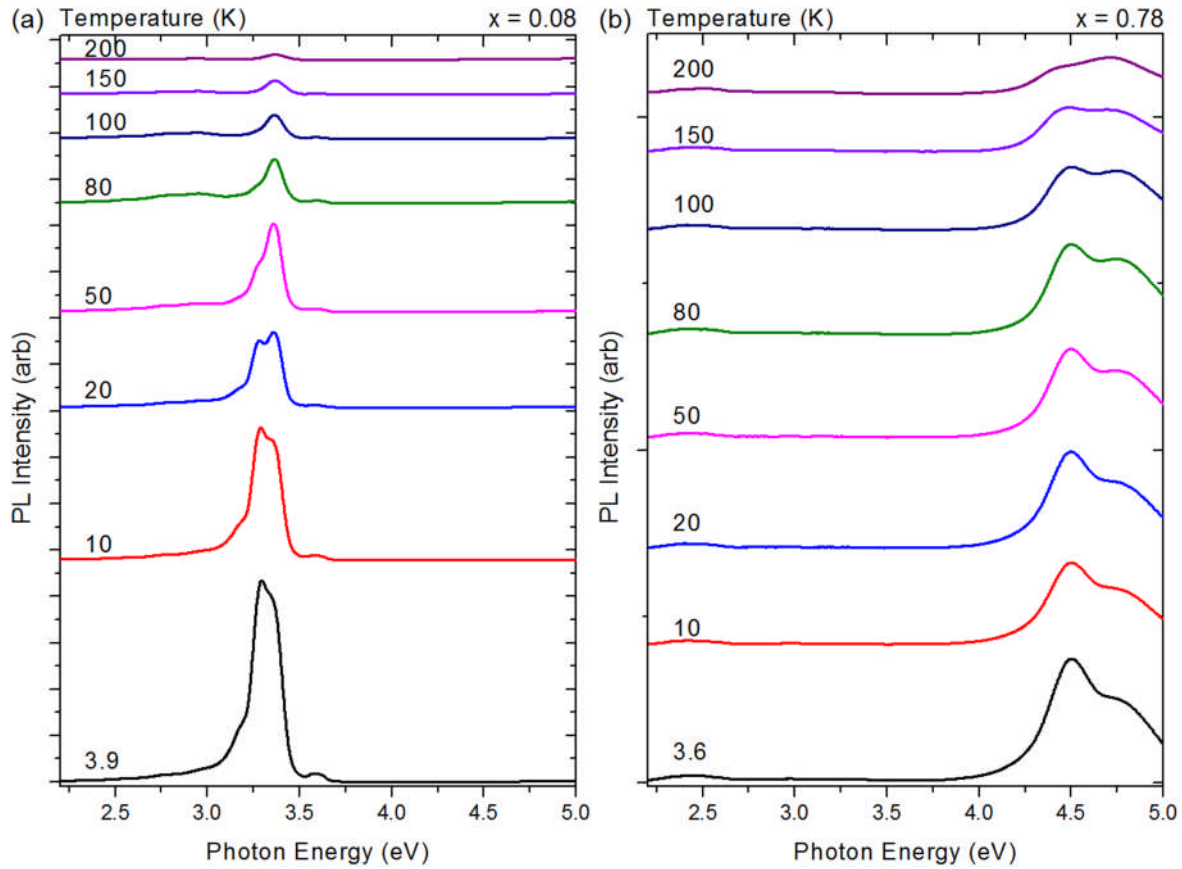

Figure 4.4: PL spectra recorded at a range of temperatures for cubic $Al_xGa_{1-x}N$ wafers with AlN fractions of (a) x = 0.08 and (b) x = 0.78.

The temperature quenching leads to a much more rapid decrease in the emission intensity in the lower AlN fraction layer. The integrated PL intensity as a function of temperature has been plotted for all the alloys in Figure 4.5. The intensity falls away more slowly with increasing temperature as the amount of aluminium increases. In addition to the changes in intensity, the distinct line features of the lower AlN fraction spectrum are lost as the shape changes to a broad line whilst the line shape of the high AlN fraction spectrum is similar across the temperature range.

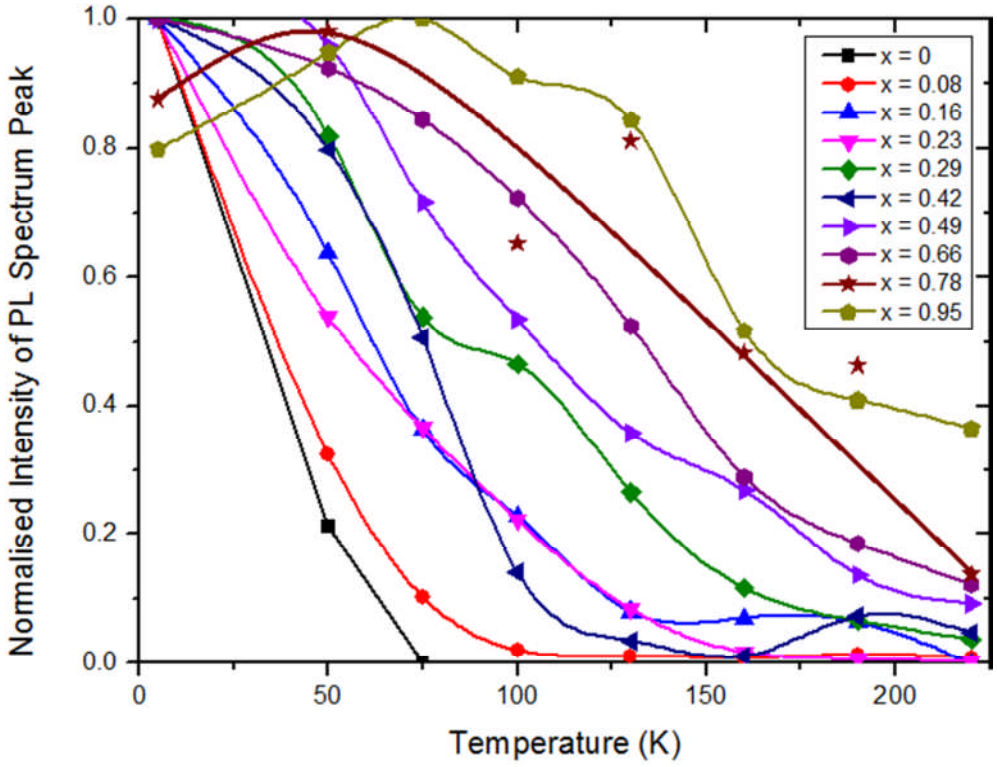

Figure 4.5: Plot of integrated PL intensity against temperature for cubic $Al_xGa_{1-x}N$ films with different AlN composition. The lines are intended as guides for the eye.

These effects also suggest there is a greater degree of localisation with more aluminium in the alloy. The carriers that are more strongly localised require more thermal energy to be put in before they have enough to escape to the extended and non-radiative sites, causing the PL intensity to decrease more slowly as the temperature increased. The lineshape of the high AlN fraction spectra is preserved as emission continues from the same localised sites.

The energy required for carriers to become unbound from localised states and be able to travel to sites of non-radiative recombination is called the activation energy, ΔE. A larger activation energy indicates that the binding energy is greater [89]. This can be calculated from the variation of integrated intensity against temperature by utilising the Arrhenius equation [95]:

$$I_{PL}(T) = \frac{I_0}{1 + Ce^{-\Delta E/KT}} \tag{23}$$

where, I_0 – PL intensity at zero temperature

C – a constant related to the kinetics of electrons and holes.

For each alloy, the integrated PL intensity was plotted against inverse temperature and the curve was fitted by a modified version of the above expression:

$$\frac{I_{PL}(T)}{I_{PL}(T_{min})} = \frac{1 + Ce^{-\Delta E/KT_{min}}}{1 + Ce^{-\Delta E/KT}} \tag{24}$$

where, T_{min} – the lowest temperature at which the spectrum was recorded.

Examples of Arrhenius plots are shown in Figure 4.6, along with the fitted curves of Equation (5) as calculated by MATLAB. As can been seen on the plots, there is good agreement between the experimental data and the fit.

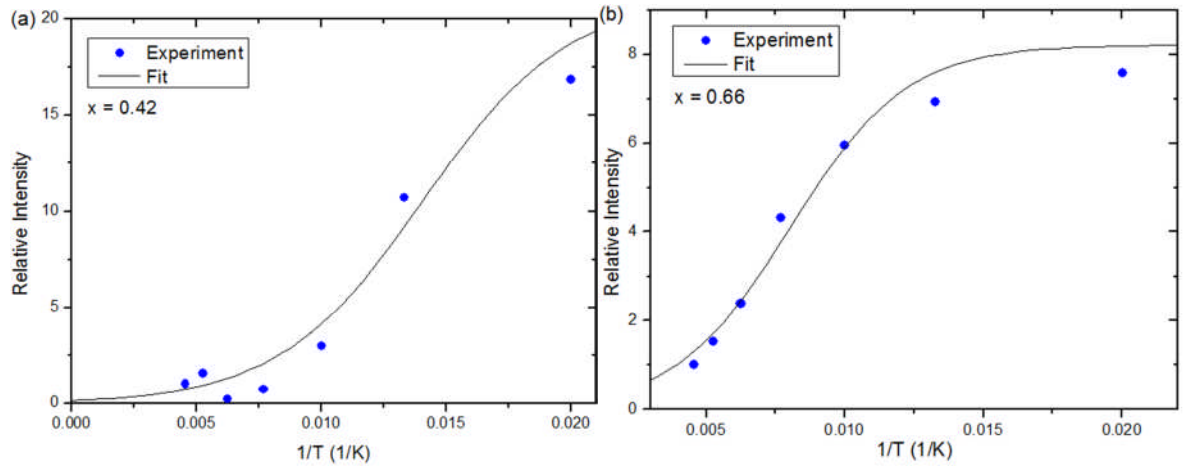

Figure 4.6: Plot of the integrated PL intensity against inverse temperature for cubic $Al_xGa_{1-x}N$ wafer with AlN fraction of (a) x = 0.42 and (b) x = 0.66. The data has been fitted using the Arrhenius equation.

The activation energy calculated for each film has been plotted against the aluminium fraction in Figure 4.7. The activation energy evidently increases linearly as more aluminium is added. The activation energies at the higher end of the scale exceed KT, even at the highest temperature, indicating the carriers would still be mostly localised due to insufficient thermal energy to escape. The trend supports the assertion that the degree of localisation is increased in the high x samples due to inhomogeneities, defects and impurities.

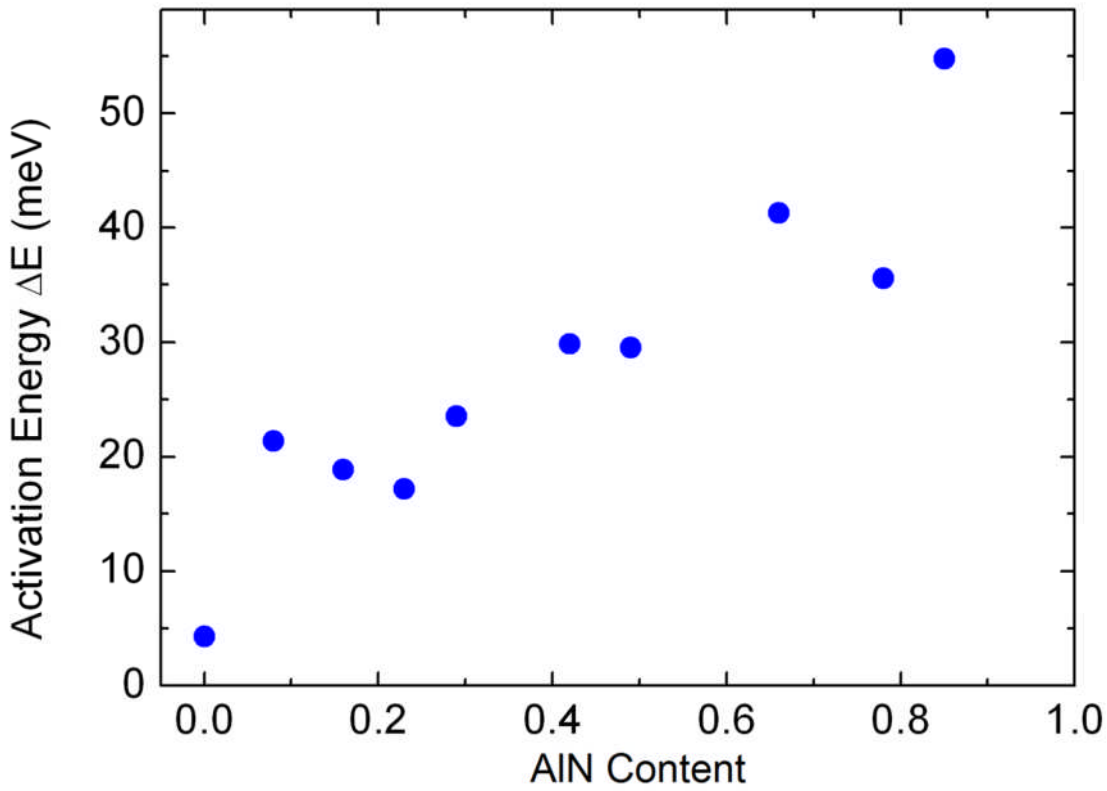

Figure 4.7: Graph of activation energy against AlN fraction for cubic $Al_xGa_{1-x}N$ layers.

The variation of the PL peak emission energy across the temperature range is shown in Figure 4.8. Generally, as the temperature was increased, the emission energy decreased slightly. This behaviour was expected due to bandgap shrinkage that is known to occur in semiconductors. Thermal expansion and changes in lattice vibrations due to increased temperature lead to a modification in the lattice constant and hence the bandgap. The dependence of the bandgap energy is described by the Varshni formula [96]:

$$E_G(T) = E_G(T=0) - \frac{\alpha T^2}{\beta + T} \tag{25}$$

where, α and β – Varshni thermal coefficients.

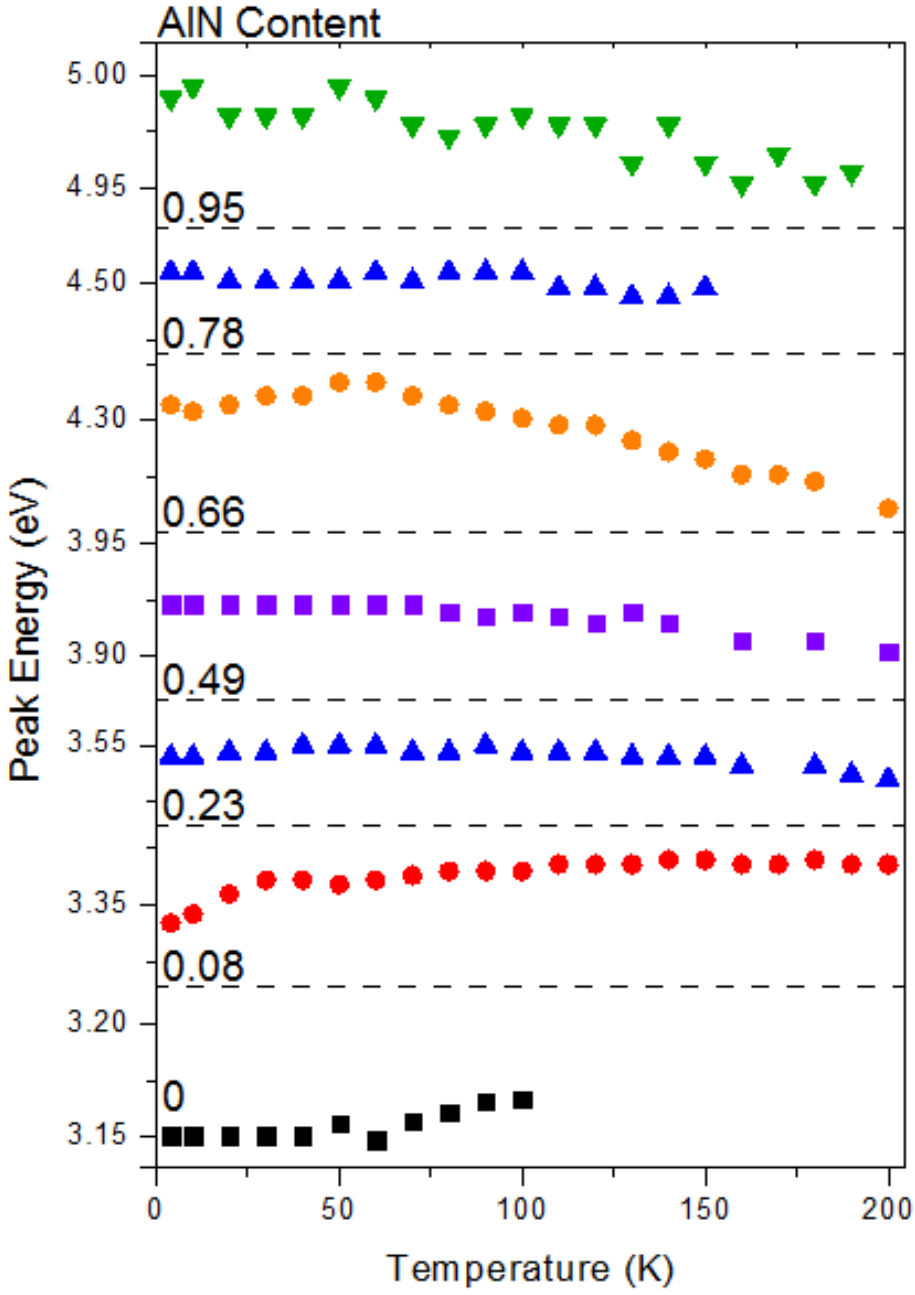

Figure 4.8: Plot of PL peak energy against temperature for cubic $Al_xGa_{1-x}N$ wafers with different AlN concentrations.

Various studies of hexagonal $Al_xGa_{1-x}N$ have identified a more complex variation in the PL emission energy [93, 96, 97]. They observed an "s-shift" temperature dependence, in which as the temperature is increased, the energy initially decreases before increasing for a period and then decreasing again. An example of this variation is illustrated in Figure 4.9, with the three separate behaviour regions shown.

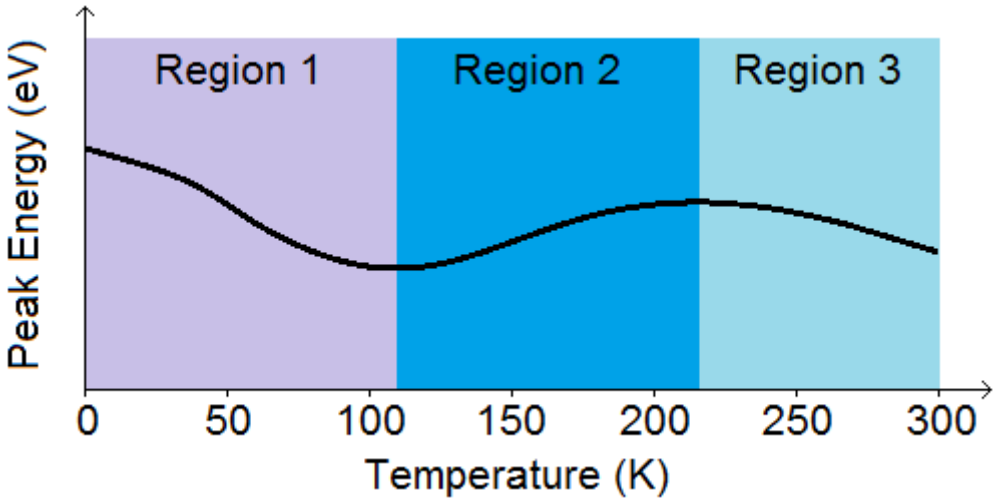

Figure 4.9: Example variation of PL peak energy against temperature showing the s-shift effect. The three different regions of different behaviour are highlighted.

The phenomenon is attributed to exciton localisation. The initial redshift of region one is due to emission from recombining excitons that move to deeper localised sites via hopping transport. As more thermal energy enters the system, the excitons move to higher energy states before recombining, and this leads to an emission energy blueshift in region two. At higher temperatures in region three, the bandgap shrinkage effect dominates and redshifting again occurs.

The Varshni formula has been modified to describe the s-wave process by adding an extra term that is related to localisation [93]:

$$E_G(T) = E_G(T=0) - \frac{\alpha T^2}{\beta + T} - \frac{\sigma^2}{K_B T} \tag{26}$$

where, σ – localisation parameter corresponding to the standard deviation of the Gaussian distribution of potential fluctuations.

The s-shift has been observed to correlate with the degree of localisation, with the shift becoming more pronounced and the changes in shift direction occurring at higher temperatures for more localised layers. The localisation parameter, calculated by fitting the above expression to the PL data, was found to correlate with the AlN fraction in hexagonal material. The studies did not however consider the higher levels of AlN concentration (>70%).

The results obtained from our cubic $Al_xGa_{1-x}N$ layers, shown in Figure 4.8 do not show clear s-shift behaviour at any of the AlN concentrations measured. The curves for samples in the middle of the range have the closest resemblance, with a short initial increase followed by a peak at around T = 60K for the alloy with 66% aluminium. This is around the concentration at which localisation was found to be highest in hexagonal AlGaN, but earlier results from our samples indicated maximum localisation at the highest AlN fraction. The broad nature of the peaks often made identification of the maximum point difficult, so the energy values given may not be highly reliable.

Given the very high activation energy it may be possible that the characteristic transition temperatures associated with the s-shift occur outside of the range of measurement and that only sections of the s-shift are visible. This could explain why a rise in emission energy is seen at low alloy contents whilst near flat variations or gradual decreases are seen for the other alloys. Data covering a wider range of temperatures are necessary for further clarification, but these results may indicate very pronounced localisation behaviour up to high temperatures in these alloys.

4.1.3 Time-resolved Photoluminescence

Time-resolved measurements allow the temporal evolution of PL emission intensity from the $Al_xGa_{1-x}N$ wafers to be recorded. Decay curves that showed the time dependent emission of a sample after a single laser pulse were measured for the full range of alloys at different temperatures. The PL emission of only one single chosen photon energy (and a very narrow range around it) could be studied, so readings were taken at energies corresponding to the maximum of the dominant donor acceptor peak as well as points on the sides of the peak.

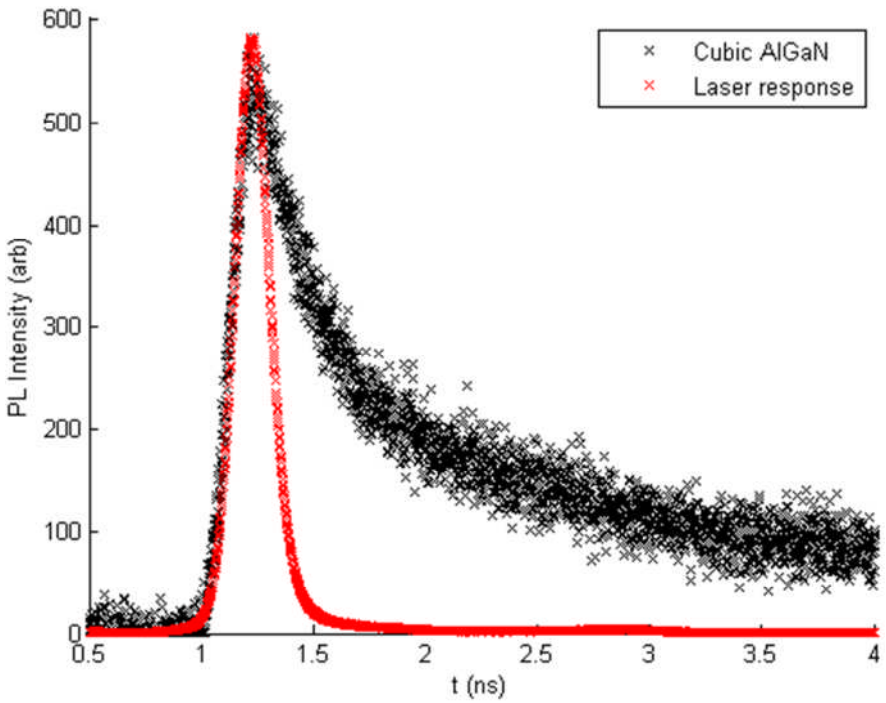

Figure 4.10: Plot of PL emission intensity against time for cubic $Al_{0.08}Ga_{0.92}N$ layer at T=50K and photon energy of 3.27eV. The decay curve for emission at the laser wavelength is also shown.

An example of a decay curve for one of the low AlN concentration layers is shown in Figure 4.10. The recorded emission at the laser wavelength is also shown and this corresponds to the scattered laser light from the sample. The laser line indicates the fastest possible response of the measurement system and hence the temporal 'resolution limit' that can be measured. Decays that were faster than the fall off of laser light intensity were hence not detectable.

The PL emission from the nitride layer increases rapidly with the rising edge of the laser pulse as excited carriers begin to recombine. When the laser excitation ends, the sample emission decays away slowly as more energetic carriers relax and spatially separated carriers converge before recombining.

The rate at which the intensity decays is related to the degree of localisation within the material, as illustrated in Figure 4.11. The various alloy fluctuations, impurities and defects cause carriers to be localised at various points in space. Electrons and holes localised in the same region are able to recombine quickly with a characteristic decay time. If the carriers are localised on sites that are spatially separated, the recombination takes longer and the emission

decay time is extended. When a broad range of localisation sites with different energies and separated by different distances are present, multiple recombinations contribute to an extended and non-exponential decay.

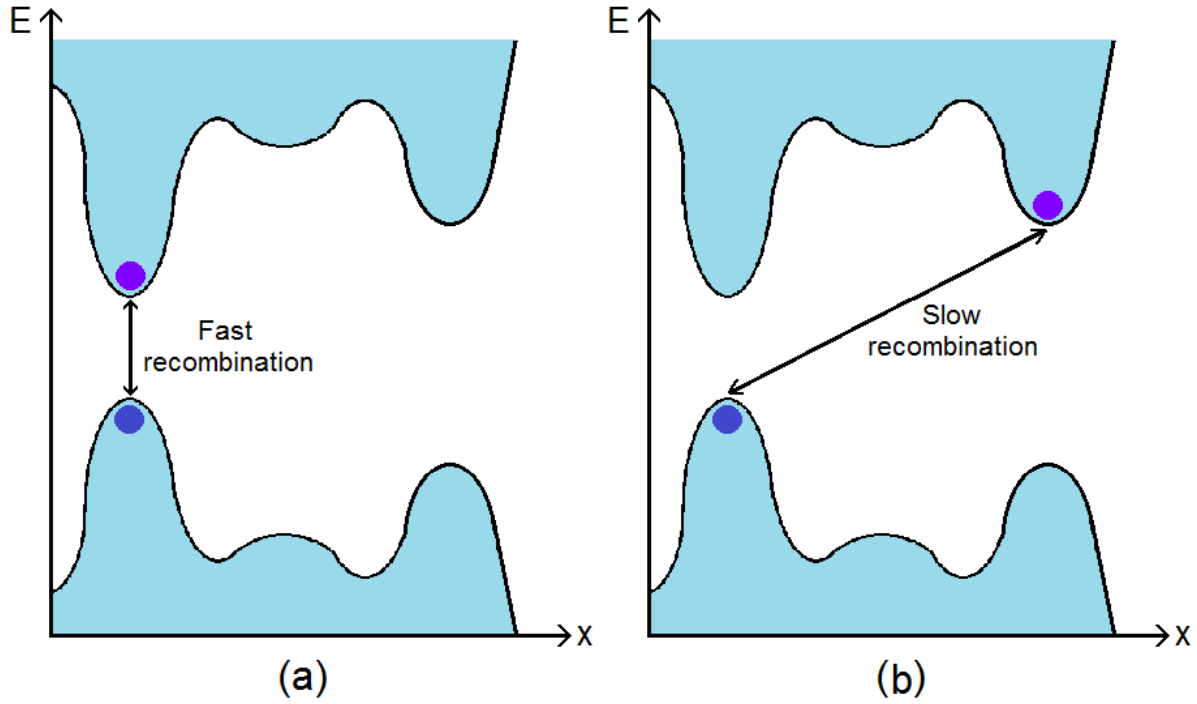

Figure 4.11: Illustration of carrier localisation model and its effect on recombination times. (a) Carriers localised in the same region of space are able to recombine more quickly than (b) those localised in separated regions.

Carriers preferentially recombine radiatively or non-radiatively based on which process is fastest. At higher temperatures, the non-radiative process becomes fastest, resulting in lower PL emission intensity and lifetime [45, 96, 98]. This occurs because carriers gain energy to escape the localised sites and travel to centres where non-radiative recombination can occur, such as impurities or defects.

In order to identify trends in the PL decay behaviour due to changes in temperature and aluminium fraction, a decay constant, τ, corresponding to the time taken for the PL intensity to fall to 1/e of its peak value was calculated from each curve. This was done by fitting the following exponential function to the decay side of the time-resolved peak:

$$I(t) = I_0 e^{-(t-t_0)/\tau} \quad (27)$$

where, t_0 – time at which PL emission is at peak intensity

I_0 – value of PL peak intensity.

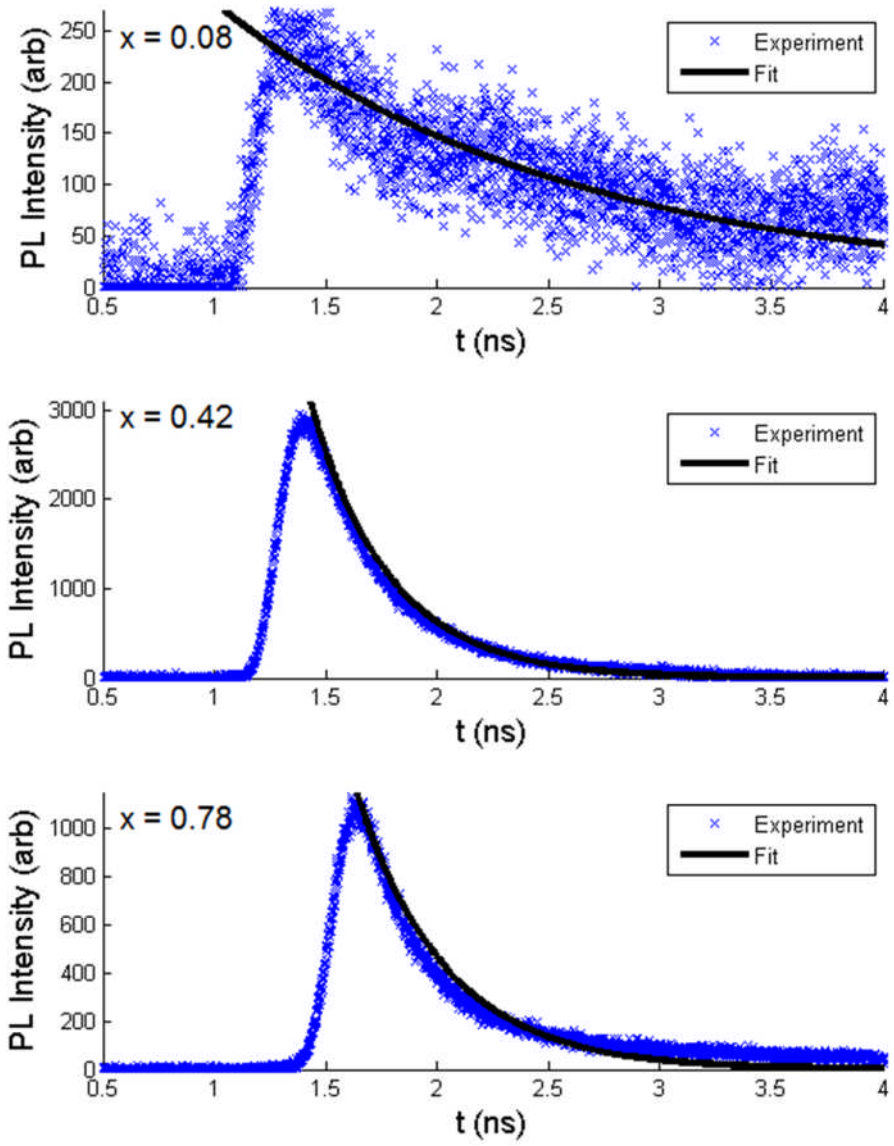

Figure 4.12: Example fits for decay curves from different cubic $Al_xGa_{1-x}N$ alloys at T = 5K using a single exponential fitting function, Equation (27).

Examples of decay curves fitted using this expression are shown in Figure 4.12. Close fits are obtained for samples across the alloy range. In some cases, the decay did not appear to be a single exponential. Fitting with a double exponential function did not lead to significant change in the primary decay constant. The quality of fit for the single exponential function was also found to be high, so the fitting function of Equation (27) was deemed suitable for

general use in identifying trends in the time-resolved behaviour. A comparison between double and single exponential fitting is shown in Figure 4.13.

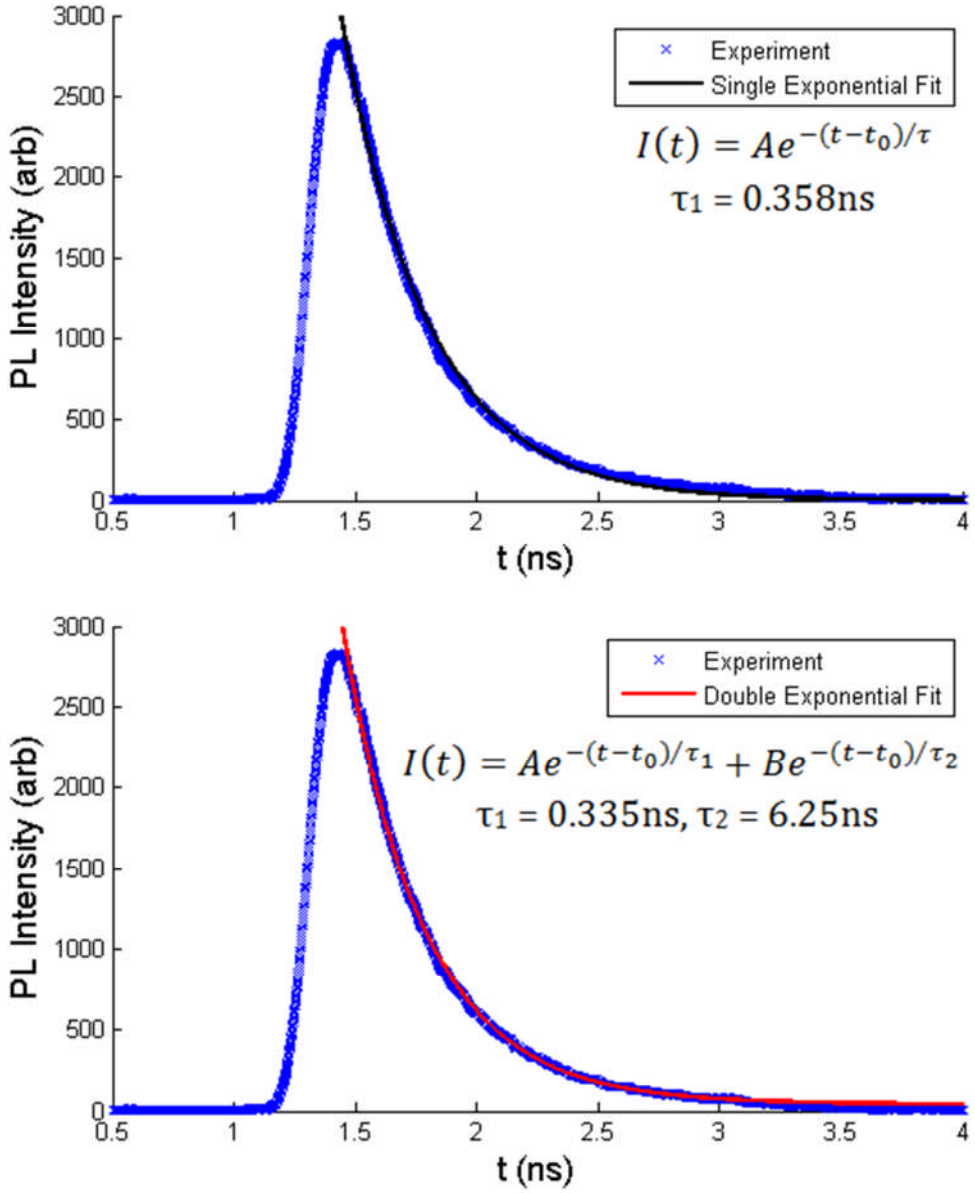

Figure 4.13: A PL decay curve for the cubic $Al_{0.66}Ga_{0.34}N$ alloy at T = 5K with curve fits corresponding to single and double exponential functions.

In time-resolved studies conducted on hexagonal AlGaN alloys, the decay lifetime was found to increase as the AlN molar fraction increased due to the higher carrier and exciton localisation energy [89, 95, 98]. The transition from dominant radiative recombination to dominant non-radiative was also found to occur at a higher temperature in samples with more aluminium as a result of stronger localisation [96].

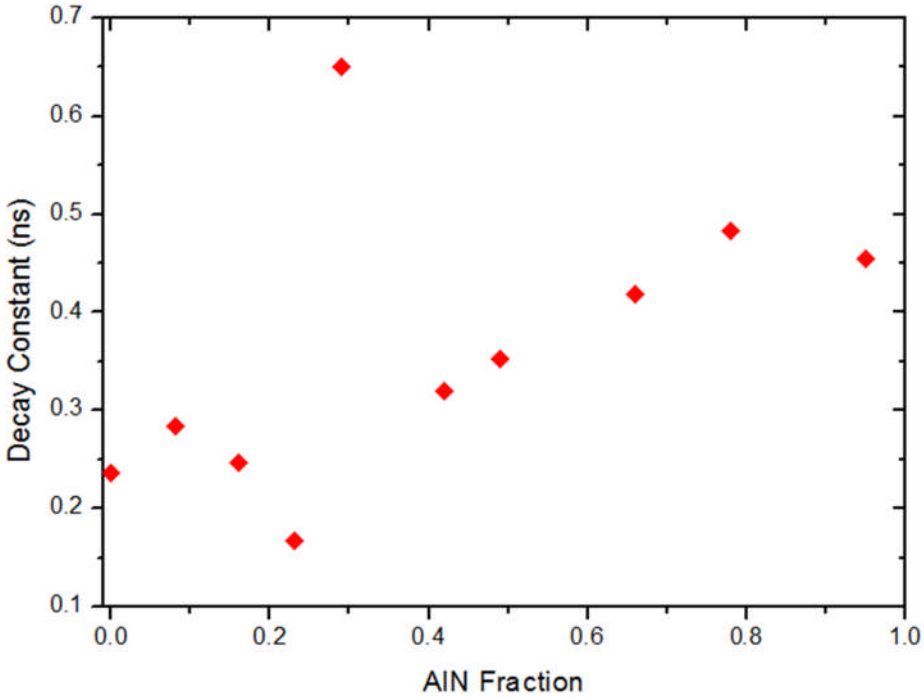

Figure 4.14: Decay constants as a function of alloy composition for cubic $Al_xGa_{1-x}N$ alloys determined at T = 100K.

The variation of the PL decay constant with alloy AlN fraction at a constant temperature is shown in Figure 4.14. The decay time increases steadily as the aluminium incorporation rises, giving further indications that the degree of localisation is greater for higher x. The temperature dependence of the decay time gives a more informative picture of what the recombination dynamics of different alloys are.

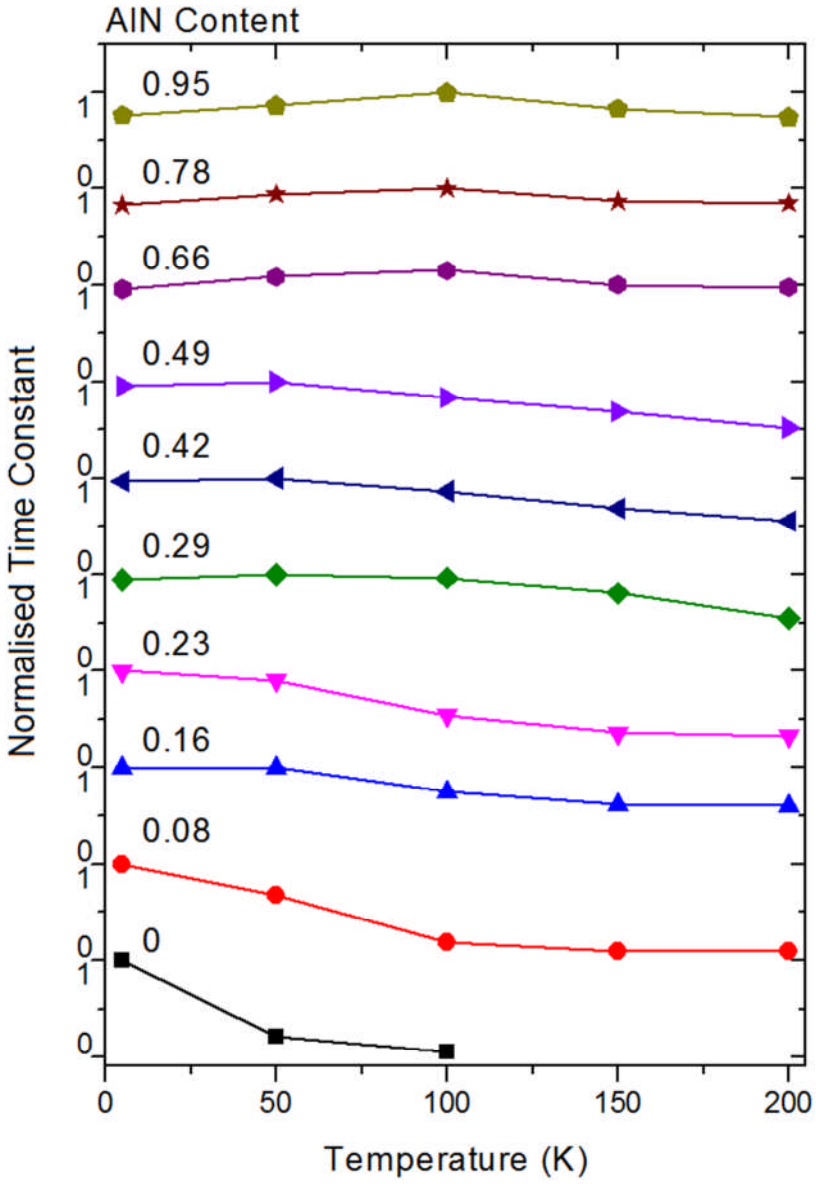

Figure 4.15: Plots of normalised PL decay constant against temperature for the full range of cubic $Al_xGa_{1-x}N$ alloys.

Decay constants as a function of temperature were measured for the different AlN fraction cubic alloys, and the results are shown in Figure 4.15. At the lowest end of the range, including pure GaN, the decay constant starts long and rapidly becomes shorter as the temperature increases. In the mid-range alloys, the decay time decreases slowly with rising temperature. In the high AlN concentration layers, the decay constant fluctuates only slightly across the temperature range, with a relatively low peak at around T ~ 100K.

This change in temperature dependent behaviour is shown more clearly in Figure 4.16, where the decays curves for one high AlN fraction alloy and a low one are shown alongside each

other. In the low AlN concentration sample, the decay has sped up almost to the response limit at the highest temperature, whilst at the higher concentration the curves are very close to each other across the whole temperature range.

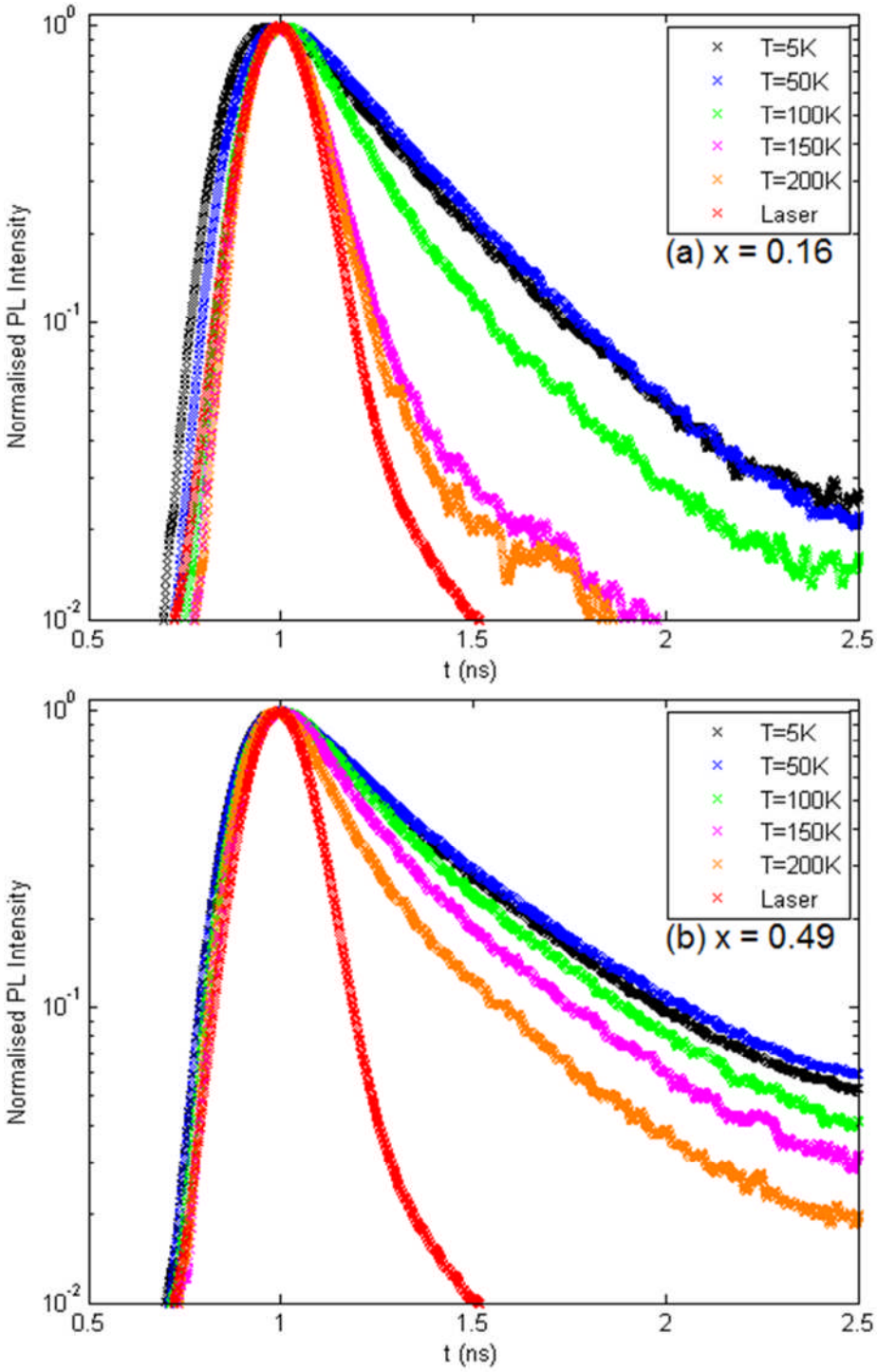

Figure 4.16: PL decay curves taken at various temperatures for cubic $Al_xGa_{1-x}N$ layers with (a) x = 0.16 and (b) x = 0.49.

These results suggest a greater degree of localisation at the higher AlN concentrations. Additional thermal energy is required to release carriers trapped at more spatially separated and deeper sites in the more localised alloys. This causes the onset of non-radiative dominance, manifested as a shorter decay time, to occur at a higher temperature. The effect is seen across the whole range of AlN levels, rather than just up to the upper-middle of the range, again suggesting that NCIs related to nominal alloy fraction are not the only localisation contributor.

The previous results were all recorded at the photon energy of the maximum of the donor-acceptor peak. We have also studied the effect of the emission energy on the decay lifetime by measuring time-resolved dynamics at energies on the wings of the PL peak. An example of this is illustrated in Figure 4.17.

The results for high AlN fraction alloys show that the decay becomes longer as the emission energy decreases. The lower energy emission is from carriers that are more strongly localised in deeper fluctuations or defects at the extremities of the band tails. Their spatial separation results in reduced overlap for radiative recombination, which combines with their inability to reach non-radiative recombination centres to increase emission decay time.

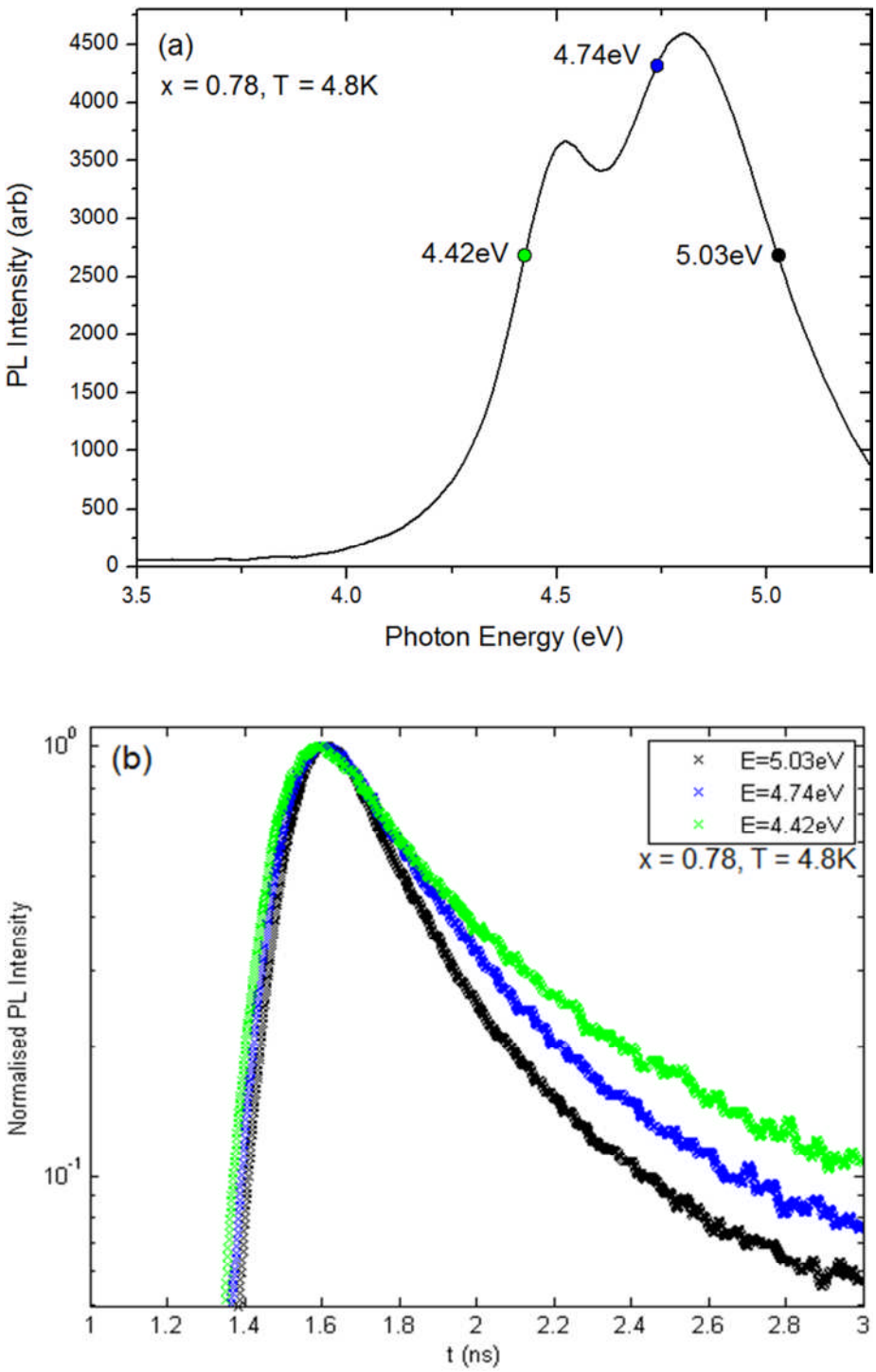

Figure 4.17: (a) Decay curves for the cubic $Al_{0.78}Ga_{0.22}N$ alloy were taken for different emission energies indicated on the PL spectrum. (b) The decay curves taken at the indicated energies.

This effect has been observed in studies performed on localised hexagonal AlGaN [99]. The longer decay time for lower energy emission has also been observed alongside a slower rise time attributed to carriers being generated in the wide band gap matrix and transferring to the localised states for radiative recombination [100].

4.1.4 Reflectivity Measurement

Reflectivity measurements were carried out on the cubic $Al_xGa_{1-x}N$ films in order to provide additional information that could not be discerned from the PL. Reflectivity allows the bandgap energies to be directly measured. It can also uncover evidence of a transition from direct bandgap to indirect bandgap structure in the range of aluminium contents.

Reflectivity spectra were recorded for the full set of alloys using the method discussed in Section 3.3. The spectra describe the proportion of light that is reflected across the range of photon energies and are shown in Figure 4.18.

Below certain photon energies the reflectivity oscillates. The light that entered the measurement apparatus was the result of interference between light reflected from the surface of the sample and light reflected from the internal substrate interface. For each wavelength, the optical path difference between these two light paths changes, resulting in a particular degree of constructive or destructive interference contributing to the reflectivity. The peaks become wider towards the higher wavelengths as small changes in wavelength result in a smaller relative change in phase between the two waves.

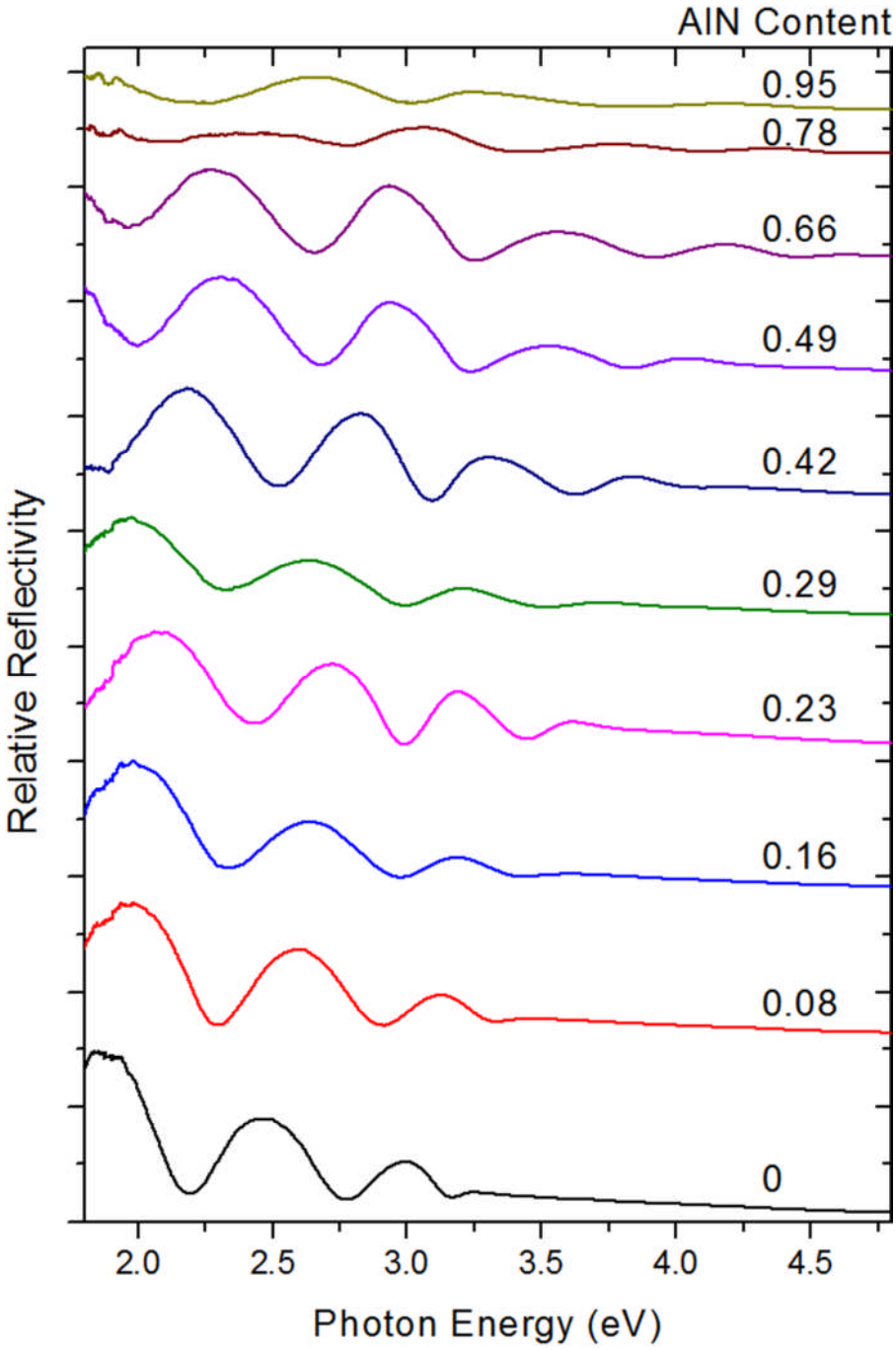

Figure 4.18: Reflectivity spectra for cubic $Al_xGa_{1-x}N$ alloys showing the relative proportion of incident light reflected as a function of photon energy.

Above particular energies the oscillations stop. It is evident from the plot that this energy increases steadily with the AlN molar fraction. This cut-off marks the point at which incident photons possess energies greater than the bandgap and so are always absorbed. The energy at which the fringes end is hence equal to the effective bandgap energy [98]. By fitting an appropriate expression to the data we can obtain a value for the sample's energy bandgap, which could not be determined from the PL spectra.

4.1.5 Fitting Model for Reflectivity Data

In order to determine the bandgap more accurately and extract other useful parameters such as refractive indices, we attempted to create a model for reflectivity that could be fitted to the data. The geometry of the model is shown in figure 4.19. The incident beam, $\mathbf{i_n}$ is partially reflected from the AlGaN surface with reflectance $\mathbf{r_1}$ and continues to propagate through the AlGaN before being reflected from the AlGaN/GaAs interface with reflectance $\mathbf{r_2}$. The overall reflectivity is obtained using methods of wave optics and interference as described in Hecht [101].

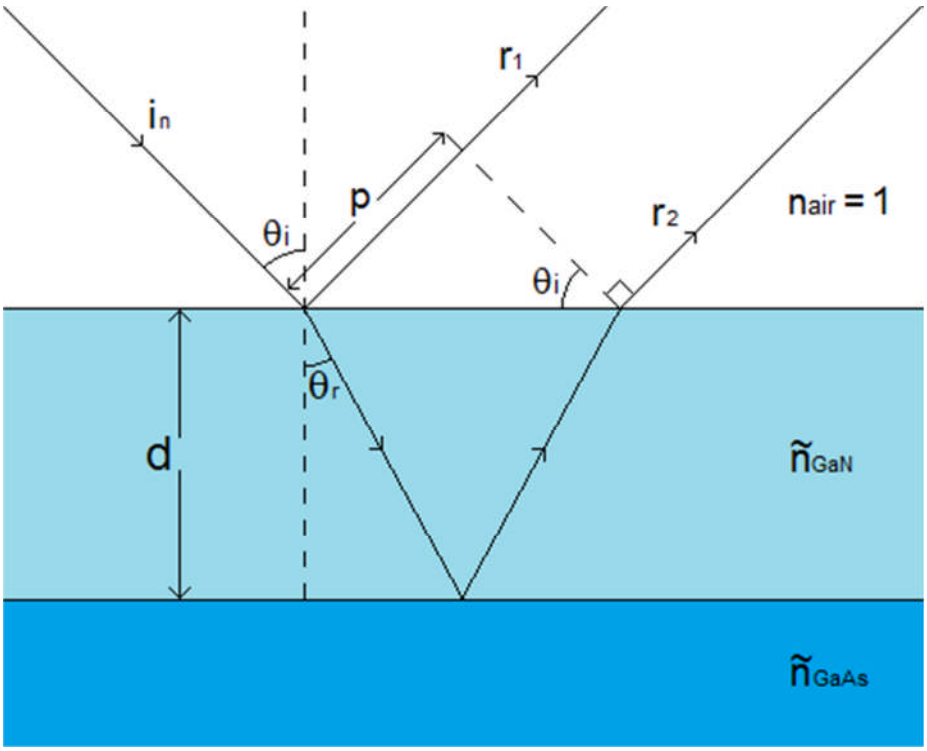

Figure 4.19: Diagram showing geometry of reflectivity model. The model considers the interference between the wave reflected from the sample surface (r_1) and the wave reflected from the AlGaN/GaAs interface (r_2).

The reflectivity of light from the surface is given by a combination of the two reflectances:

$$R = |r_1 + r_2|^2 \tag{28}$$

Using the Fresnel equations, and assuming normal incidence, this becomes:

$$R = \left|\left(\frac{1-\check{n}_{GaN}}{1+\check{n}_{GaN}}\right)+\left(\frac{\check{n}_{GaN}-\check{n}_{GaAs}}{\check{n}_{GaN}+\check{n}_{GaAs}}\right)e^{\frac{2i\pi d\check{n}_{GaN}}{\lambda}}\right|^2 \quad (29)$$

where, $\check{n}_{GaN} = n_{GaN} + i\kappa_{GaN}$ – the complex refractive index of AlGaN material

$\check{n}_{GaAs} = n_{GaAs} + i\kappa_{GaAs}$ – the complex refractive index of the GaAs substrate

λ – light wavelength.

The exponential term in Equation (29) represents the attenuation and phase of the ray reflected from the AlGaN/GaAs interface. The wavelength dependent refractive index components of GaAs used in the calculation were taken from a database [102].

The imaginary component of the refractive index, κ is related to the absorption coefficient, α via:

$$\alpha = 4\pi\kappa/\lambda \quad (30)$$

For direct gap semiconductors, the absorption coefficient is defined by an abrupt cut-off at the energy bandgap [50]:

$$\alpha = A(h\nu - E_G)^{1/2} \quad (31)$$

where, A – a constant

ν – photon frequency.

In order to avoid a singularity in the fitted curve caused by this function's rapid fall off to zero at the bandgap, it was given an exponential tail in the bandgap region of the form:

$$\alpha = Be^{C(h\nu - E_G)} \quad (32)$$

where, B and C – constants.

The values and derivatives of these two functions were matched at their meeting point to prevent any discontinuities. The addition of this tail was justified due to the presence of

impurities and defects that lead to band tails in the energy gap of the material, causing deviations from the function described in Equation (31).

The real refractive index of the AlGaN was modelled using the Cauchy formula [101]:

$$n_{GaN} = D + \frac{F}{\lambda^2} \tag{33}$$

where, D and F – constants.

Up until this point, the model has assumed normal incidence for the light rays onto the surface. In the experiment however, a 45° angle of incidence was used. This means that the path difference, **p** between the two rays is no longer 2d. Accounting for the corrected path difference due to an angle of incidence θ_i leads to the following expression for reflectivity:

$$R = \left| \left(\frac{1 - \check{n}_{GaN}}{1 + \check{n}_{GaN}} \right) + \left(\frac{\check{n}_{GaN} - \check{n}_{GaAs}}{\check{n}_{GaN} + \check{n}_{GaAs}} \right) e^{\frac{2i\pi}{\lambda} \times \left(\frac{2d}{\sqrt{\check{n}_{GaN}^2 - sin^2(\theta_i)}} (\check{n}_{GaN}^2 - \check{n}_{GaN}^2 sin^2(\theta_i)) \right)} \right|^2 \tag{34}$$

Equation (34) was used with Equations (31)-(33) by a MATLAB program to generate a curve that was matched to the experimental data by adjusting the parameters and constants. This function allowed a good match to be achieved between the fit and the data for the absorption edge and the widths of the interference peaks, but there was significant disagreement between the peak amplitudes.

In order to rectify this, the model was expanded to include the effect of Rayleigh scattering of incident light off the material surface. Different wavelengths are scattered by different amounts due to the interaction of their oscillating electric field with the atomic electrons. The incident light and hence total reflectivity was considered to be attenuated by a wavelength dependent factor [86]:

$$R_F = R e^{-G/\lambda^4} \tag{35}$$

where, R_F – overall reflectivity (function used for fitting data)

G – constant.

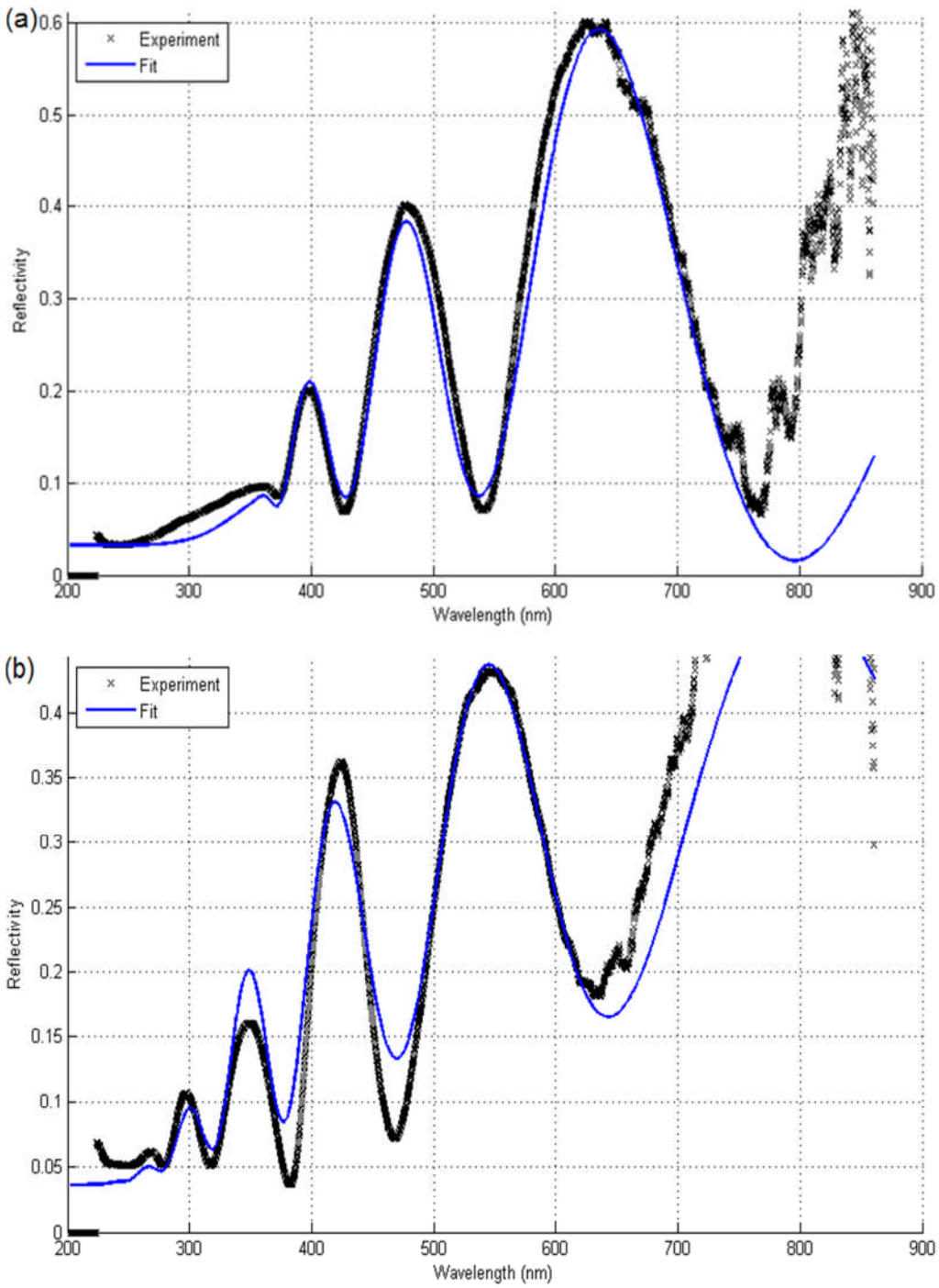

Figure 4.20: Reflectivity spectra for cubic $Al_xGa_{1-x}N$ alloys with (a) x = 0.08 and (b) x = 0.66 shown with the fitted curves from Equation (3).

The fitting parameters used by the program were the bandgap energy, E_G, an energy point at which the values and derivatives of the absorption function and the exponential tail were matched (E_b), the Cauchy constants D and F, the Rayleigh scattering constant G and an overall scaling factor S. The constant A was set to 0.01 in all cases from which B and C were

calculated such that the matching conditions were met for the absorption functions. The extinction coefficient κ was a wavelength dependent factor that depended on the bandgap energy and absorption function matching point for each alloy.

Example fits of the data for two of the alloys is shown in Figure 4.20. There is good agreement between the amplitudes and widths of the peaks as well as the cut-off point for the oscillations. The discrepancies occur towards the edges of the measurement region where the spectrometer does not give reliable readings.

Similar fits were performed on all the other wafers in the set. The bandgap energy values for the samples were extracted from the fits. These values have been plotted alongside the energies of the PL spectrum donor-acceptor peaks in Figure 4.21.

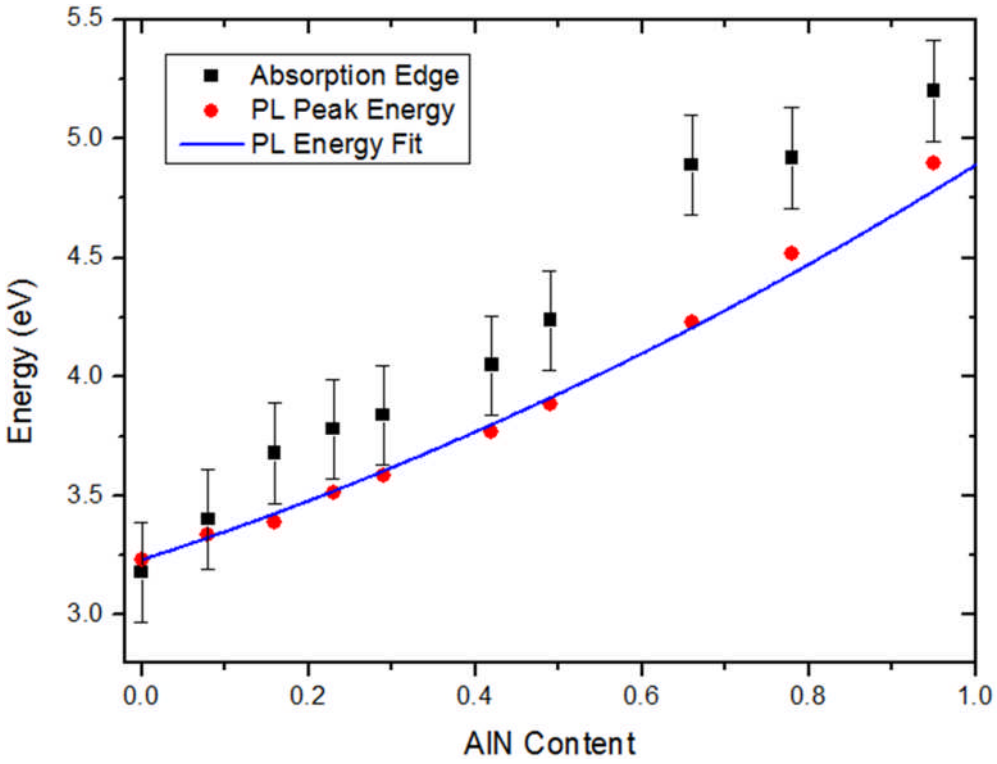

Figure 4.21: Plot of bandgap energies calculated from reflectivity absorption edge (black) against AlN concentration for cubic $Al_xGa_{1-x}N$ films. The energies of the near band edge peaks from PL are also shown (blue) and fitted to Vegard's law.

The bandgap energies from the reflectivity measurements are mostly higher than the PL peak energies, as expected. The bowing of the energy described by Vegard's law is evident from the PL. The same bowing behaviour does not occur in the absorption edge unless the x = 0.66

point is excluded. It is evident from Figure 4.20 that the quality of the fit is not as high for this data point.

An alternative interpretation of the data is that there is a change in behaviour at this point. An indirect valley for the high x alloys would possess highly localised states as shown by the PL studies. Such states would have a very broad momentum spread and could potentially extend into the direct valley permitting PL transitions between that appeared direct in nature. This could explain the disparity in PL and absorption edge variations in Figure 4.21 but relies on the positioning of one data point. Additional data points in the mid to upper x range would be necessary to draw such conclusions.

Other optical studies of cubic AlGaN performed using reflectivity or spectroscopic ellipsometry indicate that the bandgap energy of cubic GaN is around 3.2eV [13, 42, 61] whilst for cubic AlN values range between 4.28eV [103] and 6.1eV [42]. We found reasonable agreement between these bandgap energies and the ones measured from our wafers.

Fitting Vegard's law to our PL peak energies led to a calculated bowing parameter of 0.53eV. Values of bowing parameters from other studies are shown in Table 4.2, indicating that our value is an underestimate.

Source	Bowing parameter (eV)
Suzuki et al. [13]	1.1
Martinez-Guerrero et al. [42]	1.4
Li et al. [103]	1.11

Table 4.2: This table shows values of the bowing parameter of cubic AlGaN determined by various groups.

There is a lack of agreement amongst the literature as to whether cubic AlGaN is a direct gap semiconductor throughout the whole range of AlN content or whether it transitions to indirect gap at higher fraction. Kanoun et al. [57] theoretically calculated a transition at x ~ 0.62. Ellipsometry results produced by Röppischer et al. [58] suggested indirect absorption for cubic AlN. On the other hand, Martinez-Guerrero et al. [42] and Okumura et al. [61] did not

see any experimental evidence of a transition to indirect gap behaviour in their optical studies.

Our own reflectivity measurements showed a near linear relationship between absorption edge energy and the AlN composition, but the outlying position of the x == 0.66 data point raises the possibility of some kind of behaviour change. Our fitting model based on the absorption coefficient profile of a direct bandgap semiconductor was able to achieve decent agreement with the data throughout the AlN content range.

Our results give little indication of a transition to indirect gap but the possibility has been raised due to the highly localised nature of the high AlN content alloys. Further studies, including measurements on a broader range of alloys in the region of interest are warranted.

4.1.6 Conclusions for Bulk Cubic $Al_xGa_{1-x}N$ Layers

Through the use of temperature dependent PL, both time-integrated and time-resolved, we have shown how localisation plays an increasing role in bulk cubic $Al_xGa_{1-x}N$ layers as the AlN concentration is increased. The localisation continues to increase beyond the near mid-range point at which the effect of nanoscale composition inhomogeneities would be maximised.

Other defects or impurities relating to high concentrations of aluminium are therefore likely to be acting as localisation sites as well. These could possibly be hexagonal alloy clusters that contribute relatively weakly to PL but that could potentially be identified by x-ray diffraction measurements. There may be significant alloy fluctuations even at high nominal AlN concentrations as a result of the growth method. The excess gallium that stabilises on the growth surface likely has significant thickness variations that may affect the local incorporation of alloy constituents into the grown film [104]. The localisation is useful as it enhances PL emission efficiency at room temperature.

Our study of the reflectivity of cubic $Al_xGa_{1-x}N$ wafers has allowed their energy bandgaps to be measured. These results, along with others did not show any obvious sign of a transition from direct to indirect bandgap at high AlN molar fraction as expected from theoretical studies, but such a transition could still be consistent with the results.

4.2 Study of Cubic $Al_xGa_{1-x}N$/GaN/ $Al_xGa_{1-x}N$ Quantum Wells

After the optical properties of bulk cubic $Al_xGa_{1-x}N$ were studied, a similar series of measurements was performed on cubic single quantum well (QW) structures. The QW samples were grown using the basic method outlined in the previous chapter (section 3.1). The growth temperature in this case was ~700°C. The full layer structure is shown in Figure 4.22. The region of interest consists of a 2nm wide pure GaN well sandwiched between two 10nm wide barriers of $Al_xGa_{1-x}N$ with AlN fractions between 0% and 90%.

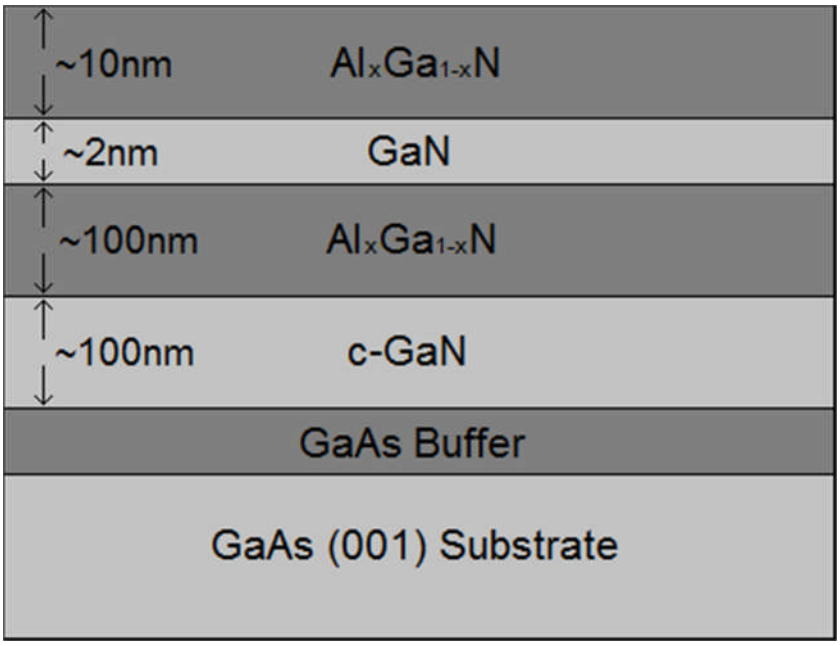

Figure 4.22: Layer structure for cubic $Al_xGa_{1-x}N$/GaN/ $Al_xGa_{1-x}N$ quantum well samples studied.

The specifications of the samples are shown in Table 4.3. The estimated AlN fractions of the barriers were derived from the PL spectra (shown later) by comparing the emission energies to those from the bulk cubic AlGaN layers. The disparity between nominal and measured values may be due to the assumption of equivalence between the two systems that does not take into account differences between the sample sets such as the heterostructure design and different growth conditions.

Sample	Nominal barrier AlN fraction (x)	Al effusion cell flux ($\times 10^{-8}$ Torr)	Estimated barrier AlN fraction (x)
SN-645	0	0	
SN-647	0.3	3.0	0.16
SN-646	0.5	5.0	0.5
SN-649	0.7	7.2	
SN-648	0.9	8.8	

Table 4.3: Sample specifications for cubic $Al_xGa_{1-x}N$/GaN/ $Al_xGa_{1-x}N$ quantum wells. The barrier AlN fraction was estimated from the PL spectra.

In addition to optical measurements, the QW structures were modelled using computer software in order to calculate the expected emission energy. The dependences of the PL spectra and time-resolved decay on temperature were again studied. In addition, the effect of laser excitation wavelength on the PL spectra was considered.

4.2.1 Modelling of Quantum Well Emission Energy

In Section 2.3.2, it was shown that the emission energy E_{PL} of a quantum well was equal to the bandgap energy added to the energies of the lowest allowed energy states in the well:

$$E_{PL} = E_G + E_{hh1} + E_{e1} \tag{36}$$

where, E_{hh1} – confined state energy for heavy hole valence band

E_{e1} – confined state energy for conduction band.

Since these energies depend on parameters of the well that have been determined in various studies, the emission energy of the QW can be calculated as a comparison to the experimental data. We will consider a layer of GaN of width a, sandwiched between two barriers of AlGaN to form a well. A diagram of the conduction band of this structure is shown in Figure 4.23:

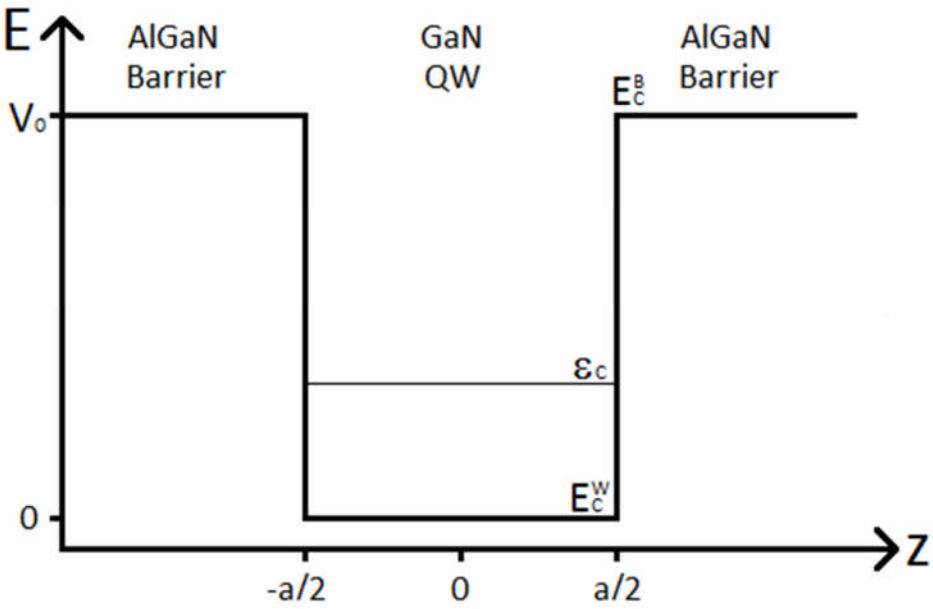

Figure 4.23: Conduction band arrangement used to model the cubic $Al_xGa_{1-x}N$/GaN/ $Al_xGa_{1-x}N$ quantum well and calculate the PL emission energy.

States with energies of less than V_0 are trapped in the well whilst those with greater energies can propagate past it. The wavefunction of a bound state of energy E in the well is given by the solution to the Schrödinger equation in the well [105] (assuming the function is even):

$$\psi(z) = Ccos(kz) \text{ (for } -a/2 < z < a/2) \tag{37}$$

where, C is a constant.

The wavenumber in this case is given by:

$$k = \sqrt{\frac{2m_0 m_w (E - E_C^W)}{\hbar}} \tag{38}$$

where, m_w – effective electron mass in the well

E_c^w- energy conduction band edge in the well.

The wavefunction of the state outside of the well is evaluated to be:

$$\psi(z) = De^{\pm\gamma z} \text{ (for } z < -a/2 \text{ and } z > a/2) \tag{39}$$

where, D is a constant.

The expression for the parameter γ is:

$$\gamma = \sqrt{\frac{2m_0 m_b (E_C^B - E)}{\hbar}} \tag{40}$$

where, m_b – effective electron mass in the barrier

E_c^b – energy of barrier conduction band edge and $E < E_C^B$.

The first step towards obtaining a solvable expression is to apply the boundary condition that the function is continuous across the well-barrier boundary by matching the function values and derivatives at z = ±a/2. Matching function values leads to:

$$\psi(a/2) = Ccos(ka/2) = De^{\pm\gamma a/2}. \tag{41}$$

The matching condition for derivatives takes into account the different effective masses since the derivative equates to the momentum, and conservation of current requires the velocity to be the same on both sides:

$$\frac{1}{m_b}\frac{d\psi_B}{dz}\bigg|_{z=a/2} = \frac{1}{m_w}\frac{d\psi_W}{dz}\bigg|_{z=a/2}. \tag{42}$$

The result of matching using this condition is hence:

$$-Cksin(ka/2) = -D\gamma e^{\pm\gamma a/2}. \tag{43}$$

Equation (43) can be divided by equation (41) to give:

$$\tan(ka/2) = \frac{m_w \gamma}{m_b k}. \tag{44}$$

We can now define the following dimensionless variables:

$$\theta = \frac{ka}{2} \tag{45}$$

$$\theta_0^2 = \frac{m_0 m_w V_0 a^2}{2\hbar^2}. \tag{46}$$

Restating equation (44) in terms of these variables gives us:

$$tan\theta = \sqrt{\frac{m_w}{m_b}\left(\frac{\theta_0^2}{\theta^2} - 1\right)}. \tag{47}$$

Solving this equation numerically gives the value of k for the bound state, which relates to its energy. In order to determine the emission energy of the QW structure (Figure 4.19), the expression was solved separately for the conduction and valence bands, using the appropriate effective masses and well depths, which were decided by the band alignments. The bound state energy of the conduction band is related to the wavevector k via:

$$E_c = \frac{k_c^2 \hbar^2}{2m_0 m_{we}} \tag{48}$$

where, m_{we} – effective electron mass in the conduction band well.

In addition, the bound state energy of the valence band is:

$$E_v = \frac{k_v^2 \hbar^2}{2m_0 m_{whh}} \tag{49}$$

where, m_{whh} – heavy hole effective mass in the valence band well.

The photon energy of light emission from the well is given by:

$$E_{em} = E_G^W + E_c + E_v \tag{50}$$

A MATLAB program was written to calculate the emission energy of the experimental QW structures by solving Equation (50) for a simulated well. The effective masses, taken from

Pugh [22] were $m_e = 0.11m_o$ and $m_{hh} = 0.8m_o$ for zinc-blende GaN and $m_e = 0.19m_o$ and $m_{hh} = 1.2m_o$ for cubic AlN, with m_o equalling the rest mass of the electron. Linear extrapolation between these extremes was used to generate effective mass values for the $Al_xGa_{1-x}N$ barriers with different AlN fractions.

The standard technique for determining band alignment in heterostrucures is to employ Anderson's rule and align the vacuum levels of neighbouring materials. The disparity in electron affinity and band gap between GaN and AlGaN however results in a stepped structure for the bands rather than clear QWs on both bands for our case if Anderson's rule is used. Instead, the bands were aligned such that the ratio of conduction band depth to valence band depth was 70:30, as used by Teke [106]. The band gap energies used in the calculation came from the reflectivity results presented in Section 4.1.4. The calculated emission energy values are presented alongside the PL results in the next section.

4.2.2 Photoluminescence Spectra

PL emission at low temperature was detected from two of the five samples, those with nominal barrier AlN fractions of 30% and 50%. As with the bulk layers, surface gallium droplets were removed from some samples and their effect on PL was assessed. The dark samples did not emit PL after etching, so absorption of incident light by droplets was ruled out as the cause of the problem. The lack of emission may have been caused by problems during growth, but is unlikely to be solely the result of a malformed quantum well layer as no barrier emission was seen.

The PL spectra taken at a range of temperatures for the two luminescent samples are shown in Figures 4.24 and 4.25. In each case, two separate peaks can be clearly seen. The higher energy peak can be assigned to emission from the AlGaN barriers as we have previously noted that adding aluminium to GaN increases the bandgap energy. The lower energy peak hence results from the QW emission.

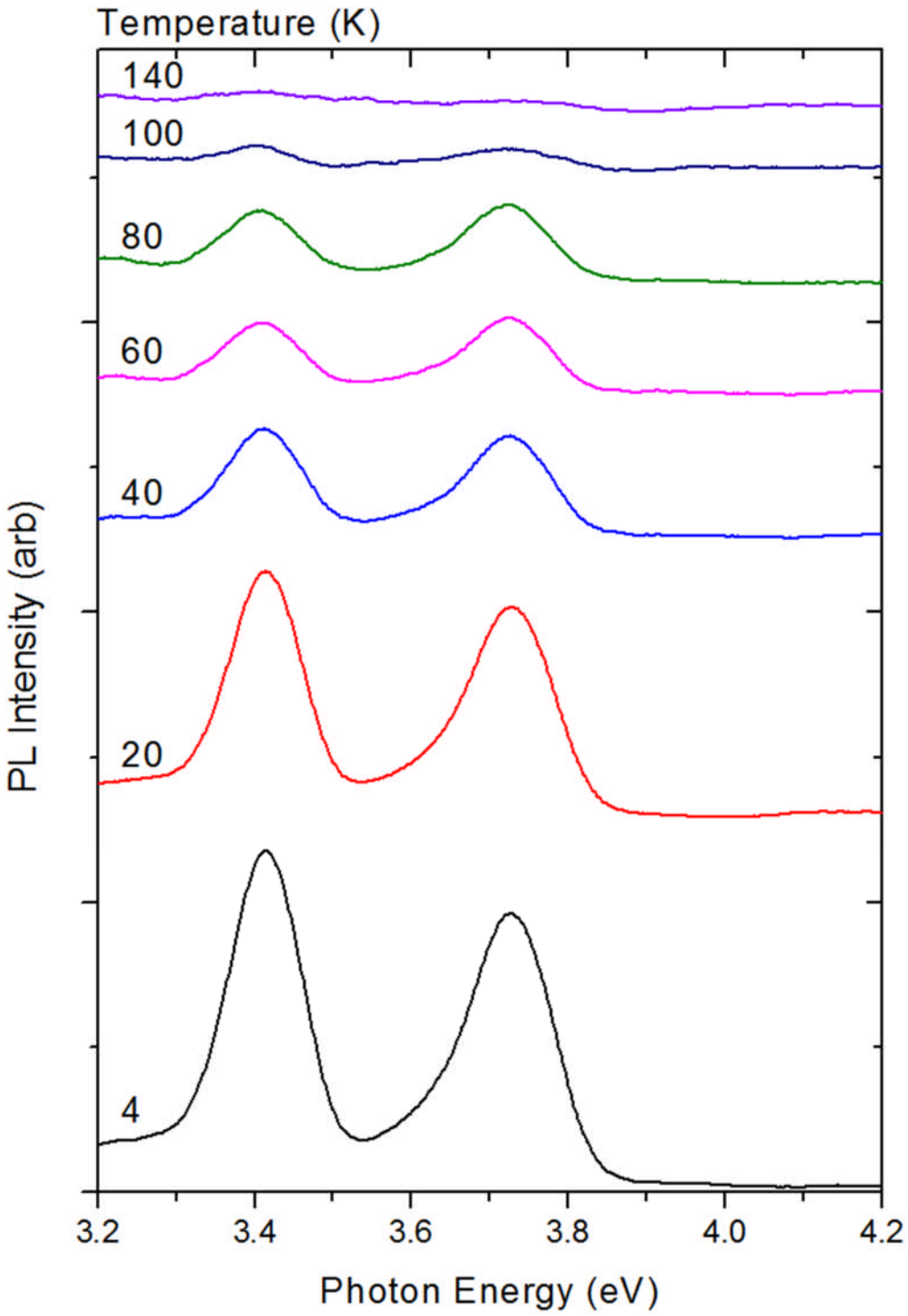

Figure 4.24: PL spectra of the cubic $Al_{0.3}Ga_{0.7}N/GaN/Al_{0.3}Ga_{0.7}N$ QW structure measured at different temperatures.

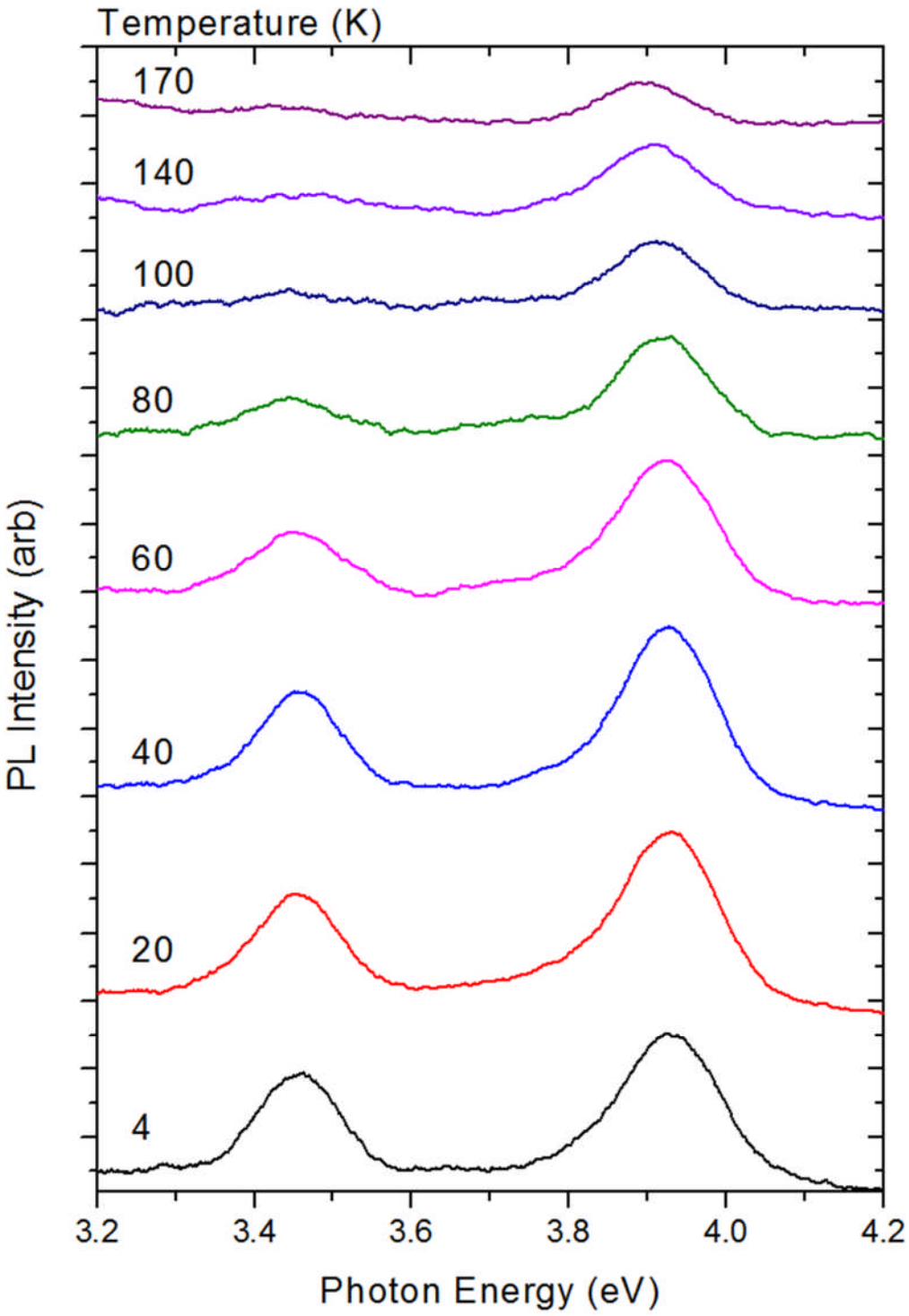

Figure 4.25: PL spectra of the cubic $Al_{0.5}Ga_{0.5}N/GaN/Al_{0.5}Ga_{0.5}N$ QW structure measured at different temperatures.

The barrier PL peak energies recorded were 3.415eV for the 30% nominal AlN fraction and 3.921eV for the nominal 50%. Comparing these energies to those obtained for the bulk AlGaN layers would suggest that the actual AlN fractions were closer to 16% and 50% than 30% and 50%. This comparison is unlikely to be highly accurate due to differences in growth

conditions and strains between the two sample sets, but provides a useful reference in lieu of SIMS data for the QWs.

The PL energy of pure, bulk cubic GaN was previously measured as 3.23eV, whilst the established value for its bandgap is 3.28eV [102]. The QW emission peaks for our samples were at higher energies; 3.415eV for the x = 0.3 sample and 3.462eV for the x = 0.5 sample despite the well containing only pure GaN.

The change in well emission energy from bulk GaN was expected based on Equation (16), which shows that the bound states in the well shift the emission energy higher. The shift is greater in the structure with the higher barrier AlN molar fraction and hence larger band discontinuity. The well emission energies for the two different structures are shown in Table 4.4, alongside the values calculated using the theoretical model:

Nominal barrier AlN fraction (x)	Estimated barrier AlN fraction (x)	Measured emission energy (eV)	Calculated emission energy (eV)
0.3	0.16	3.415	3.387
0.5	0.5	3.462	3.441

Table 4.4: A comparison of measured and calculated well emission energies for cubic $Al_xGa_{1-x}N/GaN/ Al_xGa_{1-x}N$ QW structures.

There is reasonable agreement between the measured and calculated emission energies. The difference in energy between the two AlN concentrations is similar with 0.047eV for the measured values and 0.054eV for the calculated case. There is however a small disparity between the measured and calculated energies at each concentration.

The relative success of the model in predicting the energy shift due to the presence of the QW demonstrates that the QW structure has properly formed and is functioning as expected. The model is based on a well free of electric fields, so its applicability to the results also suggests a lack of internal fields due to hexagonal components. The disparity in values is likely caused by the assumptions of the model, such as the effective mass values, which vary significantly between sources, and the band alignment ratios. Non-uniform well boundaries, compositional fluctuations and impurities can also affect the emission energy.

Schörmann et al. [65] measured the PL of a 3nm single cubic GaN QW with cubic $Al_{0.15}Ga_{0.85}N$ barriers and recorded a well emission peak at 3.3eV, attributed to electron-hole pair recombination in the well. The disparity in emission energies between their QWs and ours is likely due to different growth conditions and their use of a 3C-SiC substrate, which reduced lattice mismatch to cubic GaN and hence reduced strain and dislocation density. In addition, their sample featured a different well width, which directly affects the emission energy.

At low temperature, the intensity of both PL emission peaks was considerably higher in the x = 0.3 structure than in the x = 0.5 structure. Emission from the well was stronger than from the barriers and did not fall off relative to the barrier with increasing temperature in the sample with lower AlN content barriers.

The temperature dependence of the PL emission is discussed by Bacher et al. [107] based on their studies of InGaAs/GaAs QWs. During PL experiments, carriers are generated in the barrier by laser excitation. Many propagate into the QW and become trapped before recombining radiatively, leading to strong emission from the well at low temperature.

As the temperature is increased, carriers are thermally activated and emitted out of the well into the barriers. This causes the population of carriers in the barriers to increase, such that intensity of barrier emission in maintained, whilst the QW emission gets weaker. At higher temperatures, the carriers have sufficient energy to reach sites for non-radiative recombination, leading to an overall decrease in emission from both the barriers and the well.

The fall-off in well emission intensity relative to the barrier in the x = 0.5 structure compared to the x = 0.3 structure is surprising as the greater band offset should lead to a deeper well that should be more difficult for the carriers to escape from. Schörmann et al. [65] noted that barrier emission from their cubic QW structure was suppressed due to efficient collection of carriers into the well from the barrier with 15% AlN. In our work, the higher AlN content in the barrier appears to be introducing other factors that are detrimental to well luminescence.

An alternative interpretation for the stronger barrier emission with the higher AlN content can be provided. A possible mechanism for carrier escape is tunnelling through the interface [108] into barrier band tail states. We have seen in the previous chapter that a broad range of

localisation sites exist in cubic AlGaN, indicative of wide band tails that increase in magnitude at higher AlN concentration. A greater density of band tail states adjacent to the well would therefore permit enhanced tunnelling for higher x barriers. The nitride system features greater band offsets than the arsenide system studied by Bacher et al. [107], so the degree of thermal escape from the wells is likely considerably less in our case. The relative enhancement of the barrier emission at higher temperatures can be explained by considering the thermal dissociation of well excitons whose carriers subsequently tunnel out of the well.

4.2.3 Time-resolved Photoluminescence

Time-resolved measurements were also carried out for the QW structures. The decay curves of PL emission from the barriers and the well were obtained for both luminescent samples. A set of decay curves recorded at T = 4K are shown in Figure 4.26, along with the laser pulse.

The decay curves plotted on a logarithmic scale are linear over roughly one order of magnitude, indicating that the intensity decays exponentially over this range. The decay curves were hence fitted using the single exponential function (Equation (27)) also used to determine the decay constant from the bulk AlGaN wafers.

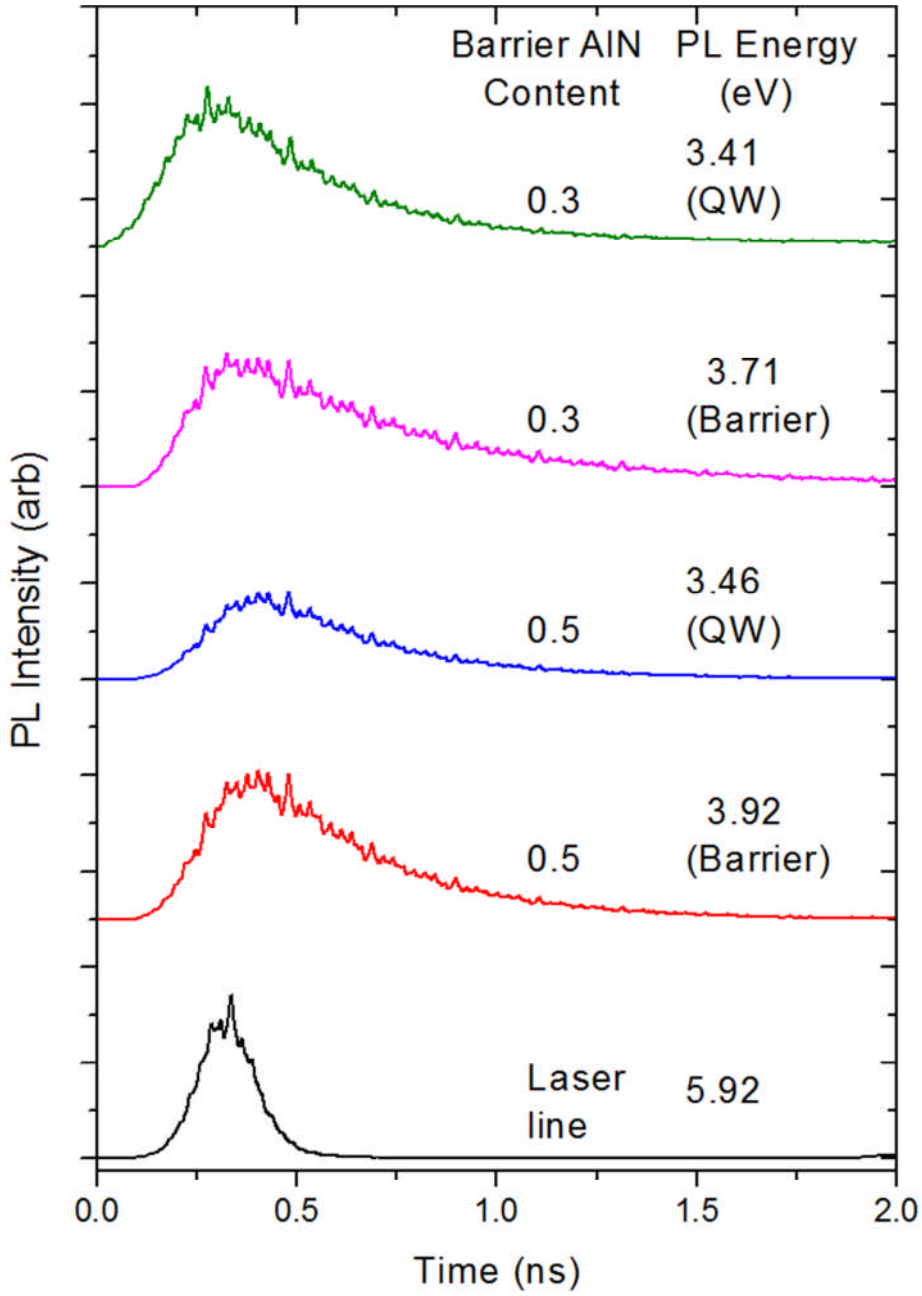

Figure 4.26: Plots of PL intensity against time for cubic $Al_xGa_{1-x}N/GaN/Al_xGa_{1-x}N$ QWs. The decays of both well and barrier emission are shown. Recorded at T = 4K.

The time constants were calculated for decay curves recorded at PL emission energies across the spectrum at constant excitation power at T = 4K. These results are shown in Figure 4.27. The decay time peaks at an energy in between the well and barrier peak emissions.

This variation is similar to what was observed in the time-resolved measurements of the bulk cubic AlGaN films (Figure 4.17). The low energy wing of the barrier peak represents emission from the deeper barrier tail states. The more strongly localised carriers here are

subject to reduced recombination overlap and reduced ability to reach non-radiative centres, leading to a slower decay. As the energy is decreased towards the high energy side of the well peak, the decay time speeds up due to the mobile, non-localised carriers involved in well, rather than barrier recombination. Fluctuations in the well width can lead to localisation effects in addition to alloy fluctuations and the presence of impurities [109].

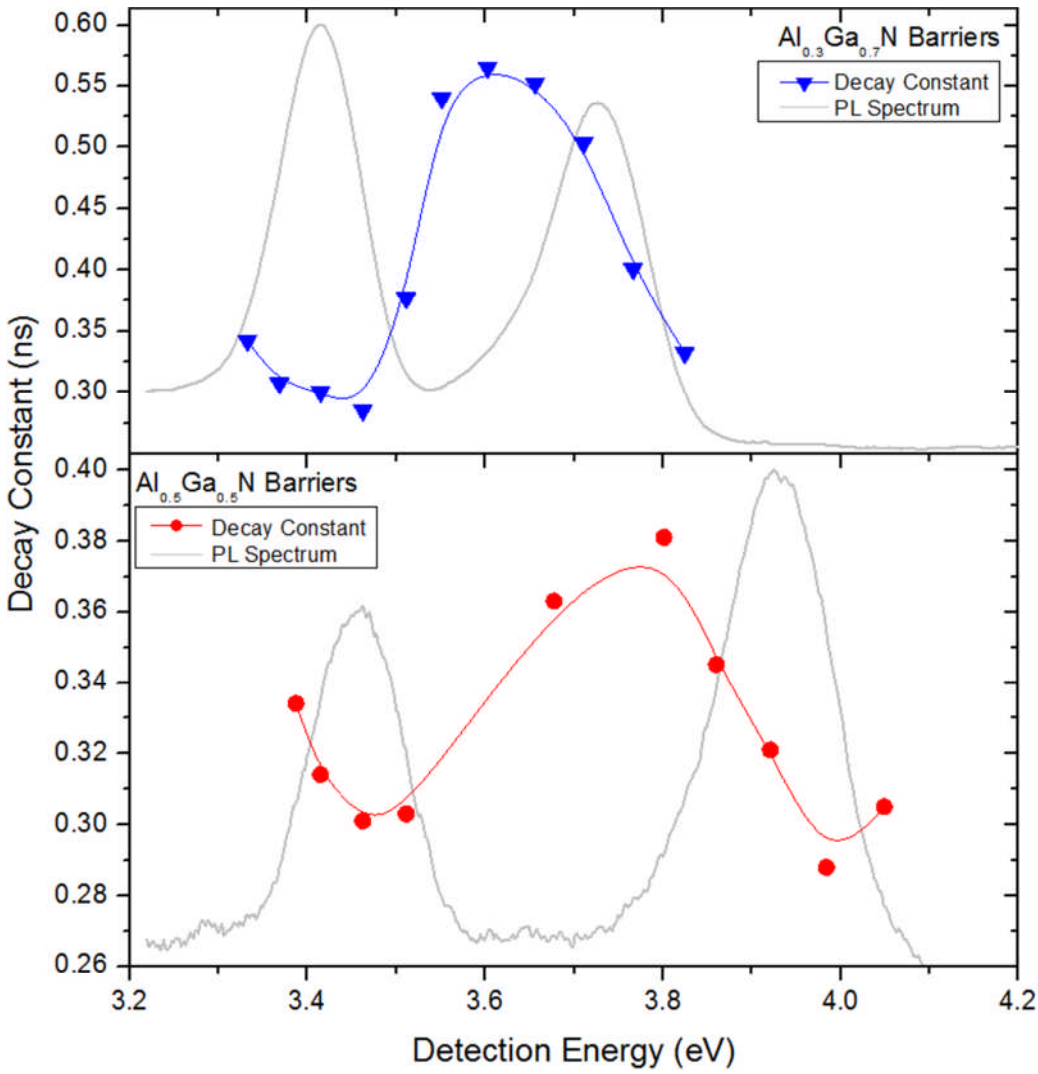

Figure 4.27: Plot of PL decay constant against emission energy for cubic $Al_xGa_{1-x}N$ /GaN/$Al_xGa_{1-x}N$ QW structures. The PL spectrum is shown in the background as a reference.

The decay times for PL were found to be significantly higher in the energy range between that of the well and barrier emission at the lower barrier AlN concentration. This suggests that carriers with energies between the two peaks are less mobile, potentially implying easier

transit between well and barrier with the higher AlN barrier concentration, as shown by the temperature dependent PL.

For each structure, emission from the barrier decays more slowly than from the QW due to the stronger overlap of electron and hole wavefunctions in the well. This suggests that the process of carrier capture into the QW occurs much faster than the recombination process since carriers have to be captured from the barrier before recombining.

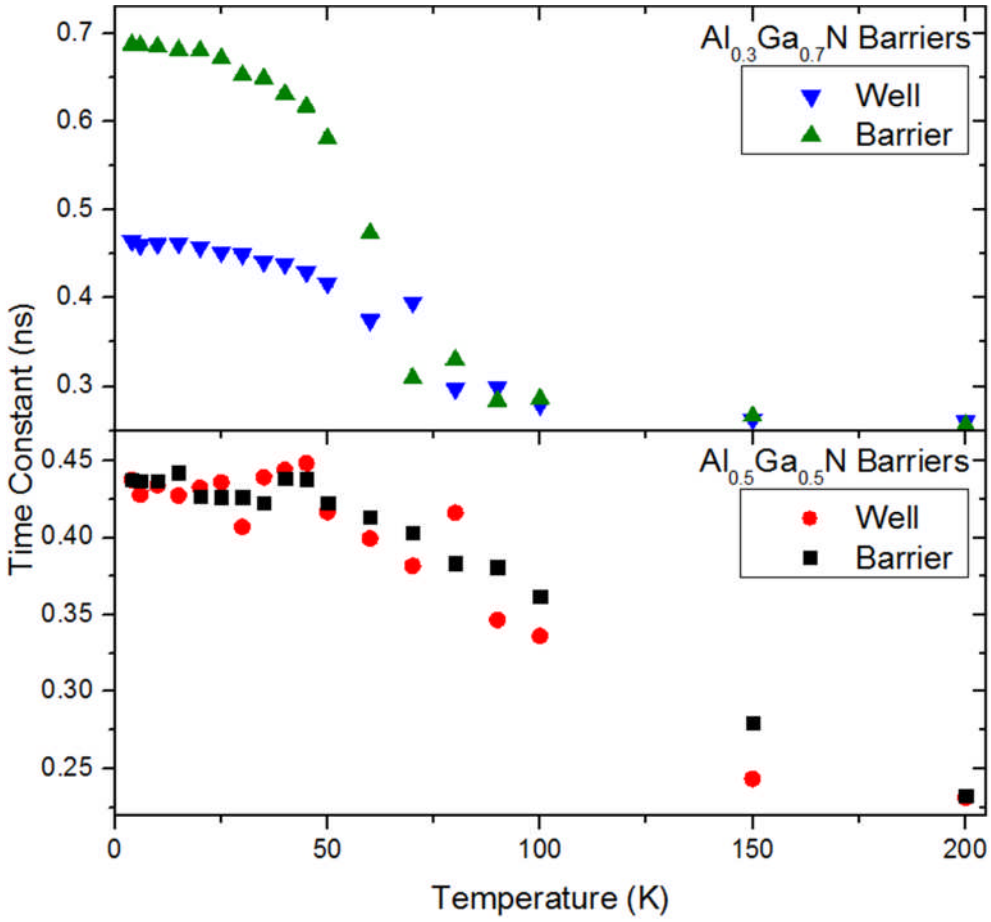

Figure 4.28: Plot of PL decay constant against temperature for well and barrier emission for both cubic $Al_xGa_{1-x}N$/GaN/ $Al_xGa_{1-x}N$ QW structures.

The variation of the decay constant with temperature for well and barrier emission from both samples is shown in Figure 4.28. As the temperature is increased from 4K, the decay time remains relatively constant and then starts to speed up when the temperature passes ~50K. The 30% AlN barrier sample experiences a much sharper decrease in decay time compared to the 50% AlN case. A similar and characteristic variation has been observed in many TRPL

studies of QW structures, where the decay time peaks at a certain temperature. This is related to the lifetimes of radiative and non-radiative recombination.

The temperature-dependent decay time constant can be expressed as a sum of separate lifetimes for radiative and non-radiative recombination channels [110]:

$$\frac{1}{\tau(T)} = \frac{1}{\tau_r(T)} + \frac{1}{\tau_{nr}(T)} \tag{51}$$

where, $\tau_r(T)$ – lifetime for radiative recombination

$\tau_{nr}(T)$ – lifetime for non-radiative recombination.

The radiative efficiency of the semiconductor at temperature T can also be stated in terms of these lifetimes:

$$\eta(T) = \frac{I(T)}{I_0} = \frac{\tau}{\tau_r} \tag{52}$$

where, I(T) – PL intensity at temperature T

I_0 – PL intensity at low temperature.

By combining equations (51) and (52), we can obtain expressions for the radiative and non-radiative lifetimes in terms of quantities that have been measured during this experiment:

$$\tau_r(T) = \frac{I_0 \tau(T)}{I(T)} \tag{53}$$

$$\tau_{nr}(T) = \frac{I_0 \tau(T)}{I_0 - I(T)} \tag{54}$$

These lifetime components were calculated using the decay constants from the TRPL experiment and the intensities of the PL peaks at different temperatures. A plot of the results for well emission is shown in Figure 4.29:

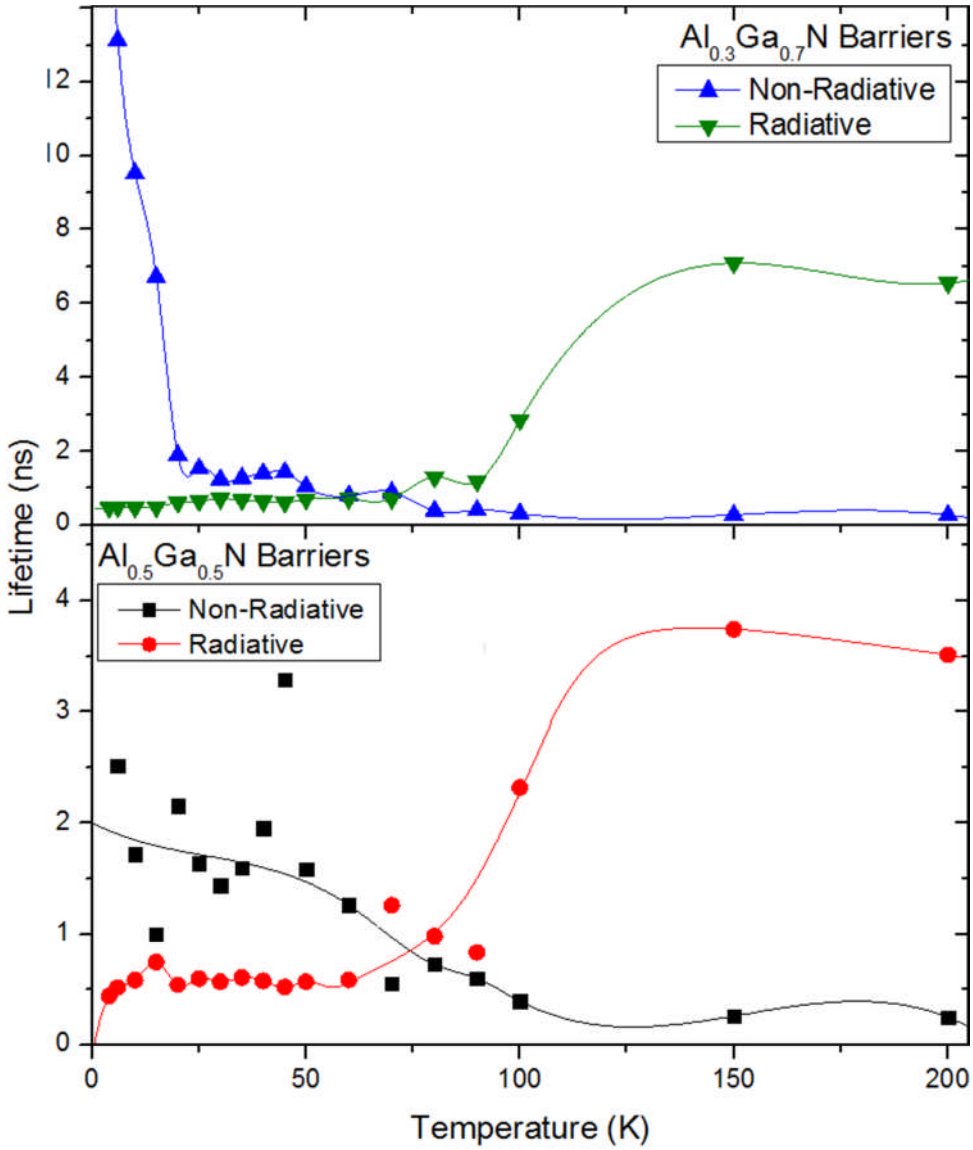

Figure 4.29: Plot of radiative and non-radiative lifetimes for well emission from both cubic $Al_xGa_{1-x}N$/GaN/ $Al_xGa_{1-x}N$ QW structures. The lines are intended as guides for the eye.

The dependence of the lifetimes on temperature is similar in both cases, but more clearly defined for the structure with 30% AlN in the barriers. At temperatures up to about 70K, the radiative process lifetime is shorter and therefore is the dominant recombination mechanism as carriers recombine in the fastest way available.

As the temperature increases, the radiative lifetime starts to increase, likely due to the thermal activation of carriers from localised states and the well, decreasing confinement and recombination overlap. The non-radiative lifetime decreases as the increased mobility of carriers allows them to reach the non-radiative sites likely located at defects. At a certain

temperature, the lifetimes cross over and the non-radiative channel becomes dominant. This leads to the peak in the decay constant and decrease in PL intensity as the temperature is increased.

The variation in overall decay constant observed in this experiment has been observed in single and multiple QW structures formed of hexagonal [109] and non-polar AlGaN/GaN [63] as well as AlGaAs/GaAs [110]. In these studies, an additional initial phase of rising decay time is observed before it peaks. The temperature of the transition from radiative to non-radiative dominance varies in each case but is found to vary strongly with well width.

The phenomenon is explained by Bacher et al. [107] in their study of InGaAs/GaAs QWs. At low temperature, carriers are captured into and become trapped in the QW and recombine radiatively. This leads to a short decay time dominated by the radiative lifetime. As the temperature is increased, excitons are more likely to disassociate, leading to more of the slower recombination between free electrons and holes, which increases the decay time.

When the temperature increases further, more excitons can escape out of the well due to thermal activation. Once free of the well they can travel to traps where they recombine non-radiatively. This decreases the non-radiative lifetime, causing it to become dominant and reduce the overall decay time.

As part of their investigation, Bacher et al. studied a sample featuring additional QWs acting as artificial traps, plus a sample without any confinement layers designed to permit non-radiative surface recombination. The PL emission from both structures experienced a lower temperature onset of decreasing decay time compared to the single QW, highlighting the importance of non-radiative centres in the barrier for structure emission.

Based on this and considering the greater band offset and band tailing in cubic AlGaN, the low temperature onset of decreasing decay time in our cubic QWs was attributed to the tunnelling of carriers out of the well after exciton thermal dissociation and their subsequent non-radiative recombination at surface and interface sites. The role of the interfaces and surfaces must be significant since high AlN fraction bulk cubic AlGaN layers exhibited strong luminescence whilst possessing few interfaces.

The relatively rapid transition with rising temperature in our structures suggests that carriers are able to escape from the wells easily, an effect which appears stronger with more AlN in the barriers. Increasing the well width has been proposed as a means of reducing carrier emission for structures that lacked in-built electric fields.

4.2.4 Excitation Dependent Photoluminescence

Time integrated PL spectra were also taken at low temperature for different excitation laser *powers*. The resulting PL peak energies remained constant at all powers for both samples, whilst the intensity increased linearly as the power was increased.

If there were internal fields present, the increase in the number of carriers created at higher powers would screen out these fields and reduce the separation in electron and hole wavefunctions caused by the QCSE [111]. The resulting increase in emission efficiency would prevent a linear increase of the emission intensity as the power was increased, in addition to a blueshift of the emission peak. Since evidence for the QCSE is not observed, there appears to be a lack of any hexagonal component that would lead to internal fields.

We also conducted a PL excitation (PLE) measurement where the effect of changing the excitation photon energy on the PL emission intensity is studied. This was performed at low temperature and constant excitation power. The integrated area under the time-resolved PL decay curves were plotted against excitation energy as shown in Figure 4.30.

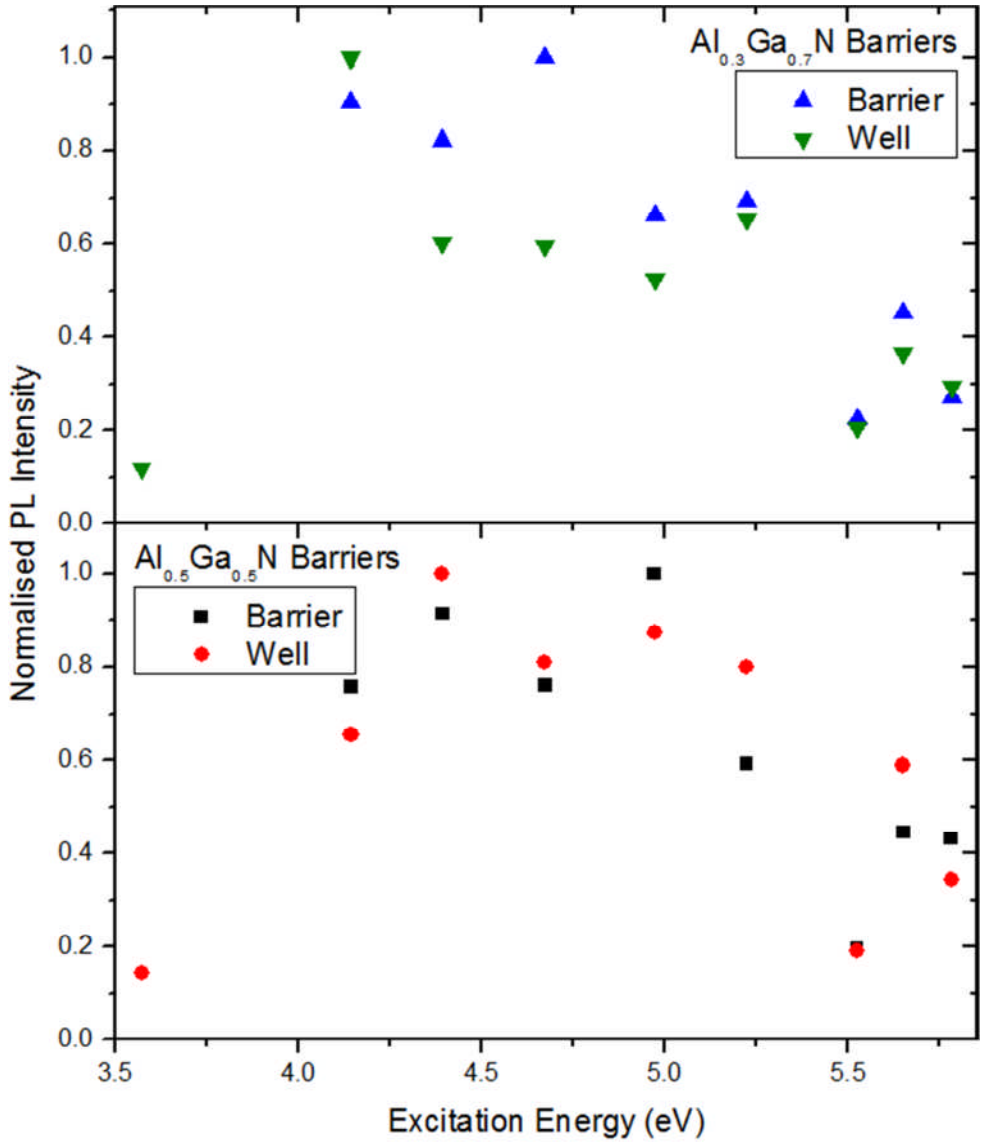

Figure 4.30: Plot of integrated PL peak intensity against excitation energy for cubic $Al_xGa_{1-x}N$/GaN/ $Al_xGa_{1-x}N$ QW structure barrier and well emission.

For both sets of measurements, the PL intensity increased as the excitation energy decreased towards the bandgap. This occurs because carriers excited at energies close to the bandgap spend less time rethermalising before recombination and hence are less likely to encounter a site for non-radaiative recombination.

Near to the band edge, the intensity either flattened off or decreased rapidly, an effect that is more pronounced in the sample with 30% barrier AlN fraction. When the excitation energy is very close to the bandgap, not all of the laser light is absorbed and the emission intensity is therefore reduced. The band edge in 30% barrier AlN structure is likely to be more abrupt due to the alloy being more homogenous.

When the time-resolved PL decay times were measured at different laser excitation powers, it was clear that the power did not have any effect on the decay time. This further supports the suggestion that there is no QCSE from hexagonal structure present as any increase of the wavefunction overlap due to field screening by additional carriers would be expected to cause a decrease in the decay time.

4.2.5 Conclusions for Cubic $Al_xGa_{1-x}N$/GaN/ $Al_xGa_{1-x}N$ Quantum Wells

When the temperature was increased, the decay times for well PL emission started to decrease at an earlier point than QW structures in other studies. In addition, no PL emission was seen from many of the QW structures with different barrier AlN concentrations. These results suggest that defects and impurities, most likely lying at interfaces are acting as strong non-radiative centres in the cubic QW structures. These defects are possibly due to strain around the interfaces.

This assessment is supported by the study of the bulk cubic material grown under similar conditions, which gave stronger PL emission whilst having much fewer interfaces in its structure. The weaker well PL in the 50% barrier aluminium sample and lack of PL from the higher x samples suggests that it becomes easier for carriers to leave the well and combine non-radiatively as the AlN content in the barrier is increased.

We have confirmed using excitation dependent PL the lack of QCSE and hence of hexagonal material in the QW structure. Our other measurements however show that the quality and confinement potential of the well interfaces may be degrading as more aluminium is put into the barrier. Further studies, including in particular an investigation of the effect of well width on the emission and time-resolved dynamics are warranted.

Chapter 5: Characterisation of Cubic GaN Doped with Silicon or Magnesium

This chapter will discuss the study of a series of cubic GaN films doped with magnesium (Mg) or silicon (Si). The layer thickness and doping levels were varied between samples. We characterised the samples using time-integrated and time-resolved PL. We also studied their electrical properties via transport measurements. Our analysis has focussed in particular on the blue PL emission from the Mg-doped samples, a phenomenon that has been explained in doped hexagonal GaN but whose origin is not well established for the cubic phase.

5.1 Sample Specifications

The samples were grown on a GaAs (001) substrate as described in the experimental chapter (Section 3.1). The growth temperature for these films was 700°C and the growth rate was 0.25μm per hour. The film thicknesses varied considerably between 0.5μm and 11.8μm Doping of GaN was facilitated using a standard effusion cell for Mg and a high temperature effusion cell for Si.

Sample	Thickness (μm)	Magnesium Cell Temperature (°C)	Magnesium Dopant Concentration (cm^{-3})
SN-709	0.572	Not doped	0
SN-710	0.573	195	5×10^{17}
SN-711	0.551	230	-
SN-712	0.550	230	9×10^{18}
SN-713	5.664	250	2×10^{19}

Table 5.1: This table shows the sample specifications for the Mg-doped cubic GaN wafers. The Mg concentration was determined from SIMS measurements.

Sample	Thickness (μm)	Silicon Cell Temperature (°C)	Silicon Dopant Concentration (cm^{-3})
SN-714	0.550	Not doped	0
SN-715	0.550	1100	5×10^{17}
SN-716	0.550	1000	-
SN-717	0.550	1150	1×10^{18}
SN-718	0.550	1000	-
SN-719	0.550	1125	-
SN-720	11.8	1150	9×10^{17}
SN-721	6.6	1150	1×10^{18}

Table 5.2: This table shows the sample specifications for the Si-doped cubic GaN wafers. The Si concentration was determined from SIMS measurements.

The temperature of the dopant effusion cell used during growth does not give an accurate measure of how much has been incorporated into the layer. Secondary ion mass spectroscopy (SIMS) measurements were hence performed (externally at Loughborough Surface Analysis Ltd.) on the doped GaN layers to measure the incorporated dopant concentrations. The sample specifications are shown in Tables 5.1 and 5.2.

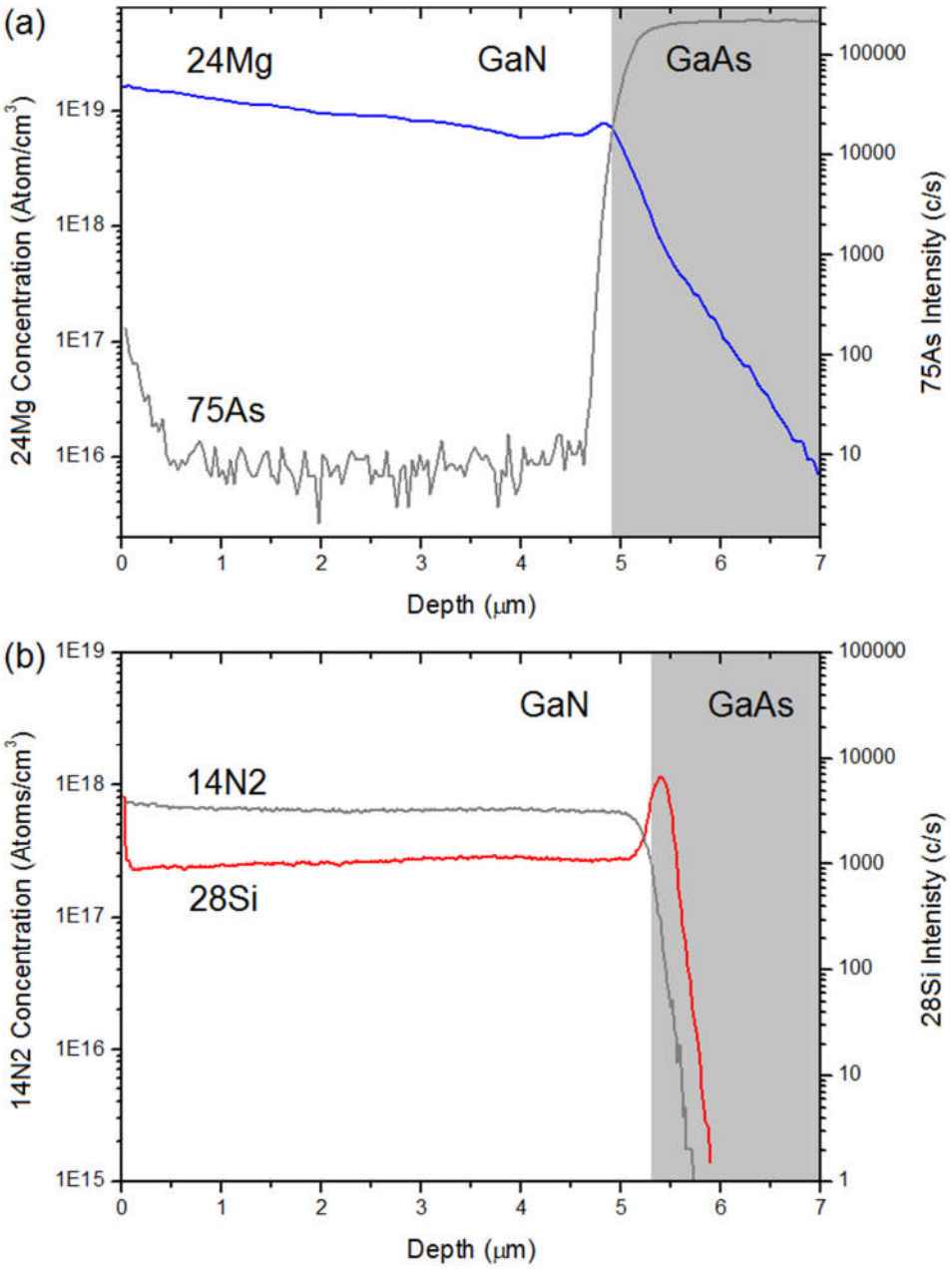

Figure 5.1: SIMS depth profiles showing concentrations of main atomic types in (a) Mg-doped and (b) Si-doped cubic GaN layers.

SIMS depth profiles for each type of doped layer are shown in Figure 5.1. These show the concentration of certain atomic types as a function of depth within the sample. The interface between the doped GaN layer and the GaAs substrate has been highlighted. It is evident that the dopants have been incorporated uniformly throughout the GaN layer. The spikes in concentration that occur on the upper surface and the internal interface are a result of the

measurement technique, which induces cratering and lateral diffusion as the ion beam digs through the layer.

5.2 Study of Mg-Doped Cubic GaN

Magnesium is used as the main p-type dopant to GaN, introducing acceptor levels above the valence band and contributing additional holes. As in the case of undoped layers, PL was used as the primary characterisation method for both types of doped samples. The temperature dependence of both time-integrated spectra and time-resolved decays was studied. Additionally, the surfaces of many samples were imaged using a scanning electron microscope in order to aid interpretation of PL and electrical measurements. Electrical transport measurements were performed to determine the free carrier density and mobility.

5.2.1 Photoluminescence Spectra of Mg-Doped Cubic GaN

The low temperature time-integrated PL spectra of the Mg-doped cubic GaN layers are shown in Figure 5.1, sorted according to dopant concentration. The intensities of the spectra have been adjusted for visual clarity, but the intensity of the thicker (topmost) layer was found to be significantly higher than the others, likely as a result of the greater bulk of material in which light could be absorbed and generated. The lowest dopant concentration sample generated higher intensity emission than the mid level sample, so no clear correlation between doping level and emission intensity can be deduced from these spectra.

A number of distinct spectral features are evident on the doped samples compared to the undoped control sample. The main features are consistent with those observed in other studies of Mg-doped cubic GaN [55, 112]. As shown on Figure 5.2, we have identified PL peaks corresponding to impurity bound excitonic transitions (X) at 3.25eV, a dominant ‘omnipresent’ near band edge donor-acceptor recombination (D^0-A^0) at 3.15eV, and transitions involving a band edge donor and a shallow Mg acceptor (D^0-A^0_{Mg}) at 3.05eV.

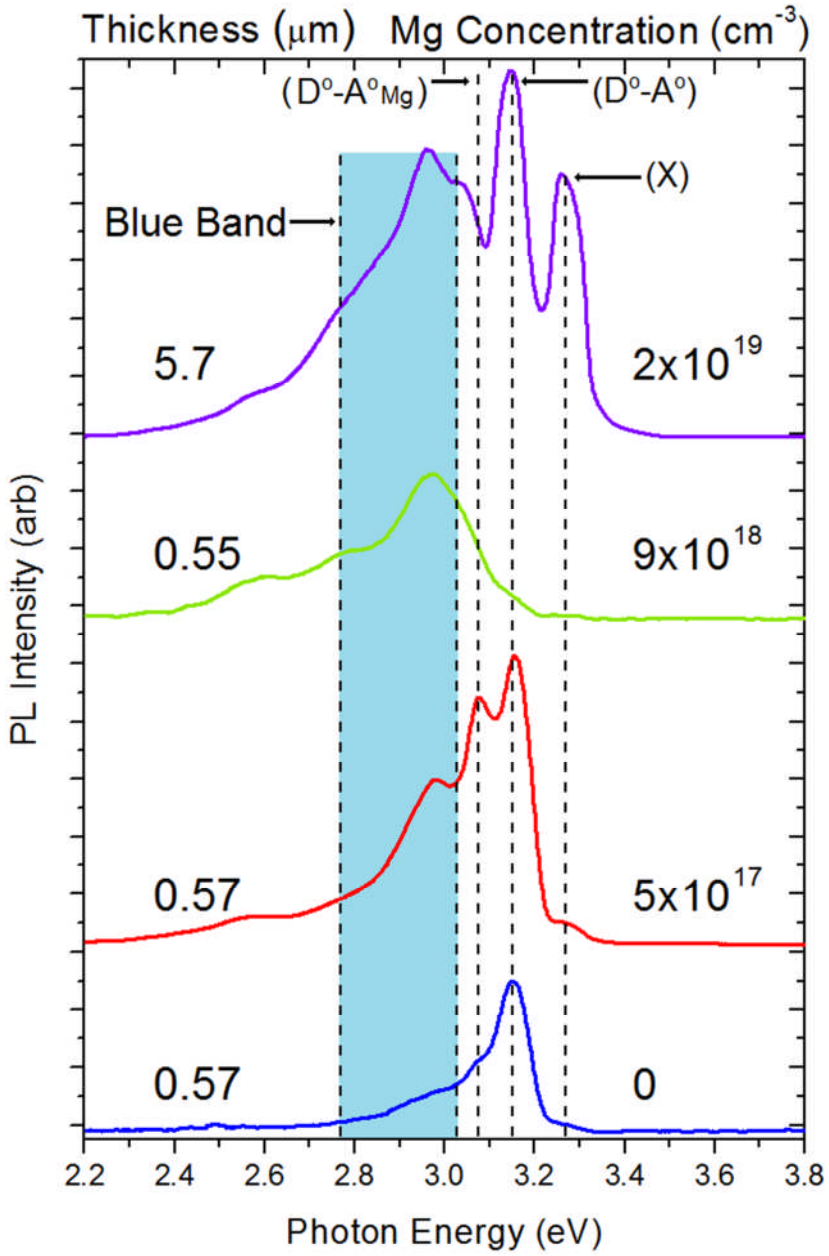

Figure 5.2: PL spectra for Mg-doped cubic GaN wafers recorded at T = 4K. The layer thickness and Mg dopant concentration are indicated in each case.

We also observed a broad 'blue band' of emission peaking at about 2.95eV that became larger relative to the D^0-A^0 peak as the Mg dopant density increased, as observed by Martinez-Guerrero et al. [66]. The undoped GaN sample featured a low energy tail to the main peak, but did not feature the strong blue band peak of the doped samples. The blue band peak has been observed in other studies of cubic GaN but its origin is not fully understood. We have therefore studied the temperature dependence and time evolution of this peak particularly closely in order to learn more about its origin.

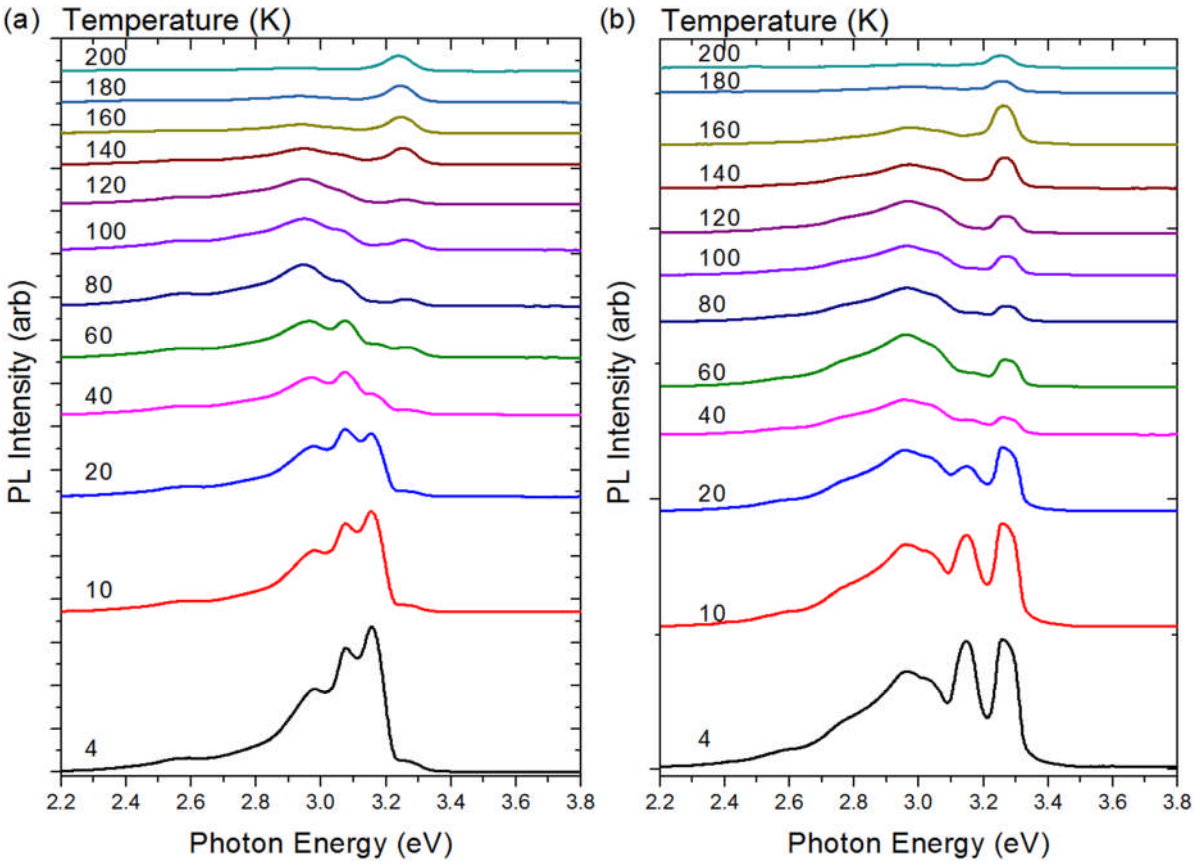

Figure 5.3: Temperature dependent PL spectra for Mg-doped cubic GaN wafers with dopant concentrations of (a) $5\times10^{17}cm^{-3}$ and (b) $2\times10^{19}cm^{-3}$.

When the temperature-dependent spectra were studied for the Mg-doped GaN samples, examples of which are shown in Fig 5.3, the increase in temperature from T = 4K led to reductions in peak intensity for the band tail peaks. This was expected due to the thermalisation of localised states on impurities and fluctuations, which allows carriers to escape to non-radiative centres. It was observed that the D^0-A^0 peak intensity decreased more rapidly than the blue band, as indicated in the intensity plots of Figure 5.4. This indicates that the ionisation energy for the carriers that contribute to the blue band peak is larger.

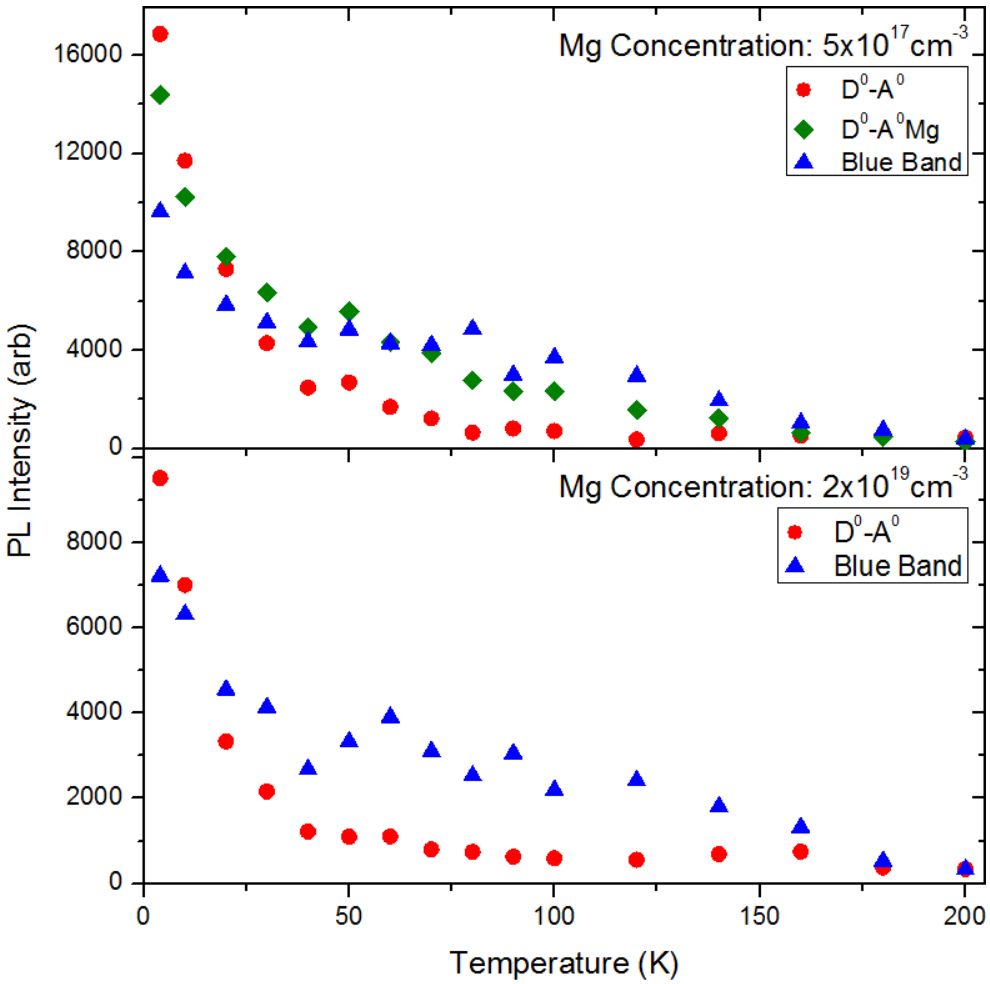

Figure 5.4: Plot of PL emission intensity against temperature for Mg-Doped cubic GaN layers of different dopant concentrations.

The excitonic peak appears to shift downwards in energy whilst its intensity remains relatively stable, allowing it to become the prominent feature of the room temperature spectra at ~3.22eV. The energy shift can be explained by the band gap shrinkage effect regularly observed in temperature dependent PL studies [112].

The lack of temperature quenching is a consequence of the high binding energy of the exciton, which only allows the exciton to dissociate when a large amount of thermal energy is put in at higher temperatures. Using the expression for exciton ionization energy [45] in conjunction with effective mass and optical values taken from a database [102], the nth level ionization energy of the exciton in cubic GaN can be estimated:

$$E(n) = -\frac{\mu}{m_0}\frac{1}{\varepsilon_r^2}\frac{R_H}{n^2} \quad (55)$$

where, R_H – Rydberg energy of hydrogen atom = 13.6eV

m_0 – Electron rest mass

ε_r – Dielectric constant (for cubic GaN = 9.7)

μ – reduced mass:

$$\frac{1}{\mu} = \frac{1}{m_e^*} + \frac{1}{m_h^*} \quad (56)$$

where, m_e^* - electron effective mass (for cubic GaN = $0.13m_0$)

m_h^* - hole effective mass (for cubic GaN heavy hole = $1.3m_0$).

Using the values stated above, the ground state ionization energy of an exciton in cubic GaN can be evaluated as 17meV, which sits above the average thermal energy for most of the temperature range studied.

5.2.2 Time-resolved Photoluminescence of Mg-Doped Cubic GaN

The time-resolved PL decays were recorded at the emission energies of the main spectrum peaks; the D^0-A^0, the D^0-A^0_{Mg}, the blue band and the excitonic peak. As was the case with the cubic AlGaN layers, discussed in Section 4.1.3, a single exponential fitting function was able to achieve fits with high quality factors to the decay curves and allow a representative decay constant, τ to be determined for each decay:

$$I(t) = I_0 e^{-(t-t_0)/\tau} \quad (57)$$

The decay constants were calculated for the emission peaks as a function of temperature and are shown in Figure 5.5. The D^0-A^0 peak decay exhibited similar behaviour at lower and higher doping levels. The decay time started at a value of around 4ns at T ~ 4K and then decreased steadily as the temperature was increased. The decay for the lower doping level wafer had sped up to near the measurement response time by T = 60K, whilst the more heavily doped layer's decay remained slightly slower up to T = 100K. This result indicated

weak localisation at the band tails, with stronger localisation in the sample with the greater concentration of dopant impurities, and hence greater range of localisation sites.

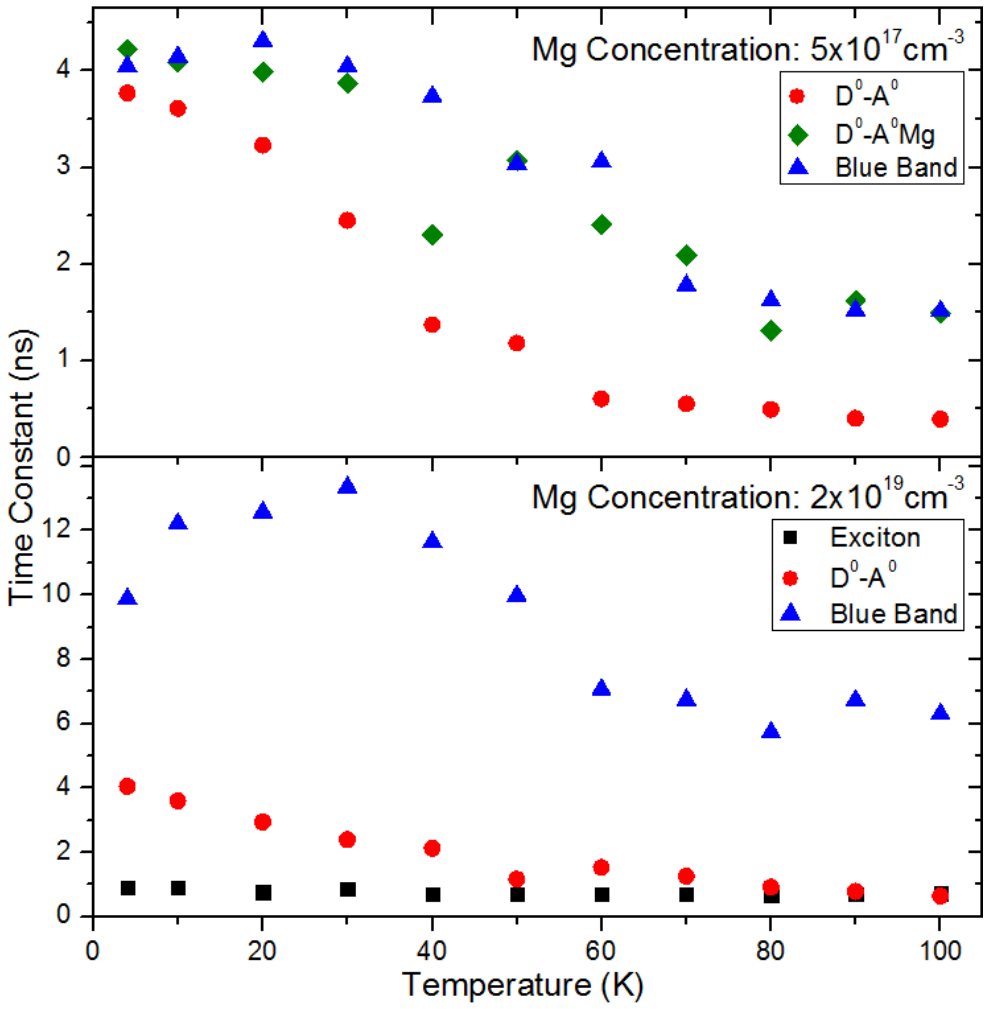

Figure 5.5 Plot of PL decay constant against temperature for Mg-Doped cubic GaN wafers of different dopant concentrations.

The decay times for the D^0-A^0_{Mg} emission followed a similar trend to the main donor-acceptor emission, but with a consistently longer decay across the temperature range. The longer decay is probably the result of stronger localisation on the deeper magnesium acceptor level resulting in reduced recombination overlap between involved carriers.

The exciton peak had a very fast decay that remained unchanged across the entire temperature range. Since the electron and hole making up the exciton are held close to each other, the overlap for recombination is large. The carriers do not have to travel far to reach

each other, resulting in a fast and efficient recombination and hence short decay unaffected by temperature changes.

The blue band in cubic GaN:Mg could not be fitted as well as the other decays owing to a reduced signal to noise ratio and a reduction in exponential-like behaviour compared to other decay curves. This was most likely a consequence of the extremely long decay for this peak evident from the decay curves. The decay was longer than the interval between laser pulses, so emission had not returned to the zero level before the next laser pulse arrived, resulting in continuous summing of a high background noise level along with the PL emission peak. If the measurement could be conducted with a lower repetition rate laser, clearer decays could possibly be obtained.

Despite the difficulty in fitting, it is evident from Figure 5.6 that the blue band had a long lifetime at low temperature. The lifetime was even longer at the higher Mg doping level. The time taken to decay decreased slowly with increasing temperature and was significantly longer than the D^0-A^0 peak decay throughout the temperature range studied.

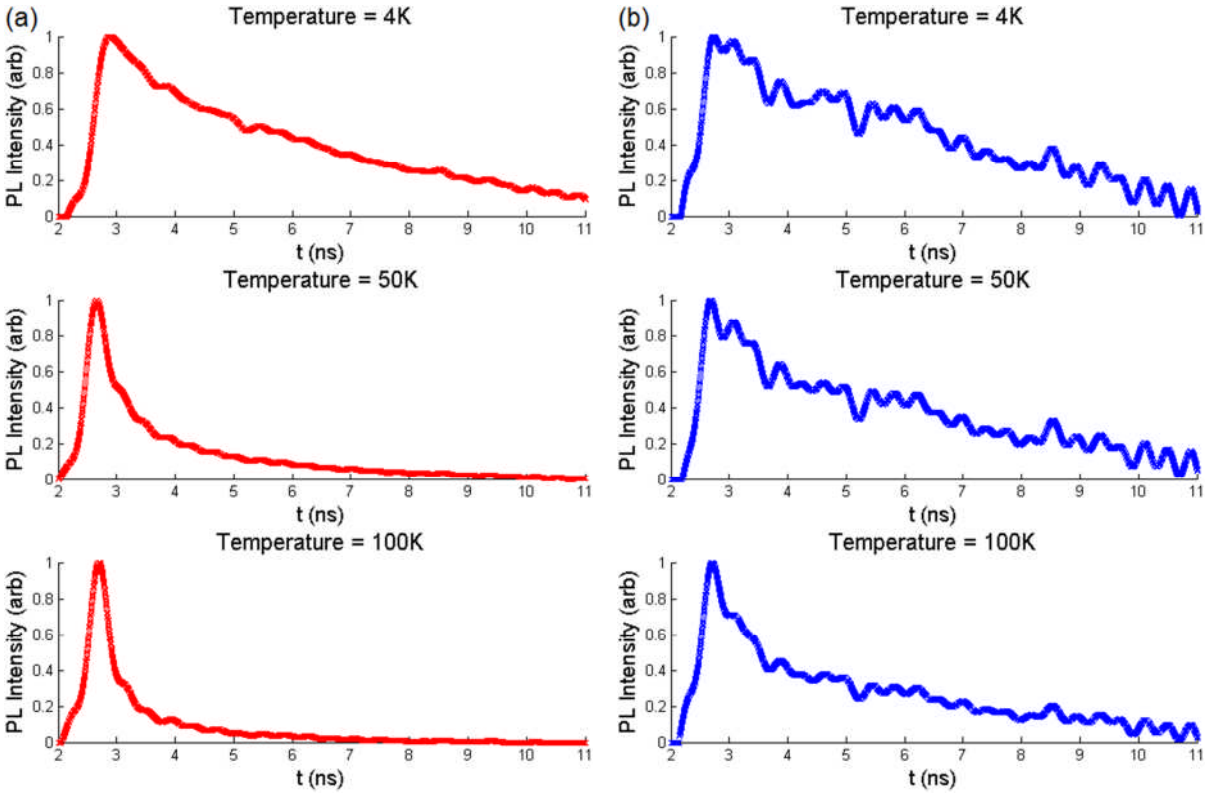

Figure 5.6 PL decay curves at different temperatures for (a) D^0-A^0 and (b) blue band emission from cubic GaN wafer with Mg dopant concentration of $2\times10^{19}cm^{-3}$.

Long and non-exponential blue band lifetimes have been observed in hexagonal GaN [52]. A non-exponential decay indicates that many different recombination paths are contributing to the emission, caused by the inhomogeneous spatial separation of localised states. The relative stability of the blue band lifetime with temperature variation is also noted in hexagonal GaN [113], and is indicative of dominant radiative recombination between donors and acceptors of large ionization energy. The temperature needs to be raised significantly for the trapped carriers to be ionised and escape to non-radiative recombination sites.

5.2.3 Transport Measurements of Mg-Doped Cubic GaN

Transport measurements were performed on the doped GaN samples to evaluate the carrier concentration and mobility. The electrical contacts were applied to the sample corners in a Van der Pauw arrangement. The conductivity of the layer was determined using a sourcemeter and the mobility was obtained from a Hall measurement as explained in the experimental chapter (Section 3.5).

Individual test samples were cut from the grown wafer. On some of these samples, the GaAs substrate was etched off chemically to prevent the potential formation of an inversion layer at the substrate/film interface. Transport measurements were conducted on free-standing doped GaN as well as samples with the substrate still attached. For the conducting wafers it was found that the difference in conductivity between free-standing and unetched samples was fairly small, indicating that the presence of the substrate had minimal effect on the measurement.

Sample	Mg Concentration (cm^{-3})	Thickness (μm)	Substrate	Conductivity ($\Omega^{-1}m^{-1}$)	Mobility ($cm^2V^{-1}s^{-1}$)
SN-710	5×10^{17}	0.57	Attached	0.03	-
SN-712	9×10^{18}	0.55	Attached	0	-
SN-713	2×10^{19}	5.66	Attached	0.43	-
			Etched	0.99	-

Table 5.3: Measured electrical properties of Mg-doped cubic GaN wafers.

The room temperature electrical properties of the Mg-doped GaN films that could be determined are shown in Table 5.3. The Hall voltage could not be measured for any of these

samples since they did not display the Hall Effect when subjected to a magnetic field. When the magnetic field was reversed in direction, the measured cross-sample voltage offset did not change polarity as expected.

It was verified that the lack of a successful measurement was not due to experimental factors. The contact resistance was evaluated by applying four square contacts in a row to the conducting surface of some samples and measuring with a voltmeter the resistance between contacts going along the row. For both Mg and Si-doped layers, the resistance increased linearly going from contact to contact, so the resistance of the metal-GaN contact must have been low compared to the GaN layer resistance.

This test only measured the resistance for a single voltage input however so it is possible that the contacts had rectifying behaviour that could have affected the Hall measurement. Performing an current-voltage sweep of the contacted sample could clarify this issue.

The effect of UV light illumination on the sample conductivity was assessed by applying voltage to the sample and measuring the current with a sourcemeter whilst a λ=220nm laser was focused onto it. The purpose of this was to determine whether carriers are being held in traps such as DX centres, where the Si donor atom sits in a displaced position away from the normal lattice position [114]. For both Mg and Si-doped samples, incident light caused a change in measured current of only ~1%. This indicates that optically activated carrier trapping is not a significant factor for the electrical conductivity of these samples.

Unreliable Hall measurements have been encountered for Mg-doped cubic GaN by Martinez-Guerrero et al. [66] and were linked to structural defects that trap impurity atoms. The conductivity for the Mg-doped layers was found to be very low despite the PL and SIMS data clearly showing successful Mg incorporation into the layers.

These results suggested that strong self-compensation was affecting the Mg-doped layers. Self-compensation refers to the formation of complexes of opposite charge to the dopants that cancel out the dopant contributions. Self-compensation effects have led to high resistance material in studies of hexagonal Mg-doped GaN [115].

5.2.4 Discussion of Blue Band Emission from Mg-Doped Cubic GaN

The cause of the blue band emission from Mg-doped cubic GaN has not been well established in the literature up to this time, but the results obtained in this work have been very informative towards this end.

In hexagonal Mg-doped GaN, the blue band has been attributed to a donor acceptor pair transition between shallow Mg acceptors and a deep donor level [113, 115, 116]. The deep donor is identified as a nitrogen vacancy/magnesium acceptor complex [113, 116]. The formation of this complex is believed to be the compensating mechanism for Mg doping.

The charged nitrogen vacancies form during growth and are mobile and hence free to combine with the acceptors. The nitrogen vacancy formation energy decreases with increasing Mg dopant concentration, resulting in a greater degree of compensation at the higher doping level. This is evidenced by the subsequent stronger blue band emission in our cubic films.

Our transport measurements on Mg-doped cubic GaN have shown that heavy compensation is occurring, and this could be due to the formation of a similar nitrogen vacancy/Mg acceptor complex. Our time-resolved temperature dependent PL indicates that blue band emission in cubic material is due to a donor-acceptor pair transition between states of high ionisation energy, as observed in hexagonal studies.

Given the similarities between our results and those taken from hexagonal material, we therefore propose that the model of recombination between shallow Mg acceptors and deep donor nitrogen vacancy/Mg acceptor complexes as the origin of the blue band emission is suitable for cubic GaN. This would account for the compensation effects on display and be appropriate for the emission energy involved. The recombination is represented in Figure 5.7.

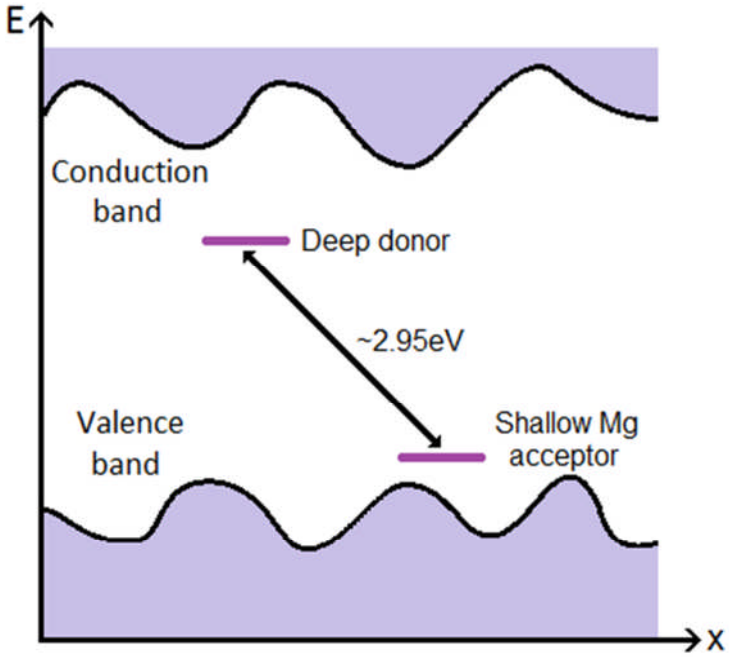

Figure 5.7: Energy level diagram illustrating the recombination leading to blue band emission in Mg-doped cubic GaN.

Since limited information is available about the binding energies of dopants like Mg in cubic GaN, a detailed analysis of the emission energy between the proposed recombination levels for the blue band cannot be performed. This leaves open the possibility of other contributors to the blue band emission, such as recombinations involving other impurity levels.

Kwon et al. [113] suggest an alternative recombination between a shallow donor and a deep Mg acceptor for hexagonal material. Oxygen, which is often found in undoped GaN [52] acts as a shallow donor [117]. Further SIMS analysis of the samples could identify the level of oxygen present.

The electronic properties of cubic Mg-doped layers could potentially be improved by post growth treatment designed to disassociate the complexes and counteract the compensation process. Nagamori et al. [118] use rapid thermal annealing under IR halogen lights in nitrogen atmosphere for the electrical activation of Mg-doped hexagonal GaN grown by MOVPE. The anneal reversed the passivation caused by Mg-H complexes.

Hautakangas et al. [119] used positron annihilation to identify Mg-V_N complexes as a major compensating centre in Mg-doped hexagonal GaN grown by MOCVD, in addition to Mg-H

complexes. They discovered that annealing at 500-800°C under N_2 for five minutes improved net space charge concentration considerably and led to a reduction in the number of measured complexes. They were unable to observe the complexes in an MBE test sample and this was attributed to the lack of hydrogen during MBE growth. They were however able to measure reasonable p-type conductivity in this MBE sample.

An anneal straight after growth was used previously at Nottingham to improve hole concentration in cubic GaN doped with manganese (Mn) [46]. These sources suggest that post-growth annealing is a potential avenue of future research in this area, with the potential to improve sample conductivity, as well as shine more light on the origin of the compensation and blue band emission in Mg-doped cubic GaN.

5.3 Study of Si-Doped Cubic GaN

Silicon is used as the main n-type dopant for GaN. The sequence of optical and electrical measurements performed on Si-doped cubic GaN was the same as for the Mg-doped material.

5.3.1 Photoluminescence Spectra of Si-Doped Cubic GaN

The time-integrated PL spectra of Si-doped GaN samples are shown in Figure 5.8. Many of the spectral features are similar to those found on the Mg-doped GaN spectra. These include the X and D^0-A^0 peaks, observed at 3.3eV and 3.15eV respectively. Although there is a small low energy tail in each case, there is no broad deep band such as the blue band caused by Mg doping.

In one of the samples, the very thickest studied, there is a peak at an energy corresponding to that of hexagonal GaN, indicating a significant density of hexagonal inclusions. This is not surprising, as increasing amounts of hexagonal inclusions in thicker cubic layers have been observed in this growth system before [11].

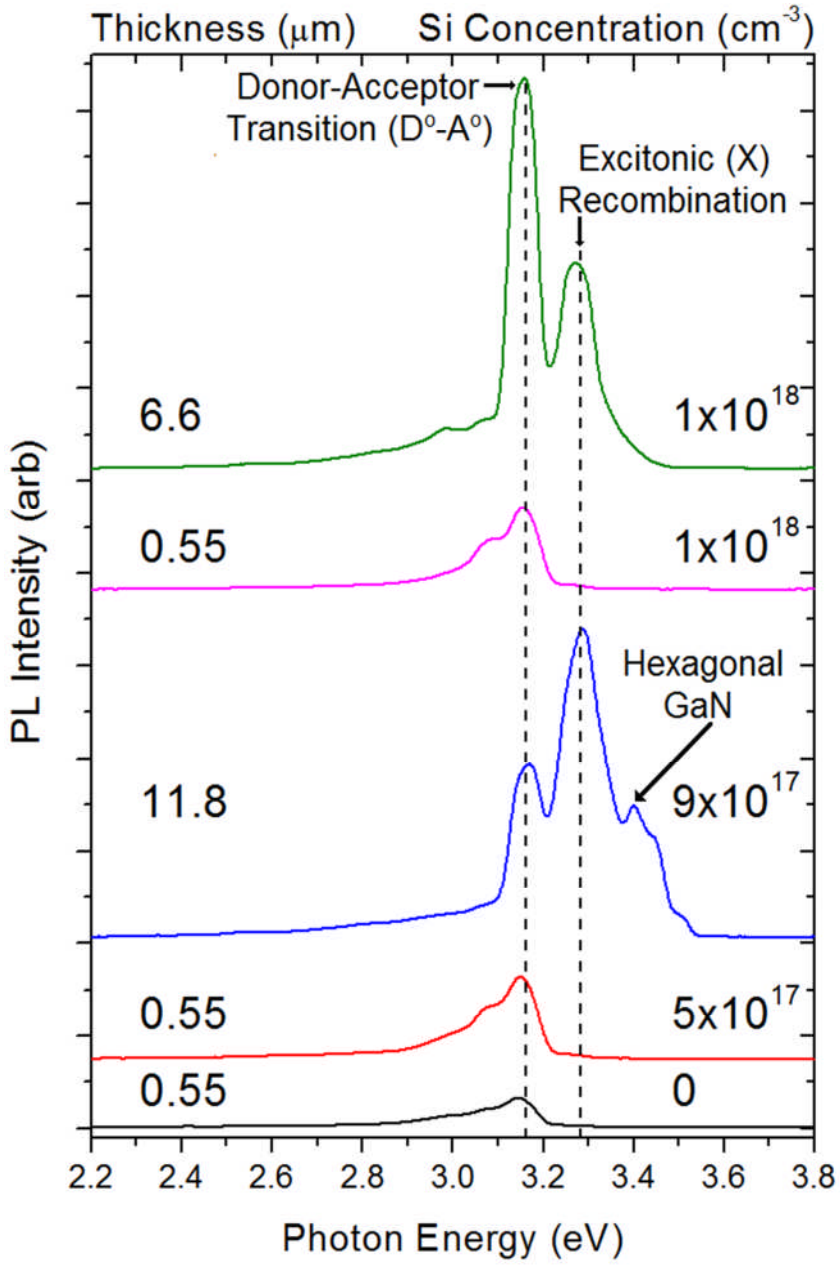

Figure 5.8: PL spectra for Si-doped cubic GaN wafers recorded at T=4K. The layer thickness and Si dopant concentration from the SIMS measurements are also shown.

The origin of the small peaks between energies of 3.0eV and 3.1eV are unclear although their low energy suggests the involvement of a relatively deep impurity. As and Lischka [55] observed peaks in this region on their undoped sample spectrum and associated them with transitions involving an arsenic impurity acceptor and a donor or conduction band electron.

They also observed that as the Si doping level was increased, the D^0-A^0 peak broadened and shifted to higher energy before merging with the excitonic peak and shifting towards the

energy of cubic GaN. This effect was not seen in our samples, most likely since their layers covered a much wider range of Si doping levels.

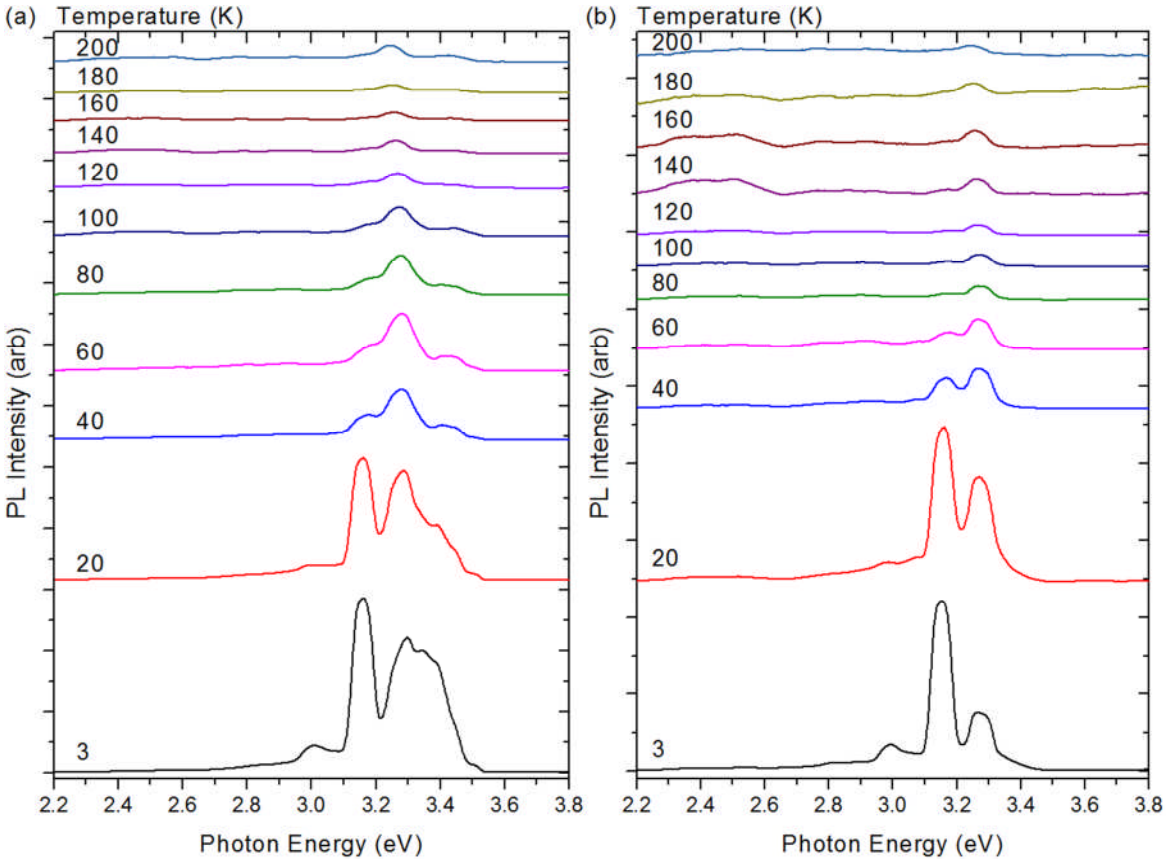

Figure 5.9: Temperature dependent PL spectra for Si-doped cubic GaN wafers with dopant concentrations of (a) $9\times10^{17}cm^{-3}$ and (b) $1\times10^{18}cm^{-3}$. The high temperature spectra (T>140K) have been scaled up for clarity.

The temperature dependence of the PL spectra was also measured and examples are shown in Figure 5.9. The intensity of the D^0-A^0 peak decreased rapidly as the temperature was increased. The exciton peak intensity decreased much more slowly, whilst shifting towards lower energy at higher temperatures and becoming the main feature of the room temperature spectrum. The hexagonal peak is also still present at room temperature. This behaviour is also similar to the Mg-doped case and points to well-understood band tail localisation effects for the donor-acceptor peak carriers.

5.3.2 Time-resolved Photoluminescence of Si-Doped Cubic GaN

As with the temperature dependent time-integrated PL, the time-resolved data for Si-doped material painted a simple picture. Plots of the fitted decay lifetimes are shown in Figure 5.10. In each case, the D^0-A^0 peak decay time decreased rapidly with increasing temperature, indicating that the recombination involves weakly localised carriers on band tail fluctuations and impurities. The decay time of the excitonic peak was extremely fast and barely changed over the entire temperature range.

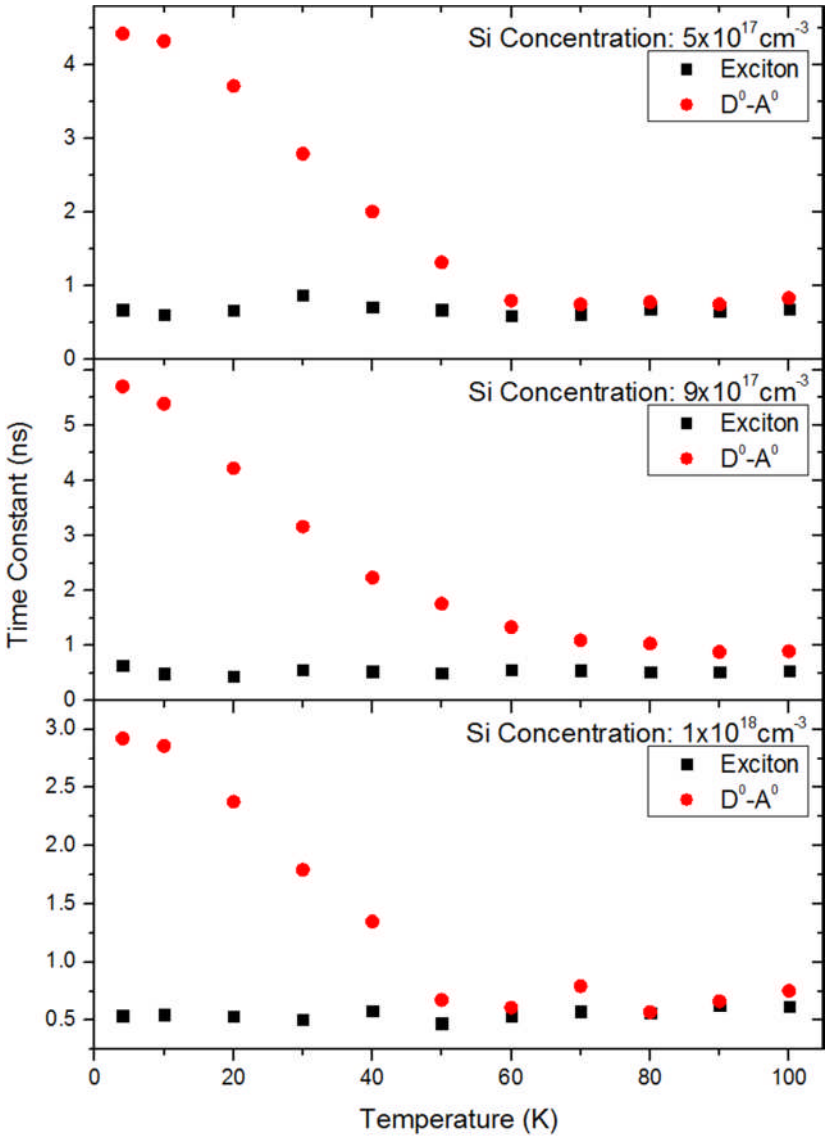

Figure 5.10: Plots of PL decay time against temperature for cubic GaN wafers doped with different amounts of silicon.

It is evident from Figure 5.10 that very similar time-resolved dynamics were observed over the full range of Si doping levels studied. This suggests that no significant changes in sample behaviour occurred over this range. Based on the PL, the Si dopants appear to act as impurity localisation sites in the band tails.

5.3.3 Transport Measurements of Si-Doped Cubic GaN

The electrical values measured at room temperature for Si-doped samples are shown in Table 5.4. In similar fashion to the Mg-doped layers, we encountered difficulty in measuring reliable Hall voltages for many of them. The Hall measurement was successful for the thin layers even though thicker layers with the same Si concentration did not display the Hall Effect properly. The conductivity of the thinner layers was also considerably higher. This indicated that the thickness of the layer was having a greater effect on the electrical properties than changes in the doping level. This result led to the surfaces of the samples being SEM imaged to look for differences in sample morphology between sub-micron and thicker layers.

Sample	Mg Concentration (cm^{-3})	Thickness (μm)	Substrate	Conductivity ($\Omega^{-1}m^{-1}$)	Mobility ($cm^2V^{-1}s^{-1}$)
SN-715	5×10^{17}	0.55	Attached	126.4	3.94
SN-720	9×10^{17}	11.8	Attached	0.88-3.45	-
			Etched	0.94	-
SN-717	1×10^{18}	0.55	Attached	136.8	9.53
SN-721	1×10^{18}	6.6	Attached	0.01	-
			Etched	0.02	-

Table 5.4: Measured electrical properties of Si-doped cubic GaN wafers.

We were able to verify that the sub-micron samples with silicon dopant concentrations of $5.0\times10^{17}cm^{-3}$ and $1.0\times10^{18}cm^{-3}$ as measured by SIMS showed n-type conductivity with bulk carrier densities of $2.0\times10^{18}cm^{-3}$ and $9.0\times10^{17}cm^{-3}$ respectively. The bulk carrier densities were hence fairly similar to the dopant concentrations. The mobility was determined as $\mu = 9.5cm^2/Vs$ for the higher doping level as indicated by SIMS and $\mu = 3.9cm^2/Vs$ for the lower doping level.

Mobility values found in other studies of Si-doped cubic material include $100cm^2V^{-1}s^{-1}$ for the concentration $3\times10^{19}cm^{-3}$ [55] and $170\text{-}50cm^2V^{-1}s^{-1}$ for concentrations of 3×10^{18}-$4\times10^{19}cm^{-3}$ [66]. The mobility of our sub-micron samples are an order of magnitude lower,

suggesting further development of the growth technique is needed to improve it. Low mobility in hexagonal GaN:Si has been attributed to electron scattering at dislocations [120], so our mobility may be limited by stacking faults. Rectifying electrical contacts or compensation effects related to the cubic structure may also be affecting the measured mobility.

5.3.4 Scanning Electron Microscope Images of Si-Doped Cubic GaN

The Figures 5.11 and 5.12 show SEM images of the surface of one sub-micron thickness Si-doped layer and another layer of similar dopant concentration that is much thicker. The scale of each image is the same as they were both recorded at 5000× magnification and show a 25μm field of view. Despite this, the thin sample has a very smooth and featureless surface whilst the thick structure's surface features micrometre-scale lumps and pits.

These defect features could be acting as traps for impurity carriers and therefore reducing conductivity in the thick doped layers and preventing a clear Hall Effect from emerging when a magnetic field is applied. Similar SEM images are shown for sub-micron and thick Mg-doped films in Figures 5.13 and 5.14. The disparity between the smooth morphology and the large scale structures is once again evident, but limited conclusions can be drawn from these images considering there is much less of a contrast between the electrical properties of thick and thin Mg-doped wafers.

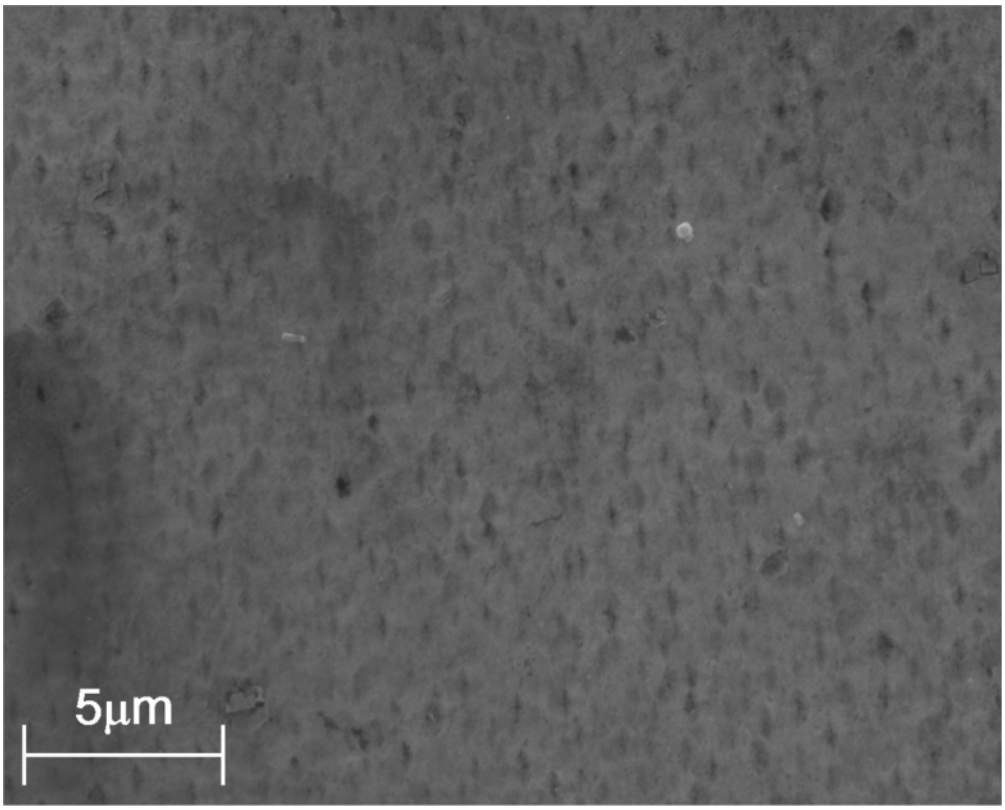

Figure 5.11: SEM image of the surface of a 0.55µm thick Si-doped cubic GaN sample with Si concentration of $1\times10^{18}cm^{-3}$.

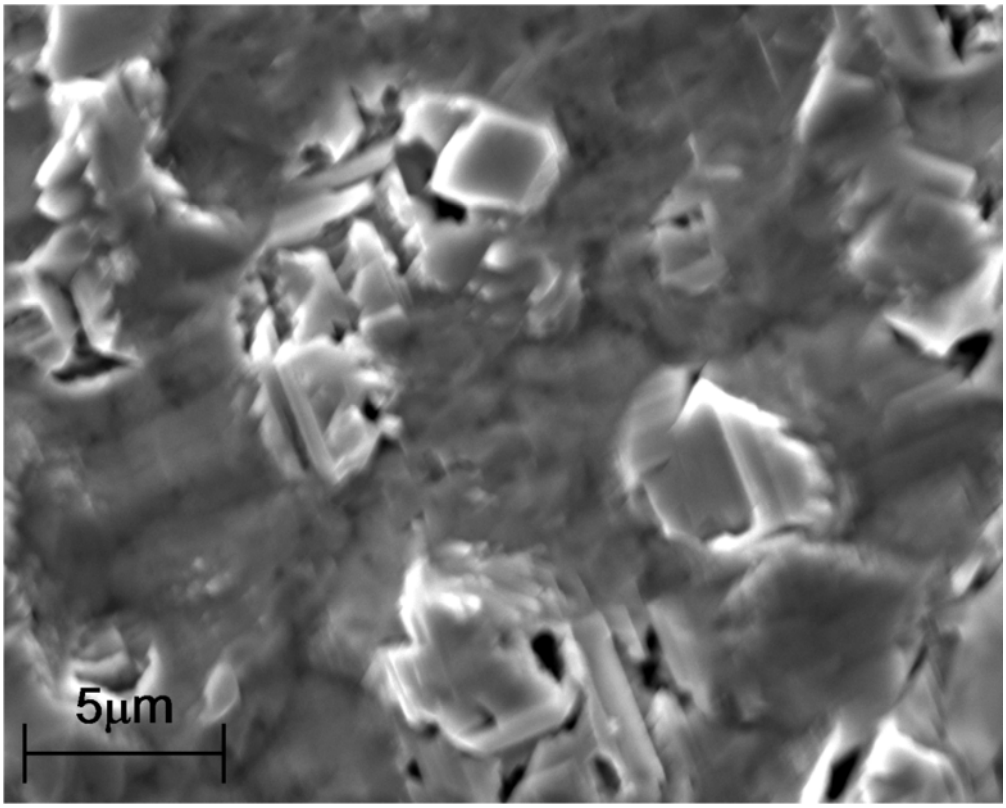

Figure 5.12: SEM image of the surface of an 11.8µm thick Si-doped cubic GaN sample with Si concentration of $9\times10^{17}cm^{-3}$.

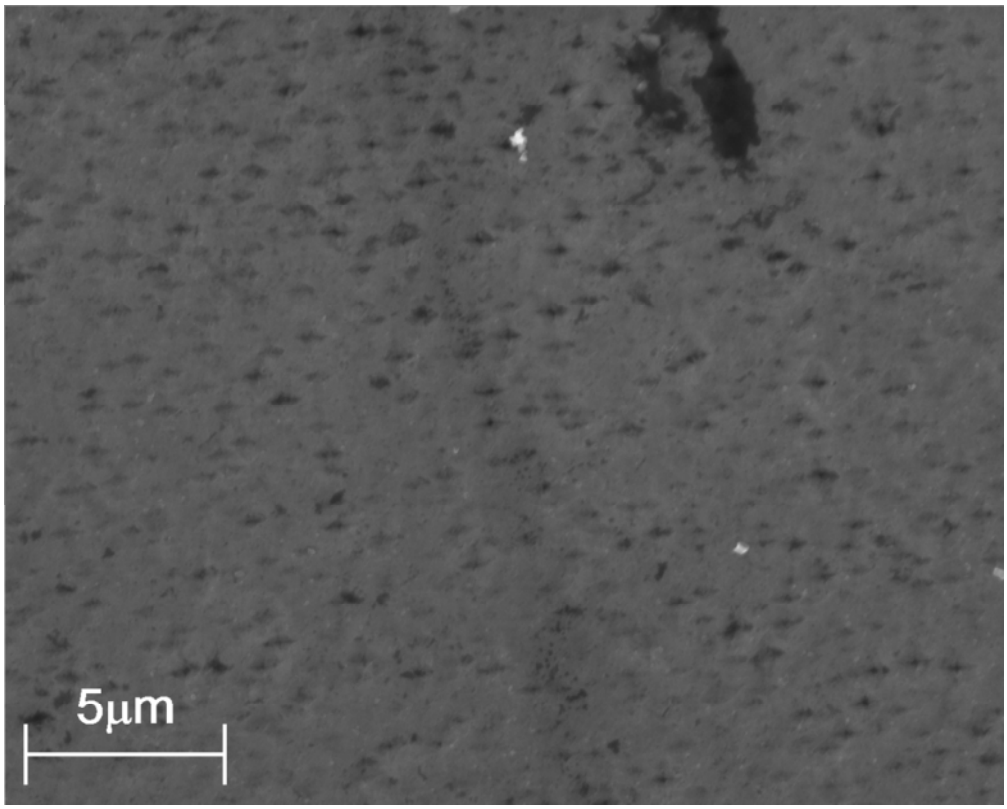

Figure 5.13: SEM image of the surface of a 0.57µm thick Mg-doped cubic GaN sample with Mg concentration of $5\times10^{17}cm^{-3}$.

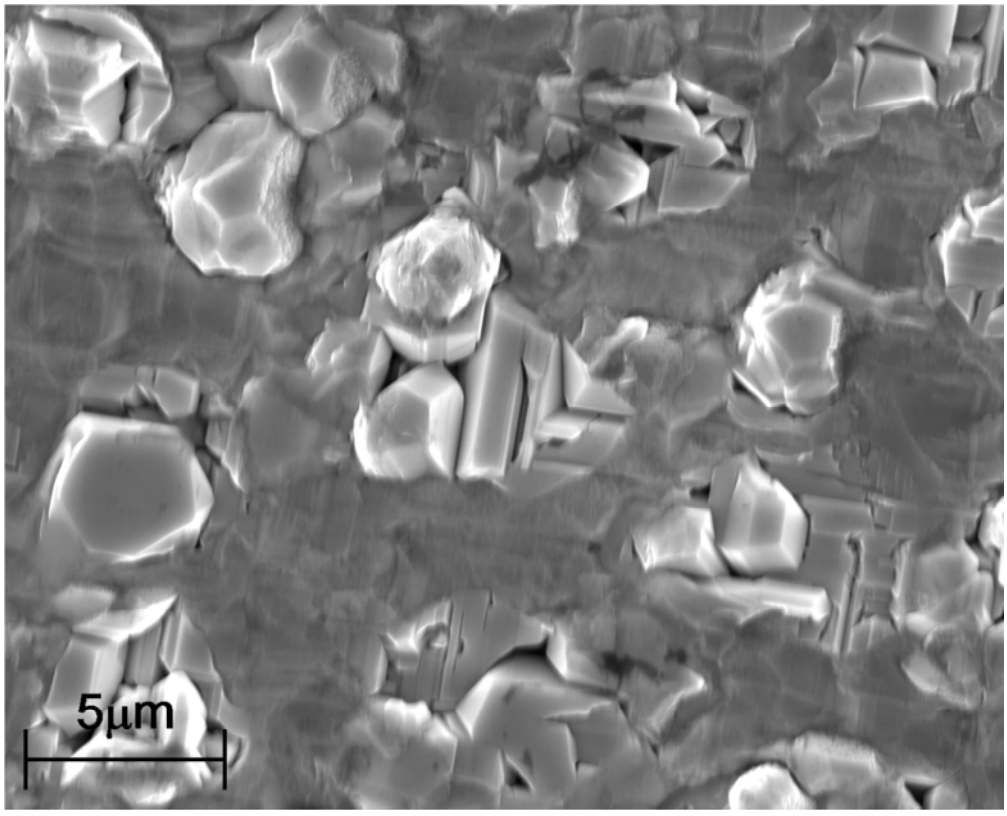

Figure 5.14: SEM image of the surface of a 5.66µm thick Mg-doped cubic GaN sample with Mg concentration of $2\times10^{19}cm^{-3}$.

These SEM images have shown that thick growth, a necessary condition for the substrate removal process has introduced additional complications that may be limiting conductivity and preventing the Hall measurement from being performed. Since the conductivity was found to be hardly affected by the presence of the substrate or otherwise, thick growth could be avoided in future studies whilst the growth parameters of the thin layers are optimised.

5.4 Conclusions for Doped Cubic GaN

We have presented results for the PL and transport characteristics of cubic GaN doped with Mg and Si. We did not observe major changes in the PL emission behaviour of GaN:Si samples over the range of concentrations studied. Other studies on cubic GaN:Si have shown that significant changes occur in the PL spectrum as more silicon is added, so a wider range of doping levels could be studied in the future. The temperature dependent and time-resolved PL suggest that simple localisation effects govern the band tail donor acceptor pair emission.

Low thickness GaN:Si was the only type of doped cubic GaN in which the Hall mobility could be reliably measured, and this was found to be lower than in other studies. Carrier scattering on defects was highlighted as a possible cause of this, indicating that improvements in growth are needed for doped cubic GaN. The mixture of thick and sub-micron wafers made the identification of trends relating the doping level more difficult to identify since the thickness affected PL emission and electrical properties significantly.

Time-resolved results in conjunction with conductivity tests suggest that the model used to explain blue band emission in Mg-doped hexagonal GaN may be applicable to cubic material as well, a result that brings us closer to understanding the origin of this emission than previously. An exploration of post-growth treatment to nullify the effects of self-compensation leading to the blue band emission would be a promising avenue in the future. The use of other dopant species in cubic GaN, such as manganese (previously studied at Nottingham [46]) or carbon [47], would also be suitable for future work.

Chapter 6: Characterisation of InGaN Structures

In this chapter, the results of PL studies of InGaN and pure InN structures are presented. These structures were grown on Si (111) substrates and so possess the hexagonal structure rather than the cubic one. The removal of mismatch related strain and the subsequent reduction in polarization fields give nanocolumns similar advantages over hexagonal to cubic films. Development of the growth of InGaN is also an important step towards the device applications that can benefit from the wide energy range of bandgaps unlocked by introducing indium into the III-nitride system. These layers were all grown in the nanocolumn structure, whilst some were grown so that the columns coalesced into one continuous layer.

6.1 Photoluminescence of InGaN Nanocolumns

The first set of studied samples consisted of $In_{0.5}G_{0.5}N$ nanocolumns grown on a p-Si (111) substrate under varied growth conditions. The indium fraction is a nominal value based on the indium flux, which was constant between samples. The specifications of these samples are shown in Table 6.1, along with an assessment of the material structure based on SEM images taken at the University of Bristol. The column heights could only be determined from images featuring toppled columns. The growth temperature values were obtained from the thermocouple within the heating element since the pyrometer previously utilised in this system is not sensitive to the low temperatures of InGaN growth.

Sample	Growth temp. (°C)	NC diameter (μm)	NC spacing (μm)	NC height (μm)
SN-670	440	~0.1	~0.1	
SN-668	492	~0.1	~0.1	
SN-672	518	~0.2	~0.4	~2.0
SN-669	544	~0.2	~0.5	~2.0
SN-673	569	~0.2-1.0	~0.3	~2.0
SN-671	595	~0.2-2.0	~1.0	

Table 6.1: This table shows the specifications of the $In_{0.5}G_{0.5}N$ nanocolumn (NC) samples studied. The diameter values were taken from SEM images.

The SEM images of the samples revealed a relationship between the growth temperature and the size of the InGaN features. For the low growth temperatures, the InGaN grew in fine, high density rods of ~100nm diameter. As the temperature was increased, the features grew

broader. At the higher end of the range, there were a large number of large irregular chunks growing amongst the thin rods. These features were as wide as 2μm on the highest growth temperature sample.

Transmission electron microscopy (TEM) studies of the nanocolumn samples were also been conducted by Cherns et al. [121] at the University of Bristol. They found that the nanocolumns were mostly free of threading defects as expected compared to continuous films. They also discovered that the nanocolumns had a core-shell structure, with a high indium content core surrounded by a gallium-rich skin, as illustrated in Figure 6.1. This was indicated by the curvature of asymmetrical rods and the cracking of the surface, indicating tension on the surface that was not present in InN nanocolumn samples. Tourbot et al. [122] have also observed the spontaneous development of a core-shell structure in InGaN nanowires grown by pa-MBE.

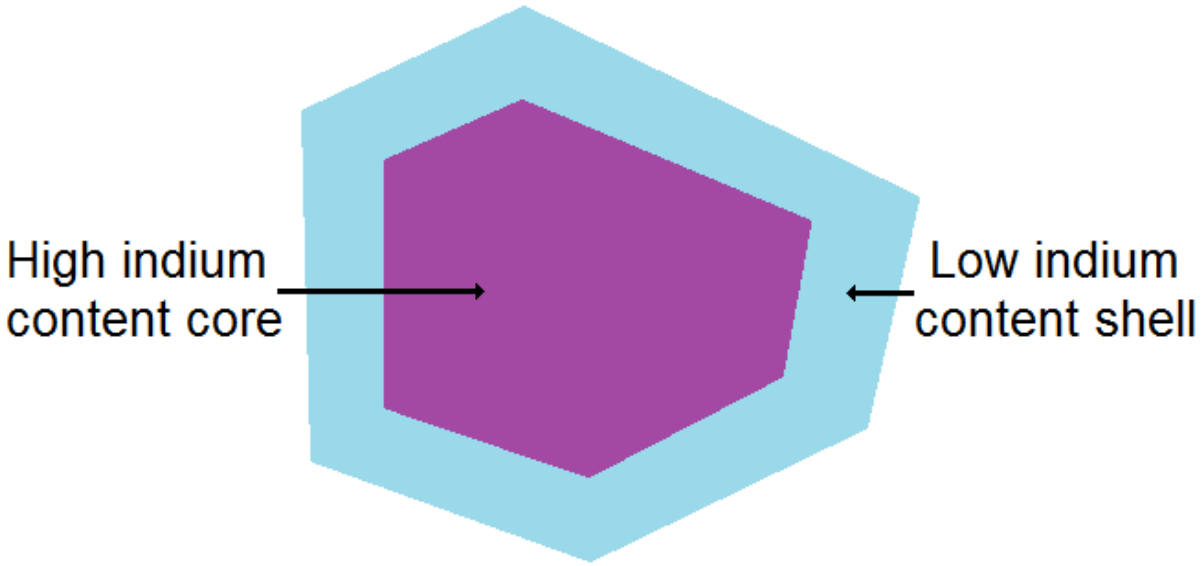

Figure 6.1: Illustration of the cross-section of a single InGaN nanocolumn showing the core-shell structure with separate regions of high and low indium concentration.

The core structure was later confirmed by cross-sectional STEM and XRD measurements. The development of this structure can be attributed to desorption of indium from the surface at the growth temperature used whilst the inner core was enclosed. Migration of indium towards the top of the columns led to additional lateral variations of the indium concentration.

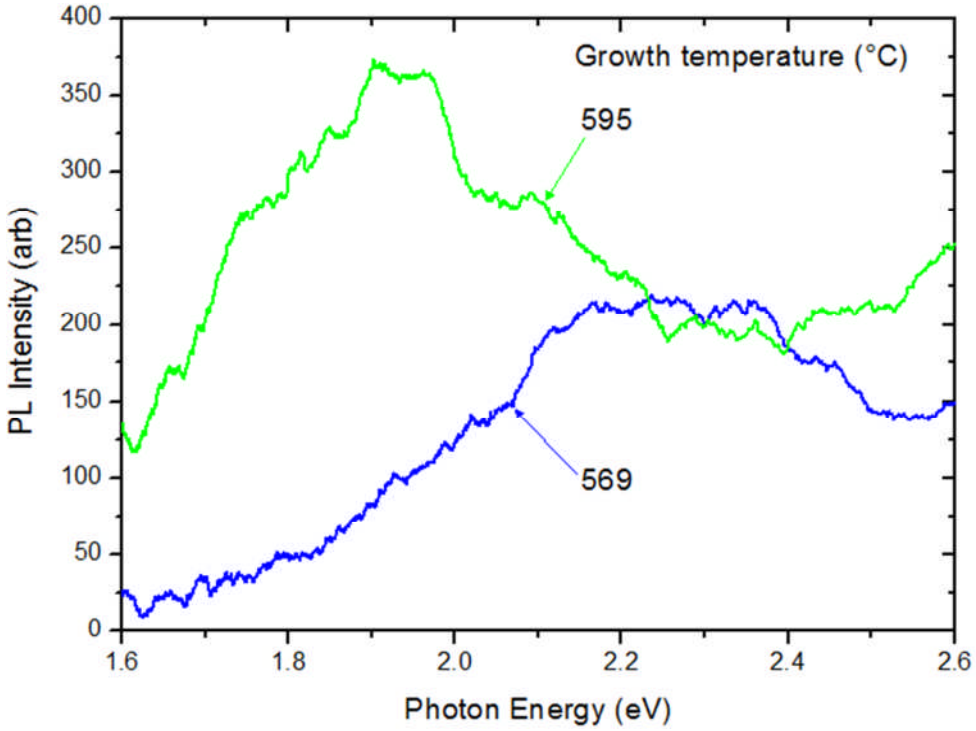

Figure 6.2: Low temperature PL spectra of $In_{0.5}G_{0.5}N$ nanocolumn arrays that were optically active.

Out of the set of samples studied, only two emitted PL spectra, and these are shown in Figure 6.2. These were the two samples grown at the highest temperatures. The 595°C sample spectrum had a broad emission peak centred at ~1.9eV whilst the 569°C sample spectrum has a slightly weaker emission around ~2.25eV. The disparity in emission energy is likely due to a different degree of indium incorporation between the samples due to differing growth conditions. The broad nature of the peak can be attributed to the varying sizes of nanocolumns, which causes each to emit at a slightly different energy.

We can use Vegard's law to estimate the indium fraction of the emitting material using values of wurtzite GaN and InN bandgap energy as 3.4eV [12] and 0.8eV [15] respectively, as well as a bowing parameter of 1.43 as used by Calleja et al. [73].

$$E_G(x) = (1-x)E_G(GaN) + xE_G(InN) - bx(1-x) \quad (58)$$

where, $E_G(GaN)$ – GaN bandgap energy

$E_G(InN)$ – InN bandgap energy.

The indium content for our two samples came out as x ~ 0.32 for the 569°C growth temperature sample and x ~ 0.45 for the 595°C sample. The estimate is rather crude as we have related the emission energy directly to the bandgap energy and bandgap values originated from other studies, whilst the core-shell structure means that the indium content is not uniform over the whole column. Furthermore, the quantum confinement brought about by the nanocolumn structure also affects the emission energy. We can however see that the indium composition is close to the midrange that was desired from the growth.

There seems to be a correlation between the emission intensity and the size of the InGaN structures. The thin, high density rods in the low growth temperature samples did not emit sufficient light to be detected. The samples with the large micrometre features did emit, and the emission was stronger when the InGaN chunks grew even larger. This may indicate a relationship between PL emission and surface effects. The structures that have a smaller surface area to volume ratio emit more strongly and would be affected less by any surface effects.

In their study of InN nanocolumns, Stoica et al. [79] state that increased growth temperature leads to higher adatom mobility and improved bonding during growth, resulting in higher quality crystals and thus higher PL efficiency. At high growth temperatures, they observed a reduction in column uniformity and density that would have to be compromised with the improved quality and PL intensities.

Stronger intensity and narrower peak widths have also been observed with higher growth temperatures for the PL of InN nanocolumns by Chang et al. [123] and for InGaN nanocolumns by Tabata et al. [75]. Growth temperature related crystal quality may hence be the primary factor affecting PL emission in our samples, ahead of the InGaN geometry.

Stoica et al. also noticed improved PL intensity for taller columns as the lower parts of the columns were subject to higher dislocation density. Taller columns were the result of higher indium-flux. Although indium fluxes were not significantly changed for samples in our set, column height may have been a contributing factor to PL emission variations.

Murotani et al. [74] studied the PL spectra of individual InGaN nanowires grown by rf-MBE on Si (111). For an increasing indium fraction, the PL peak broadened due to the alloy

fluctuation effect previously noted with AlGaN. The broadening in our samples is likely due to such fluctuations considering the un-optimised growth.

The impact of InN edge effects on the PL emission intensity is unclear. Kawakami et al. [124] suggest that surface states may contribute to non-radiative recombination centres. This is also proposed by Murotani et al. [74]. In their study of InGaN single QWs integrated into GaN nanocolumns, Kawakami et al. noted a reduced blueshift in peak energy with increasing excitation density, partially attributed to screening of piezoelectric fields by band bending at the surface. They did not however investigate experimentally any links between the edge effects and the PL intensity.

We have seen that InGaN nanocolumns possess a core-shell structure [121]. This may be the cause of the limited PL activity of the samples. The distinct boundary between the two regions likely introduces a large number of non-radiative recombination centres and may obstruct carrier diffusion into a portion of the structure. High indium content regions would also have very low PL emission energies that may lie outside of the sensitivity range of the measurement apparatus. The strong spatial variation in indium content may also explain the very broad PL emission.

Cai et al. [125] grew core-shell InGaN nanowires using chemical vapour deposition in a tube furnace. The indium content in the shells was found to be 4-10% whilst in the cores it was 30-60%. The PL spectrum featured a very broad feature formed of the combination of blue and red emission peaks. The PL data for our samples is similarly broad, but two distinct contributions cannot be distinguished.

Considering the experimental results and the literature, it is likely that the core-shell structure and the growth temperature were the key factors influencing PL emission intensity. Only at the highest growth temperatures, where crystal quality was improved and the nanostructure shapes became less regular was PL emission achieved.

6.2 Photoluminescence of Coalesced InGaN Nanocolumns

We have seen how InGaN nanocolumns are subject to the development of a core-shell structure and potentially surface effects. The coalesced structure is designed to utilise the

advantages of a continuous layer whilst still deriving benefit from the excellent structural quality of nanocolumn growth. The film initially grows as separate nanocolumns and after and a change in the growth they broaden with height and coalesce together into a continuous layer.

A set of coalesced nominal $In_{0.5}G_{0.5}N$ films were grown and studied by PL. The same N-rich growth conditions as previously were used for the initial nanocolumn phase, but the fluxes were changed to Ga-rich conditions for the second phase. The parameters of the various samples are shown in Table 6.2. The indium fraction is again nominal and based on the flux during growth. One of the coalesced layers had no indium flux during the second phase. Based on TEM images [121], the thickness of the coalesced layer was about 250nm.

Sample	Growth temperature (°C)	In fraction (x)
SN-680	492	0
SN-677	492	0.5
SN-679	544	0.5
SN-678	595	0.5

Table 6.2: This table shows the specifications of the coalesced $In_xGa_{1-x}N$ samples studied.

The low temperature PL spectra for the light emitting samples in the coalesced sample set are shown in Figure 6.3. Once again, the emission intensity was brighter in the higher growth temperature samples, whilst those at the lower end of the scale did not emit at all. The 544°C sample had a broad emission peak centred at ~1.7eV that was similar in intensity to the non-coalesced nanocolumn emission.

The 595°C sample emitted at an intensity that was over an order of magnitude higher than any other InGaN sample. This emission was also broad, peaked at around ~1.95eV and had a step on the high energy shoulder. Using Vegard's law again, the indium fraction of this sample can be estimated at x~0.43, which is very similar to the content of the non-coalesced sample grown at the same temperature.

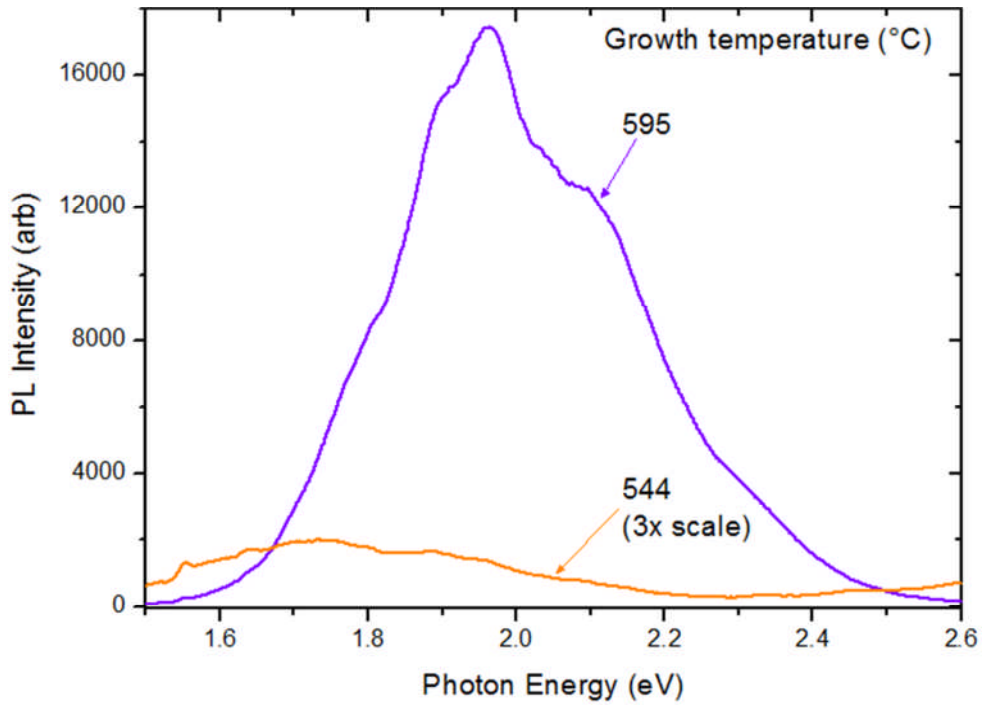

Figure 6.3: Low temperature PL spectra of coalesced $In_{0.5}G_{0.5}N$ layers that were optically active. The intensity of the 544°C trace has been scaled up for visual clarity.

A disparity in the peak emission energy between samples was again observed, likely due to differing indium incorporation between the samples. These PL spectra have shown that for the coalesced structure, the growth temperature once again had a significant effect on the ability of the sample to luminesce. The massively enhanced intensity from the highest growth temperature sample suggests that coalescence improves PL properties compared to the nanocolumn structure for this material.

Studies of binary compound nitride nanocolumns have shown that coalescence is detrimental to PL emission. Grandal et al. [78] observed a decrease of two orders of magnitude in PL for coalesced InN layers compared to nanocolumns, attributed to the generation of grain boundaries and defects as a result of coalescence and their subsequent role as non-radiative recombination sites. Stoica et al. [79] noted that the PL efficiency of their InN nanocolumns increased due to higher indium flux up to the point at which coalescence started to occur and then it decreased.

The opposite effect has been observed in our tertiary alloy coalesced layers, with a huge increase in PL intensity after coalescence. We have discussed how a phase separated core-shell structure has been detrimental to PL emission in our InGaN nanocolumns. This effect

would not have occurred in the binary compounds studied in the above sources, so the introduction of defects in the coalesced layer led to a reduction in PL efficiency.

TEM images of our coalesced InGaN show that the overgrown film consists of large grains with consistent indium composition that are up to 1μm across, with threading defects only present at the grain boundaries. These large grains are much more conducive to strong PL emission than the core-shell nanocolumns, and so an improvement is seen after coalescence, contrary to what occurs with binary alloy coalescence. This result has also been confirmed with cross-sectional CL mapping of a sample [121].

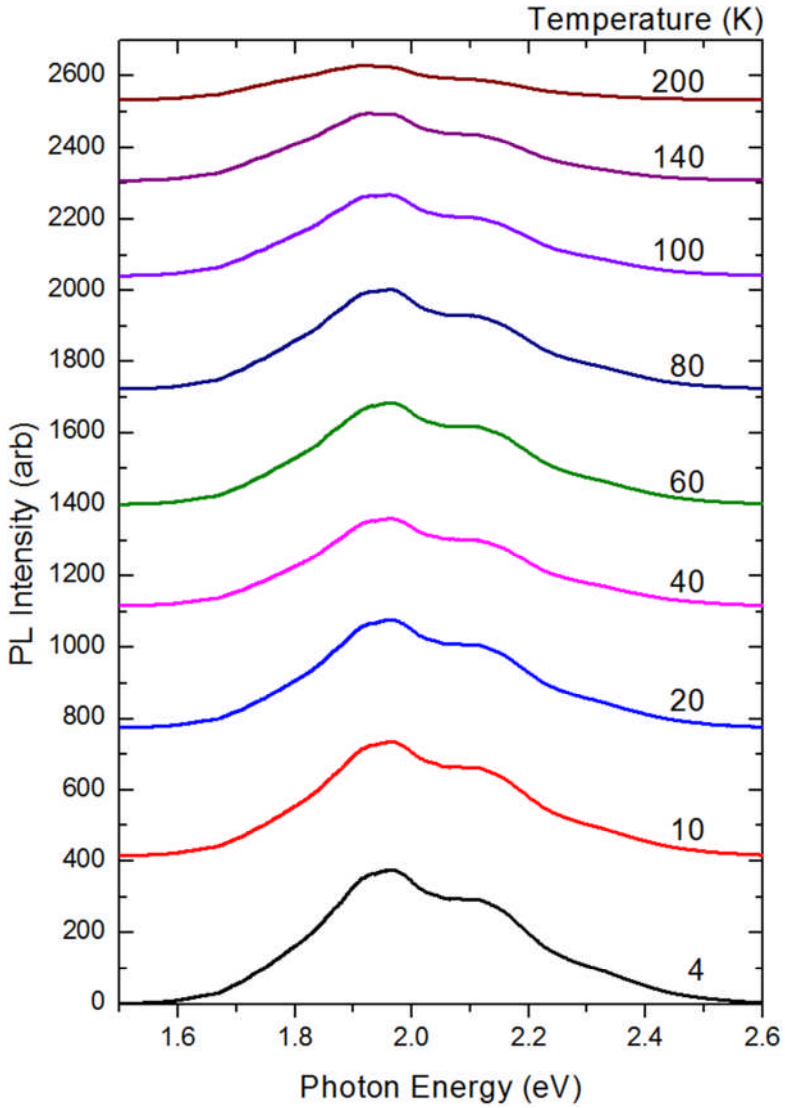

Figure 6.4: PL spectra as a function of temperature for coalesced $In_{0.5}G_{0.5}N$ film grown at 595°C.

The PL spectra of the highest growth temperature coalesced InGaN film are shown as a function of temperature in Figure 6.4. The intensity of the emission decreased steadily as the temperature was increased, but the relative intensities of the peaks remained similar. The peak energy of the main feature decreased in energy with increasing temperature, as shown in Figure 6.5.

Chang et al. [80] state that a significant variation of peak energy position with temperature from InN nanowires indicates that strong surface electron accumulation is not occurring. In their study of InGaN nanocolumns grown on GaN bases, Tourbot et al. [122] observed a s-shaped shift in the emission energy with increasing temperature for their 11% indium content sample and a simple downwards shift in energy for the 43% indium content sample.

This disparity was attributed to different localisation mechanics. In the higher indium content sample, with similar indium fraction to our own, deep potential minima related to alloy disorder were said to trap carriers until radiative recombination for the whole temperature range. In the other sample, the localisation clusters were believed to be more homogenous, allowing carriers to delocalise and diffuse to deeper states initially and then shallower states at higher temperatures as thermal filling took place. This led to the s-shaped shift for low indium content. The similar behaviour of the coalesced layer shown in Figure 6.5 to the 43% indium sample of Tourbot et al. may indicate similar localisation on deep potential fluctuations due to alloy variation is occurring in our material.

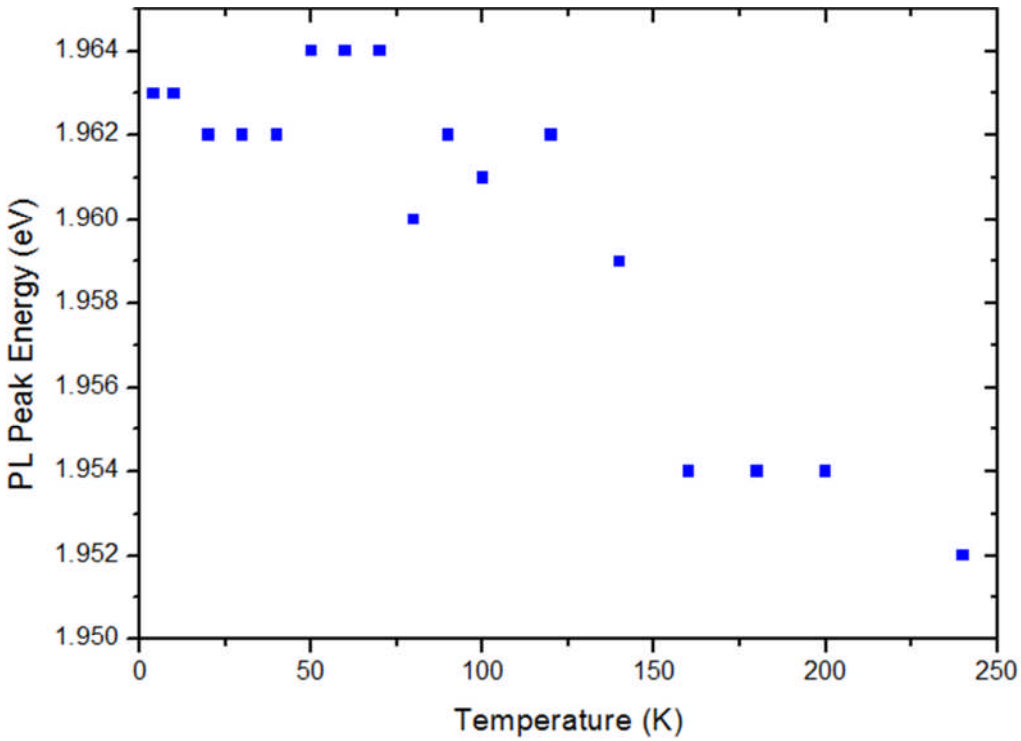

Figure 6.5: Emission energy of the near band-edge PL peak as a function of temperature.

Murotani et al. [74] studied the temperature dependent PL of single InGaN nanowires. The energy of the PL peak shifted to higher energy as the temperature increased up to 170K before shifting to lower energy as the bandgap decreased. The initial increase was attributed to the thermal activation of excitons localised on fluctuation minima. This effect is also not seen in our results, which may be due to differences in PL behaviour as a result of the coalescence such as a different degree of potential fluctuations.

We have also studied the time-resolved PL decays of the coalesced structure grown at 595°C. The measurements were taken at energies corresponding to the centre and halfway up each side of the PL peak. A typical decay, recorded at a temperature of T = 4K is shown in Figure 6.6 alongside the decay recorded at the laser emission energy. This demonstrates that the decays being measured are considerably longer than the measurement limit of the system.

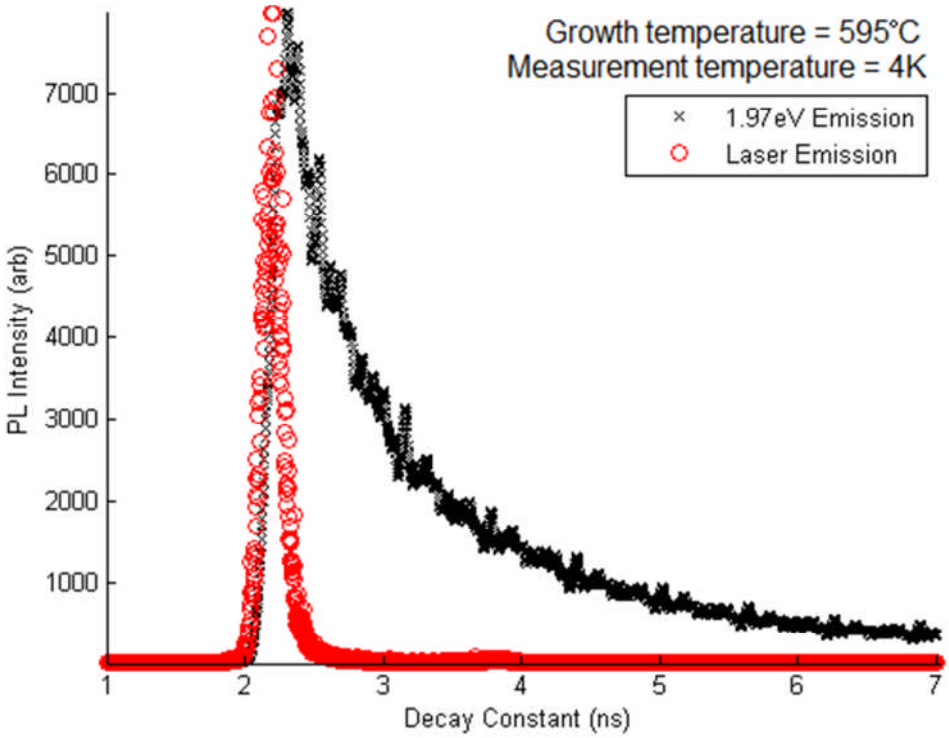

Figure 6.6: Decay curve showing the emission intensity as a function of time for the 1.97eV peak of the 595°C growth temperature coalesced InGaN layer at T = 4K. Shown for comparison is the decay at the photon energy of the laser line.

The decay constants were calculated for decays at a range of temperatures and laser excitation powers. When analysing the results, high fit quality was obtained using a single exponential function similar to the one used in previous time-resolved studies. This function is stated below in Equation (59):

$$I(t) = I_0 e^{-(t-t_0)/\tau} \tag{59}$$

The derived decay times as a function of temperature are shown in Figure 6.7. The decay is longest for the emission energy of 1.97eV, corresponding to the point of highest intensity on the spectral peak. The high energy emission at 2.26eV features faster decays whilst the low energy emission at 1.83eV decays slightly more slowly. All three emission energies behaved similarly as a function of temperature. As the temperature increased, the decay initially sped up before slowing again after T = 50K. Beyond this point the decay again sped up for the rest of the temperature range.

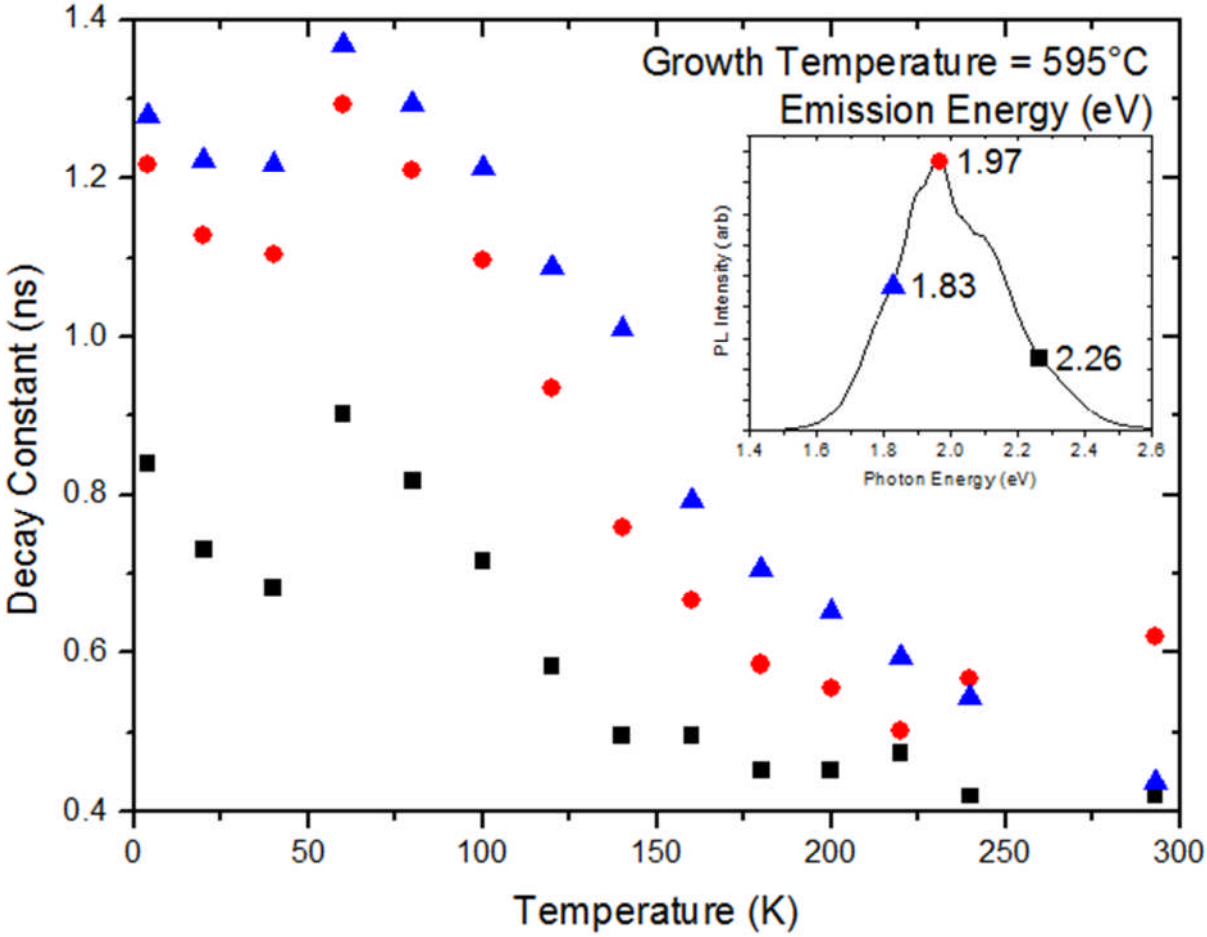

Figure 6.7: Decay time constants for time-resolved curves of the 595°C growth temperature coalesced InGaN layer at varying temperatures for emission energies shown on the PL spectrum inset.

In their TRPL study of single InGaN nanowires, Murotani et al. [74] found that the decay time was similar for emission energies lower than and at the energy of the PL peak but became shorter at higher energies. This was also attributed to exciton localisation, and is similar to our results. This suggests that localisation due to alloy fluctuations may be affecting the coalesced InGaN on some level. They also noted that the degree of localisation and the internal quantum efficiency increased as the indium concentration increased, but we did not have emitting samples from a range of indium fractions in order to make comparisons.

6.3 Photoluminescence of Graded InGaN Structure

The graded structure is a development of the coalesced layers grown previously. It is intended for a solar cell application and so is designed to absorb a broad range of photon energies. This was achieved by having the indium fraction vary vertically through the film, creating layers of different bandgap. $In_{0.5}Ga_{0.5}N$ nanocolumns were grown as previously before coalescence. In the coalesced film, there were four stages of growth lasting 30 minutes each with different indium fluxes. The different stages are all summarised in Table 6.3. All of the layers were grown at the same growth temperature of 492°C.

Growth stage	Duration (hr)	In flux ($\times 10^{-8}$ Torr)	Ga flux ($\times 10^{-8}$ Torr)
1	3	3.00	2.2
2	0.5	2.25	2.2
3	0.5	1.50	2.2
4	0.5	0.75	2.2
5	0.5	0	2.2

Table 6.3: This table shows the growth sequence for the InGaN graded structure.

The low temperature PL spectrum for the graded film is shown in Figure 6.8. The PL emission was quite weak, but had a distinct peak centred on ~2.3eV, along with a high energy plateau that continued up to the laser energy, which was higher for this sample than previously. The main peak can be attributed to emission from the higher indium concentration layers whilst the broad high energy emission is associated with the regions nearer the surface that are expected to be approaching pure GaN.

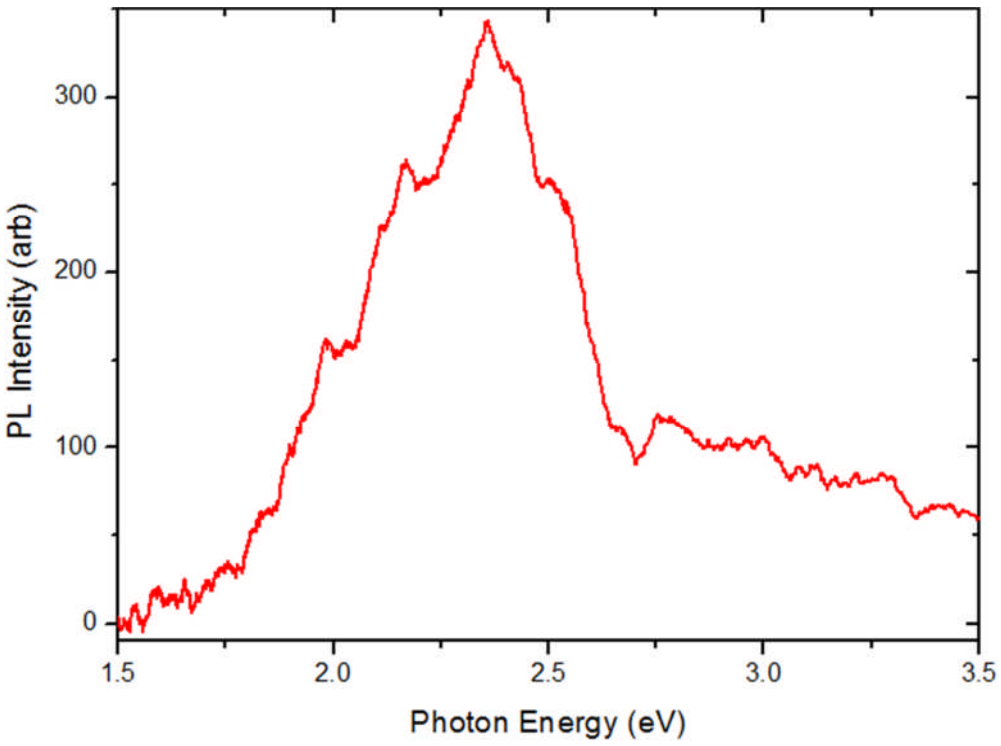

Figure 6.8: Low temperature PL spectrum of InGaN coalesced structure with vertically graded indium concentration.

Graded InGaN nanocolumns were grown by Albert et al. [126] on top of GaN nanocolumns using pa-MBE. They observed that the emission energies depended on the direction of the growth temperature gradient used to achieve varying indium content. A positive gradient, corresponding to increasing temperatures and thus decreasing indium content (going bottom to top) led to blue emission peaking at around ~2.6eV. The negative gradient had primarily green emission with the spectral peak at ~2.1eV. This was attributed to the thermal decomposition of high indium regions as the temperature was increased using the positive gradient, resulting in emission primarily from the lower indium concentration regions.

Since the indium composition of our sample was varied using fluxes rather than growth temperatures, and indium concentrations were not given in the above source, few parallels can be drawn with our results. The emission peak is similarly broad in both cases, suggesting that the indium concentration has been graded successfully in our structure. The growth temperature in this case was 492°C, considerably lower than the temperatures that resulted in strong PL emission previously. This suggests that a higher growth temperature could result in an improved graded structure. Further investigation and development is warranted in light of this.

6.4 Photoluminescence of Coalesced InN Nanocolumns

The final set of samples that we studied consisted of a coalesced structure, but with no gallium present, so the layers were pure InN. The initial nanocolumn phase was grown under indium rich conditions at a growth temperature of ~544°C. The second stage growth featured a low indium to nitrogen ratio for the coalescence. The growth temperature during this phase was varied. The differences in growth conditions between samples in the set are summarised in Table 6.4.

Sample	1^{st} In_2 flux ($\times 10^{-8}$ Torr)	2^{nd} In_2 flux ($\times 10^{-7}$ Torr)	2^{nd} phase growth T (°C)
SN-633	5.08	4.98	466
SN-632	5.08	5.00	544
SN-634	5.66	4.72	518
SN-635	5.83	5.00	590

Table 6.4: This table shows the specifications of the pure coalesced InN nanocolumn samples studied.

Since the CCD spectrometer used for the other PL measurements in this work was not sensitive to the IR wavelengths emitted by pure InN, an alternative setup was used. The details of this are covered in the experimental chapter (Section 3.2.5) but it used an IR photodiode for light detection. The laser excitation wavelength was λ=535nm from a CW laser. The low temperature PL spectra are shown in Figure 6.9.

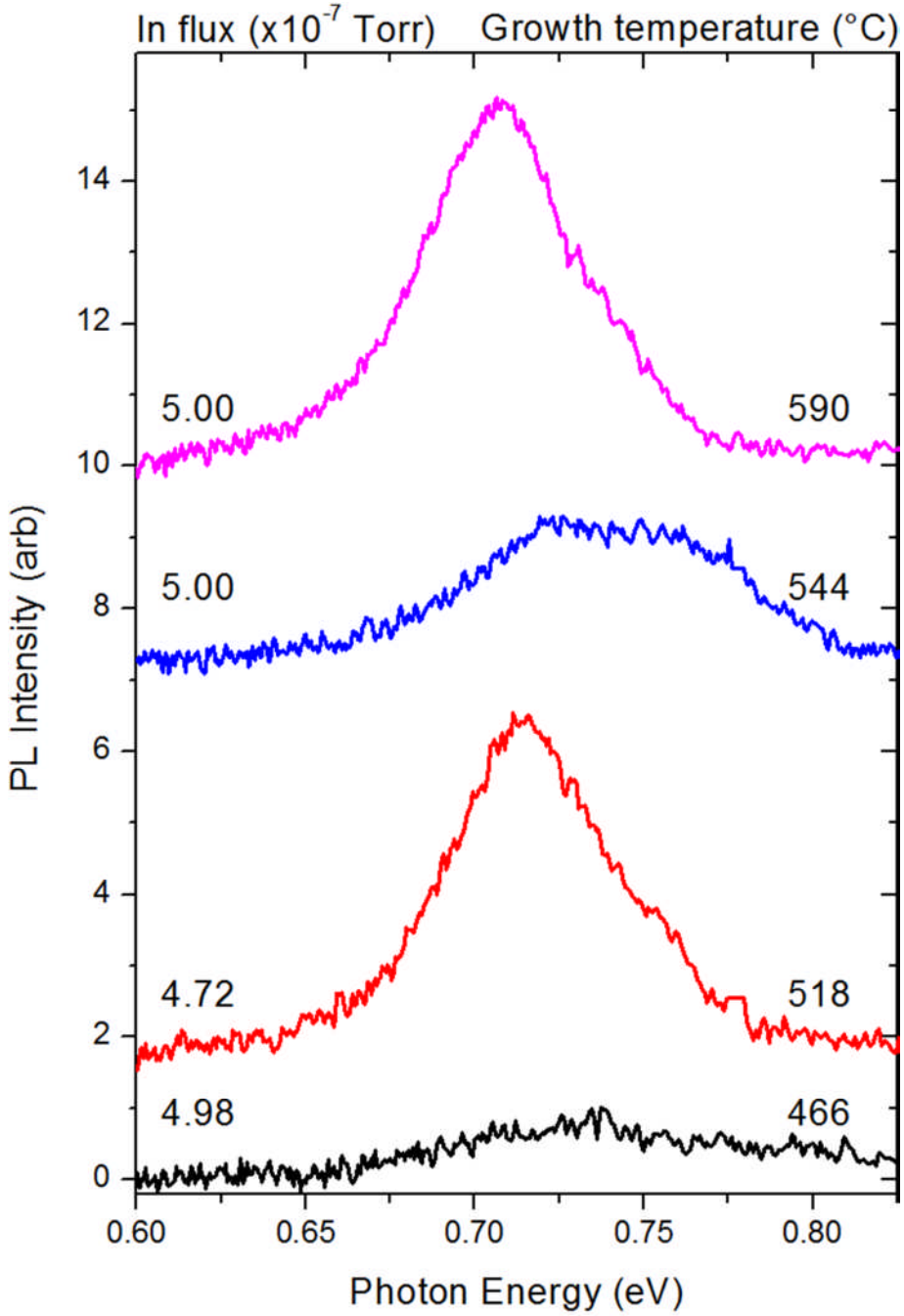

Figure 6.9: Low temperature PL spectra of coalesced pure InN films. The indicated indium flux is for the second (coalescence) phase of growth.

We were able to record distinct PL spectra from InN samples spanning a broad range of growth temperatures, not just the samples grown at the highest temperatures. This may be due to the lack of core-shell structure in the initial nanocolumn phase, or a reduced sensitivity of PL emission to growth temperature in InN compared to InGaN.

Our PL results are broadly consistent with those in the study of InN nanocolumns by Stoica et al. [79]. They observed that increasing the growth temperature shifted the emission to lower energy, narrowed the peak and increased intensity. They also found that higher indium flux caused redshifting, narrowing and improved intensity up to the point of coalescence. The higher intensity of the sample grown at the relatively low 518°C may therefore be due to a lack of coalescence in this sample on account of the reduced indium flux.

These spectra have demonstrated successful growth of coalesced InN and the use of the new infrared PL set-up. Further development of InN growth can take place from this point taking into account the importance of growth temperature and indium flux.

6.5 Conclusions for InGaN Structures

We have studied a variety of InGaN structures including nanocolumns and coalesced layers. The characterisation results have given valuable insight into how high quality, optically active InGaN can be grown in the future.

PL spectra of InGaN nanocolumns showed how growth temperature is a critical factor in achieving high PL intensity. High temperature growth improves PL emission but taken to excess leads to indium desorption, so compromise is needed. The core-shell structure of the nanocolumns, with an indium-rich core and a low indium shell was likely also a cause of poor PL efficiency. The role of surface effects was less clear but they may also have been a contributing factor.

Coalesced InGaN layers, consisting of an initial phase of nanocolumn growth followed by a continuous film were studied next. A very large increase in PL intensity was seen for high growth temperature samples compared to the nanocolumns. The observed surface structure of the coalesced layers, which featured homogenous grains, indicated that PL emission had been enabled by the overcoming of the core-shell structure.

We also considered a graded InGaN coalesced layer, where the indium alloy fraction varied vertically through the layer. The broad PL emission indicated that successful grading had likely taken place, but the low intensity indicated that improvements in growth were needed.

Lastly, coalesced films of pure InN were studied using a newly developed infrared PL set-up. The distinct PL spectra we obtained demonstrated the success of this set-up. The PL results were consistent with other studies and highlighted the importance of growth temperature and indium flux for obtaining high quality InN.

Chapter 7: Conclusions and Future Plans

The aim of this chapter is to summarise the results obtained from our studies of cubic III-nitride structures. With these results in mind, future work that could be carried out to build upon or clarify these results will be suggested.

7.1 Background research

Research of the literature has been highly informative for understanding the experimental results. Our interest in cubic nitrides has been explained in terms of the potential advantages they offer over the hexagonal structure, including the lack of internal polarization fields. Studies of cubic GaN growth have shown that MBE on GaAs (001) substrates allows high quality material with a very low hexagonal component to be grown. Less work has been conducted on the growth of cubic AlGaN alloys and doped GaN, but the difficulty of growing high AlN concentration AlGaN alloys has been demonstrated.

Numerous optical studies have been performed on cubic GaN and the PL spectrum features are well characterised. For cubic AlGaN, there is disagreement between theory and experiment regarding the band structure of the alloy across the AlN fraction range. A number of theoretical calculations indicate a transition from a direct bandgap to an indirect bandgap transition at higher AlN concentration, whilst some do not. Experimental results mostly do not give any indication of a transition occurring.

Cubic nitride QWs have been studied to a limited extent, showing the effect of well parameters on the emission characteristics. Optical and electrical studies of doped cubic GaN have shown that strong self-compensation occurs for high levels of Mg doping and that this is related to the onset of a blue emission band in the PL spectrum. In Si-doped cubic GaN, the broadening effect of the potential fluctuations due to Si incorporation was shown by several groups.

7.2 Research Outcomes

We have gathered a significant body of characterisation results for cubic and other III-nitride structures grown at Nottingham. The conclusions that we have been able to draw should prove highly useful for optimising and improving the growth of cubic nitrides in the future. These steps bring closer the achievement of high quality bulk substrates and device structures.

7.2.1 Cubic $Al_xGa_{1-x}N$ bulk films

Bulk cubic $Al_xGa_{1-x}N$ films covering the full range of AlN concentration up to pure AlN were extensively studied using PL and reflectivity measurements. The PL peaks increased in emission energy as the AlN fraction increased. In addition, the peaks broadened whilst their activation energy increased. The time-resolved PL showed that the PL decay lifetime reduced more slowly as the temperature was increased for the higher AlN fractions.

All of these results indicate an increasing degree of localisation for increased AlN fraction. Localisation in hexagonal AlGaN has been associated with nanoscale compositional inhomogeneities due to the random distribution of group III atoms, a phenomenon that leads to maximised localisation just above the middle of the alloy range. Our results for cubic material therefore suggest that there are other contributors to localisation coming into play at the higher AlN concentration, likely other defects and impurities.

The reflectivity measurements of the cubic AlGaN wafers have shown that the bandgap energy of the alloy increases continuously across the AlN fraction range but the positioning of a single data point suggested some kind of transition could take place. A model for the data, which assumed a direct bandgap absorption edge allowed good fits to be made for all alloy compositions up to 95% AlN concentration. However, without additional data in the region of $x = 0.66$, we are unable to state definitively whether there is a direct to indirect bandgap transition as predicted by theoretical sources.

7.2.2 Cubic AlGaN/GaN/AlGaN quantum wells

We have studied cubic AlGaN/GaN/AlGaN single quantum well structures with varying AlN concentration in the barrier. Despite a wide range of barrier AlN fractions being studied, only samples with 30% and 50% emitted PL spectra. Studies of the PL spectra at different excitation powers indicated a lack of quantum confined Stark Effect and hence the internal polarization fields that would be present in hexagonal material.

The PL emission was weaker than that recorded for the bulk AlGaN layers grown in the same system. In addition, time-resolved studies showed that the variation of PL decay time with temperature has a fall off that starts at a lower temperature in our samples compared to the literature. These results point to the interfaces as being a potential detriment to PL emission by introducing non-radiative centres such as defects due to interface strain.

The process of carrier escape from the QW and subsequent non-radiative recombination at higher temperatures was highlighted by the literature and consistent with our time-resolved studies. The lifetime for non-radiative recombination became shorter than the radiative lifetime at under T = 100K in both samples. The higher PL intensities from the 30% AlN structure as well as the more reliable time-resolved results suggest that the higher AlN concentration barriers are allowing carriers to escape from the well more easily.

7.2.3 Doped cubic GaN

Bulk layers of cubic GaN have been doped with varying amounts of magnesium and silicon. These samples were characterised using both optical and electrical methods. Optically, Si incorporation had little effect on the PL spectrum since the narrow range of Si doping levels prevented us from seeing the broadening effects observed in other studies. Localisation effects were observed in the temperature and time dependent PL, showing how dopant impurities contribute to localisation.

Hall measurements only worked on sub-micron thickness Si-doped layers which had smooth surfaces, compared to the rough surfaces on the thicker layers. This indicated that the thick growth was compromising the conductivity. The thin layer mobility values were lower than other sources, which may have been caused by carrier scattering off defects.

For Mg-doped cubic GaN, increasing the Mg concentration led to the emergence of a broad blue emission band in the PL spectrum. This band had similar properties to the one seen in hexagonal GaN:Mg, which has been attributed to compensating nitrogen vacancy-Mg acceptor complexes. Strong compensation was seen in the electrical measurements on Mg-doped GaN. Given the similarity between our results and the literature results for hexagonal GaN:Mg, the blue band in cubic GaN:Mg was also attributed to recombinations involving a deep donor compensating complex with a nitrogen vacancy and magnesium atom.

7.2.4 Nanocolumn growth of InGaN and InN

Various structures integrating indium and nanocolumn growth were studied. Although these structures did not consist of cubic material, many of them have not been widely studied elsewhere, so they are important for advancing nitride research. Firstly InGaN nanocolumns samples with a nominal indium fraction of 50% were characterised. Secondly we considered coalesced InGaN samples, which consisted of continuous layers grown on top of nanocolumns.

For all sample sets involving indium, we consistently observed that higher growth temperatures led to stronger PL emission intensity because of the improved crystal quality. The maximum growth temperature is however limited by the onset of indium desorption. The coalesced InGaN layer had vastly higher PL efficiency compared to the nanocolumn arrays. This was associated with the fact that the InGaN nanocolumns consisted of an indium-rich core surrounded by an indium-poor shell, as indicated by TEM. The coalesced film did not feature this phase separation, so strong InGaN luminescence was achieved.

The final extension of the InGaN nanocolumn growth process was a coalesced InGaN structure with a vertically graded indium composition, designed to have a broad absorption spectrum. The broad, low intensity PL spectrum suggested that the indium concentration had been graded, but that improved growth was needed.

The last set of samples that were discussed consisted of pure InN coalesced layers, whose PL spectra could only be measured using a dedicated infrared PL set-up. The PL spectra were

consistent with the literature and demonstrated the success of the new measurement apparatus.

7.3 Suggestions for Future Work

We have made considerable progress in the growth of cubic III-nitride structures, but many of the results we have obtained from the optical and electrical studies can be built upon, whilst some questions need further investigation. Beyond this, other materials and structures can be studied in order to bring us closer to device applications.

In the case of cubic AlGaN alloys, a greater number of AlN contents in the mid to upper range should be studied by PL and reflectivity in order to clarify whether any transition to indirect gap behaviour is taking place.

The cubic AlGaN/GaN/AlGaN QW structures were affected by a number of problems. Sample structures with different well widths could be grown in order to allow an optimum to be found. This optimum would then make investigation of the effect of AlN composition in the barriers on the interface quality easier. MQW structures could also be grown as a way of enhancing PL emission intensity. Improving the interfaces is an important step towards growing high quality heterostructures.

Regarding the doping of cubic GaN, considerable improvement is needed in the growth in order to obtain conductive layers with high mobility values. The use of post-growth annealing treatment to disassociate complexes in Mg-doped hexagonal GaN and thus reverse the effects of compensation has been demonstrated in the literature, and this is worth exploring for Mg-doped cubic GaN grown in the future.

For Si-doped GaN, a wide range of silicon doping levels need to be studied in order to determine how Si doping affects the optical properties in this growth system. Focusing on sub-micron thickness films is the most promising avenue for achieving high conductivity and mobility cubic GaN:Si.

For InGaN and GaN coalesced layers, the critical importance of growth temperature has been demonstrated. Improved quality InGaN and GaN coalesced and graded structures can thus be achieved by growing at an optimally high temperature. The optimisation of other parameters, such as indium/gallium flux can then also occur.

The improvements that can be made to the structures studied in this thesis have been summarised. The development of cubic nitrides can be furthered by considering other structures, particularly device structures. Simple devices such as Schottky diodes and resonant tunnelling diodes have already been grown and subject to preliminary tests that were not successful. Using the results of this thesis, particularly concerning doped material and layered structures, more of these devices should be grown and fabricated in order to identify optimal growth conditions. Once functional devices and high conductivity cubic nitride layers have been achieved, more complex devices, such as LEDs could be attempted.

References

1. Yoshizumi, Y., et al., Journal of Crystal Growth, 2007. **298**: p. 875.
2. Jeong, T., et al., Japanese Journal of Applied Physics, 2013. **52**: p. 10MA09.
3. Nakamura, S., et al., Japanese Journal of Applied Physics, 1995. **34**: p. L797.
4. Cao, X., et al., Applied Physics Letters, 2004. **84**: p. 4313.
5. Yoshida, H., et al., New Journal of Physics, 2009. **11**: p. 125013.
6. Omar, M., *Elementary Solid State Physics*. 1975: Addison-Wesley.
7. Ambacher, O., et al., Journal of Physics: Condensed Matter, 2002. **14**: p. 3399.
8. Li, Y., et al., Journal of Luminescence, 2007. **122-123**: p. 567.
9. Haskell, B.A., et al., Applied Physics Letters, 2003. **83**: p. 1554.
10. Waltereit, P., et al., Journal of Crystal Growth, 2000: p. 143.
11. Novikov, S.V., et al., Journal of Vacuum Science and Technology, 2010. **B28**: p. C3B1.
12. Jain, S.C., et al., Journal of Applied Physics, 1999. **87**: p. 965.
13. Suzuki, T., et al., Japanese Journal of Applied Physics, 2000. **39**: p. L497.
14. Silveira, E., et al., Journal of Crystal Growth, 2008. **310**: p. 4007.
15. Nanishi, Y., Y. Saito, and T. Yamaguchi, Japanese Journal of Applied Physics, 2003. **42**: p. 2549.
16. Schley, P., et al., Physica Status Solidi (c), 2007. **5**: p. 2342.
17. Moram, M.A. and M.E. Vickers, Reports on Progress in Physics, 2009. **72**: p. 036502.
18. Vurgaftman, I. and J.R. Meyer, Journal of Applied Physics, 2003. **94**: p. 3675.
19. Perlin, P., et al., Applied Physics Letters, 1995. **68**: p. 1114.
20. Fanciulli, M., T. Lei, and T.D. Moustakas, Physical Review B, 1993. **48**: p. 15144.
21. Kim, K., et al., Physical Review B, 1997. **56**: p. 7363.
22. Pugh, S.K., et al., Semiconductor Science and Technology, 1999. **14**: p. 23.
23. Korotkov, R.Y., J.M. Gregie, and B.W. Wessels, Applied Physics Letters, 2002. **80**: p. 1731.
24. Bermudez, V.M., C.I. Wu, and A. Kahn, Journal of Applied Physics, 2001. **89**: p. 1991.
25. Slepko, A., J. Ramdani, and A.A. Demkov, Journal of Applied Physics, 2013. **113**: p. 013707.
26. Ager, J.W. and N.R. Miller, Physica Status Solidi (a), 2012. **209**: p. 83.
27. Novikov, S.V., et al., Journal of Crystal Growth, 2008. **310**: p. 3964.

28. Novikov, S.V., et al., Semiconductor Science and Technology, 2008. **23**: p. 015018.
29. Kimura, R., et al., Journal of Crystal Growth, 2003. **251**: p. 455.
30. As, D.J., et al., Applied Physics Letters, 1997. **70**: p. 1311.
31. Qin, Z., M. Kobayashi, and A. Yoshikawa, Journal of Materials Science: Materials in Electronics, 1999. **10**: p. 199.
32. Daudin, B., et al., Journal of Applied Physics, 1998. **84**: p. 2295.
33. Wei, C.H., et al., Journal of Electronic Materials, 2000. **29**: p. 317.
34. Kemper, R.M., et al., Journal of Crystal Growth, 2013. **378**: p. 291.
35. Tsuchiya, T., et al., Journal of Crystal Growth, 1999. **198/199**: p. 1056.
36. Vilchis, H., V.M. Sanchez-R, and A. Escobosa, Thin Solid Films, 2012. **520**: p. 5191.
37. Yasui, K., K. Kanauchi, and T. Akahane, Thin Solid Films, 2003. **430**: p. 178.
38. Funato, M., et al., Physica Status Solidi (a), 1999. **176**: p. 509.
39. Wu, J., et al., Japanese Journal of Applied Physics, 1998. **37**: p. 1440.
40. Nakadaira, A. and H. Tanaka, Japanese Journal of Applied Physics, 1998. **37**: p. 1449.
41. Xu, D.P., et al., Journal of Crystal Growth, 1999. **203**: p. 40.
42. Martinez-Guerrero, E., et al., Physica Status Solidi (a), 2001. **188**: p. 695.
43. Okumura, H., et al., Journal of Crystal Growth, 1998. **189**: p. 390.
44. Koizumi, T., et al., Journal of Crystal Growth, 1999. **201**: p. 341.
45. Fox, M., *Optical Properties of Solids*. 2nd ed. 2010: Oxford University Press.
46. Novikov, S.V., et al., Journal of Vacuum Science and Technology B, 2005. **23**: p. 1294.
47. As, D.J., et al., Physica Status Solidi (c), 2003. **0**: p. 2537.
48. Pavesi, L. and M. Guzzi, Journal of Applied Physics, 1994. **75**(10): p. 4779.
49. Singh, J., *Electronic and Optoelectronic Properties of Semiconductor Structures*. 2003: Cambridge University Press.
50. Pankove, J.I., *Optical Processes in Semiconductors*. 1971, New York: Dover Publications.
51. McAleese, C., et al., Physica Status Solidi (b), 2006. **243**(7): p. 1551.
52. Reshchikov, M.A. and H. Morkoc, Journal of Applied Physics, 2005. **97**: p. 061301.
53. Feneberg, M., et al., Physical Review B, 2012. **85**: p. 155207.
54. Philippe, A., et al., Material Science and Engineering B, 1999. **59**: p. 168.
55. As, D.J. and K. Lischka, Physica Status Solidi (a), 1999. **176**: p. 475.
56. Xu, D., et al., Applied Physics Letters, 2000. **76**: p. 21.
57. Kanoun, M.B., et al., Journal of Applied Physics, 2005. **98**: p. 063710.

58. Röppischer, M., et al., Journal of Applied Physics, 2009. **106**: p. 976104.
59. Amin, B., et al., Journal of Applied Physics, 2011. **109**: p. 023109.
60. Landmann, M., et al., Physical Review B, 2013. **87**: p. 195210.
61. Okumura, H., et al., Physica Status Solidi (b), 1999. **216**: p. 211.
62. Badcock, T.J., et al., Applied Physics Letters, 2008. **93**: p. 101901.
63. Corfdir, P., et al., Journal of Applied Physics, 2012. **111**: p. 033517.
64. Köhler, U., et al., Physica Status Solidi (a), 2002. **192**: p. 129.
65. Schörmann, J., et al., Applied Physics Letters, 2006. **89**: p. 131910.
66. Martinez-Guerrero, E., et al., Material Science and Engineering B, 2001. **82**: p. 59.
67. Wang, D., S. Yoshida, and M. Ichikawa, Applied Physics Letters, 2002. **80**: p. 2472.
68. Li, Z.Q., et al., Applied Physics Letters, 2000. **76**: p. 3765.
69. Zhang, X., et al., Applied Physics Letters, 1998. **12**: p. 1890.
70. As, D.J., et al., Physical Review B, 1996. **54**: p. R11118.
71. Lin, M.E., et al., Applied Physics Letters, 1993. **63**: p. 932.
72. Kim, J.G., et al., Applied Physics Letters, 1994. **65**: p. 91.
73. Calleja, E., et al., Physica Status Solidi (b), 2007. **244**: p. 2816.
74. Murotani, H., et al., Journal of Applied Physics, 2013. **114**: p. 153506.
75. Tabata, T., et al., Japanese Journal of Applied Physics, 2013. **52**: p. 08LE06.
76. Wang, H.-C., et al., Thin Solid Films, 2010. **519**: p. 863.
77. Kusakabe, K., A. Kikuchi, and K. Kishino, Japanese Journal of Applied Physics, 2001. **40**: p. L192.
78. Grandal, J., et al., Physica Status Solidi (c), 2005. **2**: p. 2289.
79. Stoica, T., et al., Journal of Crystal Growth, 2006. **290**: p. 241.
80. Chang, Y.-L., M. Zetian, and L. Feng, Advanced Functional Materials, 2010. **20**: p. 4146.
81. King, P.D.C., T.D. Veal, and C.F. McConville, Physical Review B, 2008. **77**: p. 125305.
82. Cheng, T.S., et al., Applied Physics Letters, 1995. **66**(12): p. 1509.
83. Barnham, K. and D. Vredensky, *Low Dimensional Semiconductor Structures*. 2001: Cambridge University Press.
84. Franssila, S., *Introduction to Microfabrication*. 2nd ed. 2010: Wiley.
85. van der Pauw, L.J., Philips Technical Review, 1958. **26**: p. 220.
86. Knight, R.D., *Physics for Scientists and Engineers*. 2nd ed. 2008: Pearson Addison Wesley.

87. Young, H.D. and R.A. Freedman, *University Physics*. 13th ed. 2012: Addison-Wesley.

88. Lyman, C.E., et al., *Scanning Electron Microscopy, X-Ray Microanalysis and Analytical Electron Microscopy*. 1990: Plenum Press.

89. Li, J., et al., Applied Physics Letters, 2001. **79**: p. 3245.

90. Sampath, A.V., et al., Journal of Electronic Materials, 2006. **35**: p. 641.

91. Sampath, A.V., et al., Physica Status Solidi (c), 2011. **8**: p. 1534.

92. Murotani, H., et al., Physica Status Solidi (c), 2011. **8**: p. 2133.

93. Lee, K.B., et al., Journal of Applied Physics, 2007. **101**: p. 053513.

94. Bru-Chevallier, C., et al., Physica Status Solidi (a), 2001. **183**: p. 67.

95. Jiang, H.X., Optoelectronic Review, 2002. **10**: p. 272.

96. Cho, Y., et al., Physical Review B, 2000. **61**(11): p. 7203.

97. Kuokstis, E., et al., Applied Physics Letters, 2006. **88**: p. 261905.

98. Onuma, T., et al., Journal of Applied Physics, 2004. **95**: p. 2495.

99. Kim, H.S., et al., Applied Physics Letters, 2000. **76**(10): p. 1252.

100. Collins, C.J., et al., Applied Physics Letters, 2005. **86**: p. 031916.

101. Hecht, E., *Optics 4th Ed*. 2002: Addison Wesley.

102. *www.ioffre.rssi.ru/SVA*, in *Ioffre Physico Technical Institute*. 2001.

103. Li, D., et al., Solid State Sciences, 2011. **13**: p. 1731.

104. Liao, Y., et al., Applied Physics Letters, 2011. **98**: p. 081110.

105. Davies, J.H., *The Physics of Low Dimensional Semiconductors*. 1998: Cambridge University Press.

106. Teke, A., et al., Solid State Electronics, 2003. **47**: p. 1401.

107. Bacher, G., et al., Physical Review B, 1993. **47**(15): p. 9545.

108. Lefebvre, P., et al., Physica Status Solidi (b), 1999. **216**: p. 361.

109. Harris, J.C., et al., Applied Physics Letters, 2000. **77**(7): p. 1005.

110. Gurioli, M., et al., Physical Review B, 1991. **44**(7): p. 3115.

111. Takeuchi, T., et al., Japanese Journal of Applied Physics, 1997. **36**: p. L382.

112. Xu, S.J., et al., Physica Status Solidi (a), 2001. **188**: p. 681.

113. Kwon, Y.-H., et al., Applied Physics Letters, 2000. **76**: p. 840.

114. Morgan, T.N., Physical Review B, 1986. **34**: p. 2664.

115. Eckey, L., et al., Journal of Crystal Growth, 1998. **189/190**: p. 523.

116. Kaufmann, U., et al., Physical Review B, 1999. **59**: p. 5561.

117. Zolper, J.C., et al., Applied Physics Letters, 1996. **68**: p. 1945.
118. Nagamori, M., et al., Japanese Journal of Applied Physics, 2008. **47**: p. 2865.
119. Hautakangas, S., et al., Physical Review Letters, 2003. **90**: p. 137402.
120. Weimann, N.G., et al., Journal of Applied Physics, 1998. **83**: p. 3656.
121. Cherns, D., et al., Journal of Crystal Growth, 2013. **384**: p. 55.
122. Tourbot, G., et al., Nanotechnology, 2011. **22**: p. 075601.
123. Chang, Y.-L., F. Li, and Z. Mi, Journal of Vacuum Science and Technology, 2010. **B 28**: p. C3B7.
124. Kawakami, Y., et al., Applied Physics Letters, 2006. **89**: p. 163124.
125. Cai, X.M., et al., Nanotechnology, 2006. **17**: p. 2330.
126. Albert, S.B.-E., A, et al., Applied Physics Letters, 2011. **99**: p. 131108.